

Fabrication of electrically pumped vertical cavity surface emitters
employing GaN:Mg/GaN:Ge tunnel junction contacts

Thesis

for the degree of

doctor rerum naturalium (Dr. rer. nat.)

approved by the faculty of Natural Sciences of Otto von Guericke University Magdeburg

by M. Sc. Cleophace Seneza

born on 25.06.1974 in Nyaruguru

Examiners: Prof. Dr. André Strittmatter

Prof. Dr. Donat As

submitted on: 16.12.2021

defended on: 28.06.2022

Abstract

This thesis investigates novel concepts for the realization of vertical cavity surface emitting lasers (VCSEL) for the blue spectral range. Among them are the p-doping scheme at the p⁺⁺-contact layer for low contact resistance, different lithographic processing strategies for homogeneous current injection as well as GaN tunnel junctions. Further, conducting AlInN/GaN Bragg mirrors were developed for application in vertical cavity devices. Parameters were first optimized in conventional LED structures with and without additional GaN:Ge tunnel junction layers to be then applied in VCSEL structures. For p-type doping in MOVPE, improved conditions were determined for contact formation to p-GaN layers and for tunneling contacts. The best scheme as applied to LEDs had to be modified for VCSEL structures with GaN tunnel junctions in order to allow an efficient acceptor activation and to avoid surface roughening.

GaN tunnel junctions were also compared to an established ITO-layer as a current spreading layer on top of p-doped GaN:Mg. ITO layers absorb significantly more light than the GaN based tunnel junction. For p-side current injection, current confinement schemes based on a lateral injection, overgrown TJ structures and selectively deposited ITO layers were compared. In these approaches, the spontaneous light emission intensity increased up to 10 times for TJ-GaN VCSEL structures as compared to a reference ITO-VCSEL. Injection current densities of up to 30 kA/cm² were demonstrated even with tunnel junctions at moderate bias. Yet, lasing could not be achieved but the relevant issues are addressed in this work. Besides further improvements on current injection by better acceptor activation techniques, an improved interface quality of the dielectric DBR forming the upper mirror is required. Moreover, the reproducibility of the InGaN/GaN active region must be revised in order to maximize the internal quantum efficiency.

A concept of conducting Bragg mirrors was investigated in order to enable electron injection into the active region through the epitaxial mirror which is expected to homogenize current distribution across the active region. Highly conductive and reflective AlInN/GaN DBRs with ohmic current-voltage characteristic, a vertical specific resistance of $5 \times 10^{-4} \Omega \text{cm}^2$ and a maximum reflectivity of 99 % were demonstrated. While heavy Ge-doping within the GaN layers is helpful to reduce vertical resistance of the DBRs, structural degradation of the AlInN layers by such heavy doping leads to significantly reduced mirror quality.

Kurzfassung

Diese Arbeit untersucht neuartige Konzepte zur Realisierung von oberflächenemittierenden Laserdioden (VCSEL) für den blauen Spektralbereich. Dazu zählen die Dotierung der p⁺⁺-Kontaktschicht für die Realisierung eines geringen Kontaktwiderstands, verschiedene Ansätze zur lithographischen Prozessierung für eine homogene Strominjektion sowie die Implementierung von GaN-basierten Tunnelübergängen. Außerdem wurden elektrisch leitende AlInN/GaN-Bragg Spiegel entwickelt, die in vertikalen Resonatorbauelementen angewendet werden können. Zunächst wurden die Parameter in konventionellen LED-Strukturen mit und ohne zusätzliche GaN:Ge-Tunnelübergangsschichten optimiert, bevor diese dann bei der Herstellung von VCSEL-Strukturen verwendet wurden. Bei der p-Dotierung wurden verbesserte Bedingungen für die Erzeugung von niederohmigen Metallkontakten zur p-GaN-Schicht und für Tunnelkontakte ermittelt. Der beste Ansatz, der für LED angewendet werden konnte, musste für VCSEL-Strukturen mit GaN-Tunnelübergängen modifiziert werden, um eine effiziente Akzeptoraktivierung zu ermöglichen und eine Oberflächenaufrauung zu vermeiden.

GaN-Tunnelübergänge wurden auch mit einer etablierten ITO-Schicht als Stromverteilungsschicht auf p-dotiertem GaN:Mg verglichen. ITO-Schichten absorbieren dabei deutlich mehr Licht als der GaN-basierte Tunnelübergang. Auf der p-dotierten Seite wurde ein Ansatz zur Erzeugung einer Stromapertur basierend auf einer lateralen Strominjektion mit anderen Ansätzen wie überwachsenen Tunnelübergangs-Strukturen sowie selektiv abgeschiedenen ITO-Schichten verglichen. Bei diesen Ansätzen erhöhte sich die spontane Lichtemissionsintensität für GaN-VCSEL-Strukturen mit Tunnelübergang im Vergleich zu einer Referenz-ITO-VCSEL-Struktur um das 10-fache. Injektionsstromdichten von bis zu 30 kA/cm² wurden sogar mit Tunnelübergängen bei moderaten Betriebsspannungen erzielt. Lasertätigkeit konnte bisher nicht beobachtet werden, aber die relevanten Fragenstellungen und verbleibenden Probleme werden in dieser Arbeit diskutiert. Neben weiteren Verbesserungen der Strominjektion durch bessere Aktivierung der Akzeptoren, ist eine verbesserte Grenzflächenqualität des dielektrischen DBR erforderlich, welcher als oberer Spiegel fungiert. Darüber hinaus muss die Reproduzierbarkeit der aktiven InGaN/GaN-Region verbessert werden, um die interne Quanteneffizienz zu maximieren.

Es wurde ein Konzept zur Realisierung von elektrisch leitenden Bragg-Spiegeln untersucht, um eine Strominjektion in den aktiven Bereich durch den epitaktischen Spiegel zu ermöglichen.

Dies lässt eine homogenere Stromverteilung über den aktiven Bereich erwarten. Demonstriert wurden hochleitfähige und reflektierende AlInN/GaN-DBRs mit ohmscher Strom-Spannungs-Kennlinie, einem vertikalen spezifischen Widerstand von $5 \times 10^{-4} \Omega \text{cm}^2$ und einer maximalen Reflektivität von 99 %. Während eine hohe Ge-Dotierung innerhalb der GaN-Schichten hilfreich ist, um den vertikalen Widerstand der DBRs zu reduzieren, kann diese zur strukturellen Degradation der AlInN-Schichten und damit zu einer deutlich reduzierten Spiegelqualität führen.

Contents

Abstract.....	ii
Kurzfassung.....	iii
Contents	v
List of figures.....	vii
List of tables.....	xii
Chapter 1 Introduction.....	1
1.1 Overview of GaN-based VCSELs	1
1.2 Challenges of electrically pumped GaN-based VCSELs	1
1.3 Overview of thesis work.....	2
Chapter 2 Basic operation principles of GaN-based VCSELs	5
2.1 Emission characteristics in LEDs and VCSELs	5
2.2 Full cavity design for GaN based TJ-VCSEL.....	7
2.3 Doping issues.....	20
2.4 Tunnel junctions in GaN-based optoelectronic devices: Survey.....	21
Chapter 3 Experimental procedures and material	
characterization methods	23
3.1 Materials growth	23
3.2 Characterization methods.....	24
Chapter 4 Approaches for current injection	26
4.1 Current distribution: ITO vs. GaN:Ge	26
4.2 Current aperture design approaches.....	27
4.3 Summary	31
Chapter 5 Development of VCSEL structures.....	32
5.1 GaN:Mg/GaN:Ge tunnel junctions	32
5.2 Half-cavity VCSEL structures	44
5.3 Fabrication and characterization of full-cavity structures.....	57
5.4 Summary	64
Chapter 6 Highly reflective and conductive AlInN/GaN DBR.....	65
6.1 N-type doping of AlInN/GaN multilayer stacks	65
6.2 Structural properties of Ge-doped AlInN/GaN DBRs	71
6.3 Electrical and optical properties of Ge-doped AlInN/GaN DBRs	74

6.4 Analysis of conductance mechanisms	78
Chapter 7 Summary and outlook	81
References	83
Appendixes.....	88

List of figures

Fig. 2.1 A schematic comparison of conventional emission structures for VCSEL, LED and EEL (image adapted from [23]).....	5
Fig. 2.2 a) Schematic energy band diagram of a 3-fold $\text{In}_{0.18}\text{Ga}_{0.82}\text{N}/\text{GaN}$ MQW structure in [0001] growth direction without piezoelectric field b) Band diagram of a quantum well including the built-in piezoelectric field.	8
Fig. 2.3 Electromagnetic plane wave incident at the surface of a single electric layer with interfaces a, b to the surrounding media.	12
Fig. 2.4 Coherent electromagnetic wave falling onto a quarter wave Bragg reflector with a multi-layer stack with refractive indices n_1 and n_2 , from free space of index n_0 via the layer-stack to the substrate of refractive index n_s	13
Fig. 2.5 Simulated reflectivities at about 405 nm wavelength for a) AlInN/GaN DBRs and b) $\text{SiO}_2/\text{HfO}_2$ DBRs for increasing numbers of layer-pairs, c) Simulated reflectance spectra for oxide DBRs and AlInN/GaN bottom DBR.	16
Fig. 2.6 Simulation of the full 7-lambda cavity of 45x AlInN/GaN bottom DBR and 9x $\text{SiO}_2/\text{HfO}_2$ upper DBR with QWs inside.....	17
Fig. 2.7 The effect of absorptions and scattering losses in a) 45x AlInN/GaN DBR and b) 9x $\text{SiO}_2/\text{HfO}_2$ DBR.	18
Fig. 2.8 Lateral and vertical current transport in a TJ-GaN-based VCSEL using intra-cavity electrical contacts.....	19
Fig. 3.1 (a) A photography of an AIXTRON MOVPE reactor and b) a scheme of gas flow in the reactor [27]	23
Fig. 3.2 Epitaxial layer structure for typical a) GaN-based LEDs and b) GaN-based VCSELs.	24
Fig. 4.1 Photography to illustrate alignment procedure. a) Alignment marker structures on a quarter wafer (2-inch) with mesa etching and b) final structures realized after several consecutive alignment steps (e.g., alignments 1b, 2b, ...6b to the markers 1a, 2a, ...6a for formation of apertures (1), passivation (2), ... TJ-contact metals (6), respectively). Zoomed view of the first alignment to design apertures for lateral current injection (top image).	27

Fig. 4.2 Current injection schemes for GaN-based VCSEL and fabrication steps for a) ITO-VCSEL, b) SAG-approach and c) passivation approach for TJ- VCSELs.	29
Fig. 4.3 a) A side view SEM image of an etched aperture after TMAH treatment. b) SEM image showing size reduction of an original aperture due to the processing conditions and c) SEM image for optimized process parameters to fit an aperture opening with the original aperture by dry-etching for lateral current injection scheme.	30
Fig. 5.1 Hole concentration, mobility and resistivity of p-GaN versus CpMg-flow rate. The dashed line connecting data points are only guides to the eye. The optimum values for bulk GaN:Mg layers are found for an CpMg-flow of 1 sccm.....	33
Fig. 5.2 PL intensity of p-GaN doped with various Mg concentrations.	34
Fig. 5.3 Nomarski microscope image of the GaN:Mg surface for Mg-doping (at high CpMg-flow) of a bulk GaN layer as used for the contact region. Zoomed view of an inversion domain-related pyramidal defect.	34
Fig. 5.4 The L-I-V characteristic of 1 mm ² LEDs for an increased CpMg-flow either at the interface to the Ni/Au contact (std-LED) or at the TJ-interface to the GaN:Ge layer (left). Images of the LED emission at 450 nm wavelength at 40 mA current (right).	36
Fig. 5.5 I-V characteristics for 1 mm ² std- and TJ-LEDs exhibiting a reduced resistance at the tunnel junction contact using excessive CpMg-flow within a thin GaN:Mg region at the junction.	37
Fig. 5.6 a) EQE-L-J characteristics for std- and TJ-LEDs according to table 5.2 b) AFM image of these LEDs illustrating the size increase of V-pits upon GaN:Ge growth. The EQEs for std-LEDs are mainly lowered by the absorption of Ni/Au contacts.	38
Fig. 5.7 Typical I-V characteristics of 10 μm-LEDs (a) processed in 3 different current aperture methods (b). The inset is photograph image of the homogeneous emission of the 10 μm TJ-LED1.....	41
Fig. 5.8 A photograph image of an alphabetical display out of a 1 mm ² mesa for TJ- μLED1.....	42

Fig. 5.9 The I-V characteristics of 10 μm ITO- μLED devices and TJ- μLED devices with various Mg-doping schemes employing 3 different current aperture methods (a), AFM images ($3 \times 3 \mu\text{m}^2$ scans) of respective μLED surfaces (b), and comparison of I-V curves of the ITO- μLED 2 devices for apertures varying from 2 to 10 μm (c).....	43
Fig. 5.10 Properties of a 45xAlInN/GaN DBR. a) Measured and simulated reflectance b) AFM images c) SEM cross-section images d) HRXRD $\theta/2\theta$ -scans around GaN (0002) reflection and respective simulation.....	45
Fig. 5.11 I-V characteristics for standard LEDs and half-cavity VCSEL diodes with different CpMg-flow during growth of the p^{++} -region. LED1 and VCSEL1 had 4x increased flow, LED2 and VCSEL2 had a 40x increased flow as compared to the bulk GaN:Mg growth.	47
Fig. 5.12 A schematic layer structures for conventional VCSEL diodes 3 and 4.....	48
Fig. 5.13 Reflectivity and PL emission spectra for a) detuned and b) resonant VCSEL diode structures. Insets are Nomarski microscopy images of the wafer surface after growth revealing a large number of particles in b).	48
Fig. 5.14 a) I-V characteristics for half-cavity VCSEL diode 3 type with detuned cavity and for VCSEL diode 4 type with resonant cavity b) light output for VCSEL diode 3 type (solid lines) and for VCSEL diode 4 type (doted).....	49
Fig. 5.15 AFM images, $3 \times 3 \mu\text{m}^2$ scans, of ITO-VCSEL, TJ-LED1,2, and TJ-VCSEL1,2,3 with varied high p-doping concentration at the interface layer.....	51
Fig. 5.16 In-situ reflectivity data of two different CpMg-flows of 20 sccm (left) and 400 sccm (right) during growth of the p-GaN interface layer in TJ-VCSELs structures. A significant drop in reflected intensity was observed in the subsequently grown GaN:Ge layer when a high CpMg-flow was chosen, indicating surface roughening, as confirmed by AFM (bottom row).	52
Fig. 5.17 HRXRD (0002) $\theta/2\theta$ -scans for conventional half-cavity ITO-VCSEL structures compared to 45xAlInN/GaN DBR and 5xInGaN/GaN LED reference structures.	53
Fig. 5.18 a) PL and b) reflectivity mapping across a wafer of a conventional half-cavity ITO-VCSEL diode structure.	54

Fig. 5.19 a) Operating voltage and EL intensity as function of current-density for a 6 μm aperture device of half-cavity ITO-VCSEL. The inset shows spontaneous emission at a current density of 22.3 kAcm^{-2} . b) Typical EL emission spectra of a 6 μm device at various current densities from 10 Acm^{-2} to 3 kAcm^{-2}	55
Fig. 5.20 a) I-V characteristics of ITO-VCSEL and TJ-VCSEL diodes compared with reference LEDs. b) Schematic view of the current aperture approaches for b1) standard ITO-diodes processing and b2) TJ-diodes processing.....	56
Fig. 5.21 The I-V characteristic of the conventional ITO-VCSEL reference diode with (a) relative light output for apertures between 2 and 10 μm and (b) Normalized light output to the area of the aperture.	56
Fig. 5.22 a) Reflectivity (R_s) and b) transmission (T_s) of a 9-fold $\text{SiO}_2/\text{HfO}_2$ DBR test structure for a resonant wavelength of 415 nm.	57
Fig. 5.23 Cross sectional SEM image of the 9-fold $\text{SiO}_2/\text{HfO}_2$ DBR test structure.	58
Fig. 5.24 a) Schematic of the layout of the 7λ -cavity TJ-VCSEL1 structures including a device photograph. b) Large view of the cavity structure. c) Closer inspection of the transition region from the cavity area to the contact region showing the disruption of the ITO layer due to an elevation in the first SiN layer.	59
Fig. 5.25 Room temperature cw I-V characteristics and light output for a) 8 μm aperture and b) 6 μm aperture TJ- and ITO-VCSEL devices. Aperture diameter dependence of the light output of ITO-VCSEL (c) and TJ-VCSEL1 (d) devices.	60
Fig. 5.26 Pulsed I-V measurements, 1 % duty cycle, for ITO-VCSEL devices.	61
Fig. 5.27 L-I-V characteristics for a 6 μm diameter TJ-VCSEL1 showing an estimation for the threshold current densities for spontaneous (SE) and amplified spontaneous emission (ASE).	62
Fig. 5.28 Current injection dependent emission spectra of a) ITO-VCSEL device b) TJ-VCSEL1 device. In c) and d) individual spectra taken at 200 Acm^{-2} are compared.	63
Fig. 5.29 Superluminescence threshold current density for ITO- and TJ-VCSEL devices in dependance on the aperture size.....	64

Fig. 6.1 I-V characteristics for (a) Si-doped and (b) Ge-doped GaN/AlInN/GaN heterostructures. Insets show the sample layout for vertical electrical TLM measurements with a lateral spacing of 20 μm between terminals.....	67
Fig. 6.2 I-V-characteristics of Ge- or Si-doped 10-pair AlInN/GaN DBRs (s-DBRs) when current is injected vertically through the DBR. The samples description can be found in table 1. The inset shows corresponding photographs of quarter wafers. Note that particles induce an additional darkening of the sample.	70
Fig. 6.3 a) Photographs (wafer lying on quad paper with 5 mm line distance), b) AFM images (10x10 μm^2) and c) SEM cross-section images of AlInN/GaN DBRs A, B, C and D.	72
Fig. 6.4 a) In-situ reflectivity at 405 nm and b) in-situ curvature monitored during growth of 45-fold AlInN/GaN DBRs A, C, and D.	73
Fig. 6.5 High-resolution X-ray diffraction (0002) $\theta/2\theta$ -scans for DBRs A, B, C and D.....	74
Fig. 6.6 a) Illustration of the fabricated TLM structures for vertical current measurements b) J-V characteristics for DBRs A, B, C and D. c) Total resistance versus distance between adjacent TLM contacts for DBR C.....	76
Fig. 6.7 Reflectivity spectra of DBRs A, B, C, and D.	77
Fig. 6.8 Transfer matrix simulations of experimental reflectivity spectra for DBRs A, B, C and D.....	78
Fig. 6.9 Temperature-dependent I-V resistivity for DBRs A, B, C, and D.....	79
Fig. 6.10 Temperature dependence of the vertical I-V characteristics of low doped DBR C. The inset shows the sample scheme with a 1mm ² mesa of the DBR C in four-point-probe geometry.	80

List of tables

Table 5.1 Sample series to optimize Mg-doping in p-type GaN layer.....	33
Table 5.2 Sample structures to optimize Mg-doping in 1 mm ² std-LEDs and TJ- LEDs.	36
Table 5.3 Summary of growth parameters for GaN layers in the micro-LEDs for test of the various current aperture approaches as described in section 4.2.....	40
Table 5.4 Overview of half-cavity VCSEL structures with either ITO layers or TJ structures for current distribution.....	50
Table 6.1 Overview of nominal dopant species and GaN carrier concentration or molar flow rate for the AlN part in 10-fold DBRs (s-DBRs) and 45-fold DBRs.....	69

Chapter 1 Introduction

1.1 Overview of GaN-based VCSELs

Electrically pumped vertical cavity surface emitting lasers (VCSELs) are a class of semiconductor-based lasers that convert electrical energy into a light beam that is emitted vertically from the manufactured wafer surface. A VCSEL has a resonant cavity with its optical axis perpendicular to the wafer surface consisting of a bottom and an upper highly reflective distributed Bragg reflector (DBR). The prime features of GaN-based VCSELs include circular beam profile, small size, 2-D array scalability, low power consumption and low-price manufacturing [1, 2].

The direct bandgap energy of wurtzite GaN and its alloys (commonly InGaN, AlInN and AlGaIn) varies widely from 0.7 to 6.2 eV depending on the alloy composition, which allows emission covering wavelengths from UV to the near infrared region. Therefore, GaN-based VCSELs can pave the way to compact full color light sources and new technologies for optical storage, high resolution printing, bio-medical sensors, projection devices, and special applications in e.g. of headlights of vehicles [3-5]. Despite the unique applications of GaN-based VCSELs and the progress on device production, it is still very challenging for researchers and companies to fabricate devices with a process stable enough for mass production. One of many challenges of GaN-based VCSEL production is the realization of highly reflective DBR mirrors. Usually III-nitride DBRs suffer from intrinsic lattice-mismatch issues. Yet, lattice-matched (LM) AlInN has been proven a well-suited material to realize, for example, strain-free AlInN/GaN distributed Bragg reflectors (DBRs) [6-9]. Nevertheless, low efficiency light output of GaN VCSELs leads to low device performance and prevents some device applications [10, 11]. Therefore, researchers and companies are interested in the fabrication of GaN-based VCSELs using different approaches to increase the device performance.

1.2 Challenges of electrically pumped GaN-based VCSELs

The low performance and challenging fabrication of GaN-VCSELs are mainly caused by an inefficient current injection into the active region due to non-conducting nitride-based DBRs used and absorption loss issues [12]. By realization of conductive n-type AlInN/GaN DBRs, it would be possible to inject current through the DBR for VCSEL operation [13]. However, the

conductivity of n-type nitride-based DBRs requires a complex growth process and the achievable conductivity is still too low. Therefore, in most cases, researchers used intra-cavity contacts for current injection [13, 14]. Si has been recently applied to n-type doping of Al(In, Ga)N/GaN DBRs. But both Si-doped graded DBRs [12, 15] as well as Si-doping modulation at the interface of AlInN/GaN layers [13] require a complex growth process and the reported achieved resistances are still relatively high. Higher Si-doping concentrations could be necessary for sufficient cancellation of polarization effect between DBR layers, but such high Si-doping can lead to severe optical and structural degradation of DBR layers [16]. Recently, excellent conductivity of AlInN:Ge/GaN:Ge heterostructures better than for AlInN:Si/AlInN:Si structures has been reported [17]. Despite the Ge memory effect and the challenges of LM AlInN growth that put limits on the MOVPE growth of highly reflective Ge-doped DBR structures, this thesis demonstrates that Ge-doped AlInN/GaN DBRs with high conductivity and high reflectivity can be achieved by adjusting Ge-doping in AlInN layers [18].

The other problem that lowers the efficiency of current injection of GaN-based VCSELs grown by metalorganic vapor phase epitaxy (MOVPE) is the low lateral hole mobility in p-GaN layers. It is known that high p-doping GaN levels, [Mg] well above $3 \times 10^{20} \text{cm}^{-3}$ corresponding to carrier concentration around $1 \times 10^{18} \text{cm}^{-3}$, may cause the formation of inversion domains, pyramidal defects, and nitrogen vacancies leading to self-compensation effects and reduce the free hole concentrations [19, 20]. In addition, the low hole mobility in p-GaN materials hinders current spreading as necessary for lateral current distribution. Indium-tin-oxide (ITO) transparent conducting contact layers or semi-transparent metal contact layers, for example oxidized Ni/Au layers, are usually employed on top of the GaN:Mg layer to enable current distribution across the intended junction area of LEDs and VCSELs. But additional ITO layers or thin film oxidized Ni/Au layers limit the performance of blue VCSELs since an embedded optical absorbing layer inside of the cavity dramatically increases the threshold current, possibly inhibiting lasing action [4, 21]. To alleviate these absorption loss issues, an employment of tunnel junction layers on top of GaN:Mg layers that replaces the oxidized Ni/Au layers, has revealed a better lateral current spreading and an improved emission intensity [1, 4].

1.3 Overview of thesis work

The GaN-based VCSEL structures were grown by MOVPE. A hybrid VCSEL on sapphire substrates design was chosen, which is characterized by a single growth process of an epitaxial bottom DBR and a cavity region that contains the optically active layers. By optical lithography

small-sized diodes with diameters below 10 μm were processed. A dielectric upper DBR mirror was deposited in the final processing step. Each component of the VCSEL structure was studied and optimized to enable a sufficiently high gain and to observe eventually stimulated emission in the final device.

This PhD work aimed at developing an electrically pumped GaN-based VCSEL in the near UV-blue spectral range with improved operation characteristics by employing a GaN:Mg/GaN:Ge tunnel junction on top of the p-doped region. In contrast to conventionally used oxidized Ni/Au and ITO tunnel junction on top of p-GaN as current spreading layers [4, 21], the GaN:Mg/GaN:Ge tunnel-junction characteristics allow a superior current spreading, lower laser threshold due to lower light absorption and therefore higher optical output power. In this study, also the Mg-doping in tunnel junctions and for contact formation was studied to improve current injection. To achieve an efficient forward current transport across tunnel junctions, heavily Mg doped p-type GaN (p^{++}) and heavily Ge-doped n-type GaN (n^{++}) layers were studied using various doping levels and film thicknesses. The p-type GaN activation and surface pretreatments prior to metal contact deposition were optimized using simple structures of conventional LEDs and tunnel junction LEDs (TJ-LEDs) for later deployment in TJ-VCSELs. Different current aperture designs were investigated to enhance the carrier injection efficiency. The upper dielectric DBR mirrors were analyzed for their spectral characteristic and interface quality. In addition, the n-type doping AlInN/GaN DBRs was studied to enable extra-cavity contacts, which would allow for a shorter cavity length and should reduce threshold current.

The thesis work is organized in 7 chapters as follows.

After this introduction, chapter 2 reviews the principles for light emission of LEDs and VCSELs in the near UV and blue spectral region using group III-nitrides and their alloys. The stimulated emission process in the VCSEL, the full design of GaN-based VCSEL with quantum confined structures, the basics of Bragg reflectors as well as electrical injection issues connect with p- and n-type doping of GaN, and with GaN:Mg/GaN:Ge tunnel junction structures are discussed.

The employed experimental procedures and material characterization methods are presented in chapter 3.

Chapter 4 describes the processing steps using standard optical lithography and the investigated current confinement approaches for intra-cavity contacts in GaN VCSEL structures.

In chapter 5, optical and electrical results are compared for conventional and tunnel junction LEDs and half-cavity VCSEL structures. Results on full VCSEL structures including a dielectric top DBR are also presented in this chapter.

The results of n-type doping of AlInN/GaN DBRs to achieve both high reflectivity and low resistivity are given in chapter 6.

The last chapter contains a summary and suggestions for future work.

Chapter 2 Basic operation principles of GaN-based VCSELs

2.1 Emission characteristics in LEDs and VCSELs

There is a variety of optoelectronic semiconductor devices that convert electrical energy into optical radiation, namely, light emitting diodes (LEDs) and several types of semiconductor lasers including edge emitting lasers (EELs) and vertical cavity surface emitting lasers (VCSELs). A schematic comparison of the emission characteristics of LEDs, EELs and VCSELs is shown in Fig. 2.1. An LED consists of a semiconductor p-n junction that under proper forward-biased conditions can emit spontaneous radiation with large divergence angles as indicated by the large spherical spot. LEDs have a large field of applications such as general lighting, displays, visible light communication or as light source for optical-fiber communication systems [22].

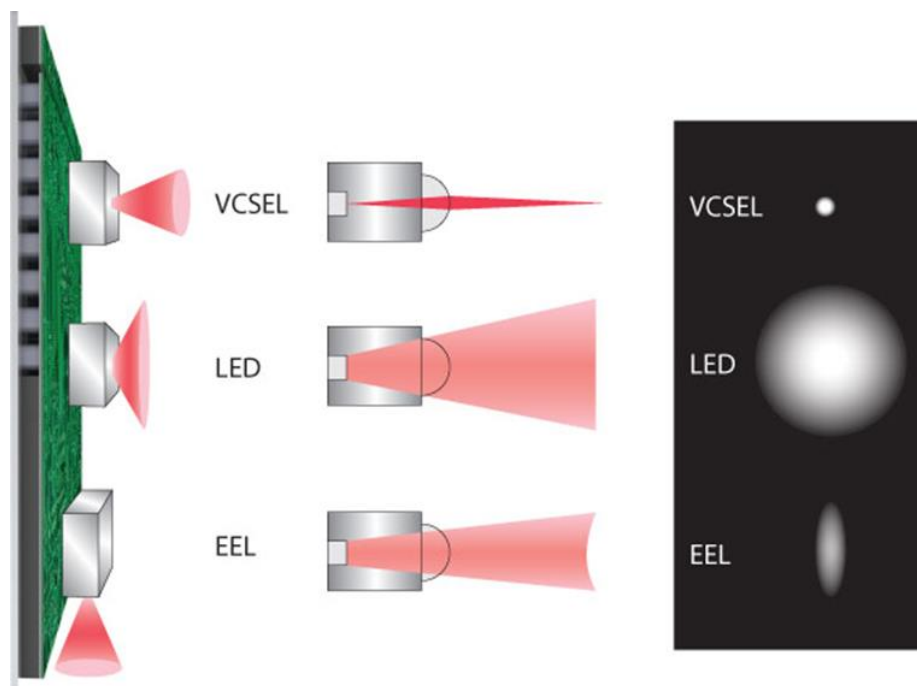


Fig. 2.1 A schematic comparison of conventional emission structures for VCSEL, LED and EEL (image adapted from [23]).

In contrast to LED, EEL and VCSEL operate by stimulated emission of light. The conventional EELs (bottom image) are different to VCSELs (top image) by emitting via the end-facets of planar waveguide guiding light parallel to the active layer while VCSELs are emitting perpendicularly to the plane of the active region which is enclosed in a cavity delimited by

mirrors. Consequently, other parameters like effective length of the gain medium, threshold current, and optical losses are different for VCSELs as compared to EELs. While the two facets of an EEL are broadband reflecting mirrors, the mirrors of a VCSEL usually formed by distributed Bragg reflectors (DBRs) provide high-reflectivity feedback within a narrow spectral region only. Laser is the acronym for “light amplification by stimulated emission of radiation”. A basic condition for laser amplification is “population inversion” between two energy states and stimulated transitions between the states yielding optical gain. An optical gain material of a laser diode is typically a multilayer heterostructure embedded in a p-n junction diode. Light produced by a spontaneous emission process is incoherent (random in space and time), which is the dominant mechanism in LEDs. Contrarily, stimulated emission by light amplification is coherent and is the main condition for lasing of VCSELs. If a free electron occupies a lower energy level within the conduction band and a hole state (or empty state) is available in the valence band, their recombination can be stimulated by an incident photon with a wavelength λ matching the electron-hole energy difference, yielding a second photon through electron-hole recombination. The two photons have the same wavelength and phase, resulting in a coherent laser output, which is the concept of “stimulated emission by light amplification”.

The wavelength λ of the stimulated emission is determined by the bandgap energy of the active material (eq. 2.1), i.e., the energy-difference of the lowest conduction band state and the highest valence band state [22].

$$\frac{hc}{\lambda} = E_{CB} - E_{VB} = E_g \quad (2.1)$$

where c is the speed of light in vacuum, h is Planck’s constant, E_{CB} and E_{VB} are conduction band energy and valence band energy respectively.

The condition for population inversion in a semiconductor laser is derived from the assumption of thermal equilibrium conditions and three optical transition processes (absorption, spontaneous emission, and stimulated emission) [22, 24]. Thus, the condition for inversion population (eq. 2.2) is that the ratio of stimulated emission rate (R_{st}) and absorption (R_{abs}) must be larger than unity.

$$\frac{R_{st}}{R_{abs}} = \exp\left[\frac{(\Delta E_f - E_g)}{k_B T}\right] > 1 \quad (2.2)$$

where $\Delta E_f = E_{fe} - E_{fh}$ is the difference of quasi-Fermi levels for electrons in the conduction band (E_{fe}) and for holes in the valence band (E_{fh}). Hereby, k_B denotes the Boltzmann constant and T represents the absolute temperature. Equation 2.2 establishes the necessary condition for lasing, with a quasi-Fermi level separation larger than the bandgap energy (E_g):

$$E_{fe} - E_{fh} > \frac{hc}{\lambda} > E_g \quad (2.3)$$

Since the quasi-Fermi levels are depending on carrier density and temperature which are controlled by carrier injection, the relation in equation 2.3 is much depending on the gain material properties and the junction media (layer structure, doping concentrations of the p-n junction, bandgap, refractive index variations, etc.). Therefore, the condition for population inversion is necessary but it does not equal the condition of lasing which is only possible when the net gain exceeds losses. For an electrically pumped GaN-VCSEL, a bias voltage that is large enough to inject enough electrons and holes into the respective bands is required in order to satisfy the condition for population inversion while highly reflective and absorption-less Bragg mirrors are required to provide the necessary optical feedback for stimulated emission.

2.2 Full cavity design for GaN based TJ-VCSEL

2.2.1 Multi-quantum-well design and quantum-confined structures

Multiple InGaN/GaN quantum wells are usually employed as active region for GaN-based lasers to allow for fine-tuning of the emission wavelength across the visible spectral range. The intensity of the luminescence peak in quantum wells (QWs) is defined as a product of radiative lifetime and the number of emitters. While the radiative lifetime is related to electron-hole overlap, the number of emitters is proportional to the thickness but may be influenced by carrier diffusion across the pn-junction as well.

For the design of GaN-based LEDs or VCSELs working in the near UV and blue spectral region, the indium content and thickness of the InGaN quantum wells have to be adjusted. In this work, the indium content in the InGaN optical gain material, except otherwise noted, is tuned to about 18 % for light emission in the blue spectral region. This indium concentration ensures carrier confinement between InGaN/GaN with an energy bandgap offset between these layers of about 0.6-0.7 eV. The strain-free $\text{In}_{0.18}\text{Ga}_{0.82}\text{N}$ bandgap energy calculated by Pereira et al. [25] is around 2.75 eV corresponding to the minimum turn-on voltage for forward current

within an ideal InGaN-based LED or VCSEL. Detailed properties of InGaN/GaN multiple quantum well (MQW) structures can be found for example in [26, 27]. Fig. 2.2a shows a schematic energy band diagram of a 3-fold $\text{In}_{0.18}\text{Ga}_{0.82}\text{N}/\text{GaN}$ MQW structure on c-sapphire without and with piezoelectric field. The InGaN layer, with relatively high indium concentration, on top of GaN experiences a compressive strain resulting in a strong piezoelectric field from $[000\bar{1}]$ to $[0001]$ crystal growth direction, which results in a band bending of both conduction and valence bands and a reduction of the electron and hole wave function (Ψ) overlap (Fig. 2.2b). This band bending effect is known as quantum confined stark effect (QCSE) as response of the confined electron and hole states in the QWs to a built-in piezoelectric field (P_z) and leads to a red-shift of the emission. Furthermore, due to the indium compositional fluctuations in InGaN/GaN quantum wells, substantial inhomogeneous broadening occurs [28]. QCSE, slow heat dissipation, defects, and electron leakage from the MQW contribute to non-radiative recombination [26]. Besides these issues which maybe partly addressed by material improvement during growth, a well-designed cavity is very important to achieve lasing operation of VCSEL structure. However, the quality of VCSEL processing, i.e., surface damage, can also have an impact on non-radiative recombination and electron leakage, consequently reducing the net VCSEL performance.

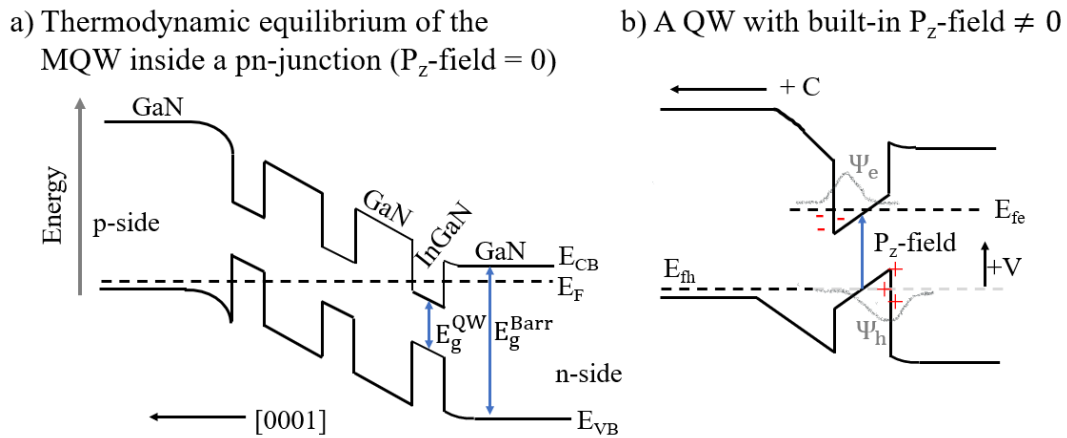


Fig. 2.2 a) Schematic energy band diagram of a 3-fold $\text{In}_{0.18}\text{Ga}_{0.82}\text{N}/\text{GaN}$ MQW structure in $[0001]$ growth direction without piezoelectric field b) Band diagram of a quantum well including the built-in piezoelectric field.

Generated photons have to be confined inside the optical cavity of a VCSEL to provide the necessary optical feedback for stimulated emission radiation. That way photons pass several times through the active region stimulating secondary photons before leaving the laser cavity. Constructively added amplitudes of all photons inside the cavity built up the total light intensity

propagating out of the laser cavity. Mirror defining the cavity ends lead to resonant cavity modes permitting only standing waves. Optical cavities are described by a Fabry-Perot resonator satisfying the condition for constructive interference through [22, 24]:

$$L = \left(\frac{\lambda_0}{2n}\right) m \quad (2.4)$$

where L is the geometrical cavity length (effective distance between two mirrors), λ_0 is the resonant wavelength, n represents the reflective index of the cavity material, and m is an integer number. The shortest cavity length allows for fundamental longitudinal mode ($m=1$) operation only. As L increases more modes become possible for a given laser. The realization of electrically pumped short cavity GaN-based VCSELs is still difficult because of the requirement for intra-cavity electrical contacts and current spreading which results in a cavity length of multiples of λ_0 . In addition, due to the finite penetration depth of the optical mode into the epitaxial DBR it is also difficult to achieve single mode lasing with extra-cavity contacts. The free spectral range or optical mode spacing $\delta\lambda$ is defined as

$$\delta\lambda = \frac{\lambda_0^2}{2n_c L_c} \quad (2.5)$$

where λ_0 is the wavelength, n_c and L_c are the effective refractive index and length for the given mode, respectively. In a semiconductor laser, the optical gain per unit length is a material parameter describing stimulated emission [24, 29]. The optical gain (g) due to stimulated emission is offset by the optical losses (α_{int}) due to internal absorption and scattering process. Lasing can be achieved only when the gain inside the cavity is greater than a threshold gain g_{th} compensating all optical losses. Therefore, a minimum pump energy into the gain region is required to saturate the optical losses and to enable amplification along the beam direction (z -direction) as:

$$E(z) \propto \exp[(g - \alpha_{\text{int}})z]. \quad (2.6)$$

Considering a complete round trip and no other optical losses other than internal cavity and mirror losses, with power reflectances R_1 and R_2 of the mirrors, the threshold gain (g_{th}) is given by

$$\Gamma g_{\text{th}} = \alpha_{\text{int}} + \frac{1}{2L} \ln\left(\frac{1}{R_1 R_2}\right) \quad (2.7)$$

The term $\frac{1}{2L} \ln\left(\frac{1}{R_1 R_2}\right) = \alpha_m$ represents the optical mirror loss, while Γ is the confinement factor of the optical field in the active layer. Maximum Γ is achieved when the quantum well region overlaps with the antinode of the optical field. To reach lasing in VCSELs, the optical field must experience gain through many roundtrips and minimum outcoupling loss. For this to happen, the mirrors must exhibit very high reflectivities (>99%) [30], which are usually realized with distributed Bragg reflectors (DBRs). The optical gain of a laser has a linear dependence on injected current. At low current there is only spontaneous emission until population inversion is reached. By further increasing the current, optical gain is generated which increases until the threshold for lasing is reached. The lasing begins when the injected current is greater than the threshold current, J_{th} , defined as:

$$\begin{aligned} J_{th} &= \frac{J_0 d}{\eta_{in}} \left(1 + \frac{g_{th}}{g_0}\right) \\ &= \frac{J_0 d}{\eta_{in}} \left\{1 + \frac{1}{g_0 \Gamma} \left[\alpha_{int} + \frac{1}{2L} \ln\left(\frac{1}{R_1 R_2}\right)\right]\right\} \end{aligned} \quad (2.8)$$

where g_0 is the optical gain of material at injected current density J_0 , d denotes the active layer thickness, and η_{in} is the internal quantum efficient. Other parameters have their usual meaning. Therefore, any lasing device is fundamentally characterized by the threshold current density. Low J_{th} values require an optimization of parameters such as η_{in} , L , Γ , R_1 , R_2 , and α_{int} .

2.2.2 Distributed Bragg reflectors

A distributed Bragg reflector (DBR) consists of a periodic modulation of the index of refraction usually formed by two different materials with layer thicknesses equal to a quarter of the wavelength in the material. At each interface of a DBR, incident light from the first index material is partially reflected and the other part of light is transmitted in the second material. The resulting phase-change $\Delta\phi$ due to light propagation along geometric distance d of light with wavelength λ through a non-absorbing layer with refractive index n is given by:

$$\Delta\phi = \frac{2\pi}{\lambda} nd \quad (2.9)$$

where the product (nd) is called the optical thickness of the layer. For $d = \frac{\lambda}{4}$, the resulting phase difference $\Delta\phi$ is 2π , thus the light experiences constructive interference [24]. Each layer fulfils Bragg's condition when their respective layer thicknesses are:

$$d_L = \frac{\lambda_0}{4n_L} \text{ and } d_H = \frac{\lambda_0}{4n_H} \quad (2.10)$$

d_L and d_H are layer thicknesses of the DBR layers with low reflective index n_L and high refractive index n_H , respectively. Under such condition (eq. 2.10), all reflected waves from the interfaces of the DBR add up in phase, allowing reflectivities above 99% with a minimum number of layer pairs. The peak reflectivity always depends on the number of layer pairs and the refractive index contrast ratio $\frac{\Delta n}{n}$ between high and low index material given by:

$$\frac{\Delta n}{n} = \frac{(n_L - n_H)}{n_H} \quad (2.11)$$

The larger $\frac{\Delta n}{n}$ is, the fewer Bragg-pairs are required for maximum reflectivity. The stopband width $\Delta\lambda_{\text{stop}}$ depends on the refractive index contrast Δn between layers of a DBR and is calculated by [5]:

$$\Delta\lambda_{\text{stop}} = \frac{2\lambda_0\Delta n}{\pi n_{\text{eff}}} \quad (2.12)$$

where n_{eff} is the refractive index given by

$$n_{\text{eff}} = 2 \left(\frac{1}{n_H} + \frac{1}{n_L} \right). \quad (2.13)$$

The effective penetration L_{eff} of the electric field in a DBR cavity can also be approximated as

$$L_{\text{eff}} = \frac{d_H + d_L}{4} \times \frac{n_H + n_L}{n_H - n_L} \approx \frac{\lambda_0}{4\Delta n}. \quad (2.14)$$

2.2.3 Transfer matrix method

The transfer matrix method for dielectric layer stacks is used to simulate the optical properties, including reflectance and transmittance of a DBR [5, 30-35]. In this method, the expression for calculating reflectance and transmittance of a dielectric or semiconductor layer stack is derived from the solutions of the optical wave equation allowing also to account for possible optical absorption or gain and scattering losses through the imaginary part of the complex index of refraction. The formula used for computing the maximum reflectivity and transmittance at a given resonance wavelength of a quarter-wavelength layer stack with multi-layer pairs can be obtained by the transfer matrix model below as described by MckLeod [34].

Fig. 2.3 shows a single thin film of thickness d and refractive index n coated on an infinitely thick substrate with refractive index n_s . While ‘a’ represents the interface between the film and the incident medium (for example, air with refractive index n_0), the interface between the film and substrate is denoted by ‘b’. An incident electromagnetic plane wave with an electric field amplitude E_0 perpendicular to the plane of incidence experiences multiple reflections and transmissions at each interface along the propagation direction (z -direction). Reflected and transmitted waves at each interface can be summed up yielding one forward-going wave and one backward-going wave, respectively.

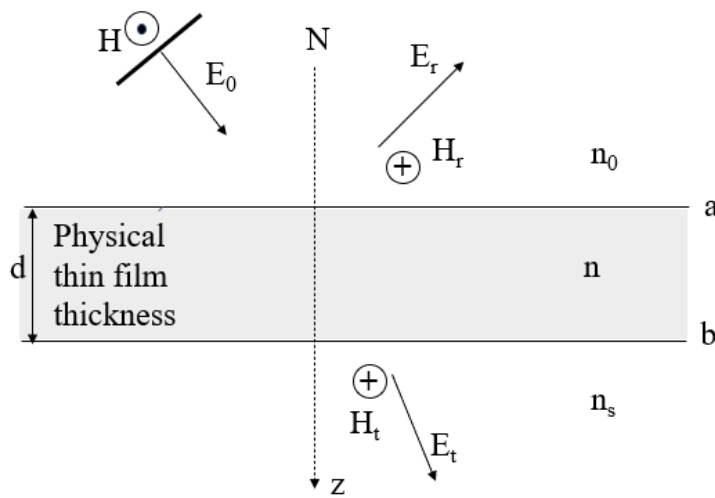


Fig. 2.3 Electromagnetic plane wave incident at the surface of a single electric layer with interfaces a, b to the surrounding media.

For each layer, a characteristic matrix describing the forward-and backward-going parts can be written as

$$\begin{bmatrix} E_a \\ H_a \end{bmatrix} = \begin{bmatrix} \cos\left(\frac{2\pi}{\lambda} nd\cos\theta\right) & j\frac{1}{\eta}\sin\left(\frac{2\pi}{\lambda} nd\cos\theta\right) \\ j\eta\sin\left(\frac{2\pi}{\lambda} nd\cos\theta\right) & \cos\left(\frac{2\pi}{\lambda} nd\cos\theta\right) \end{bmatrix} \quad (2.15)$$

where $j = \sqrt{-1}$ represents the imaginary number. The phase shift experienced by the wave as it traverses a distance d normal to the interface is given by $\delta = -\frac{2\pi}{\lambda} nd\cos\theta$. The phase factor $\cos\theta$ is unity for normal incidence waves, θ is the angle of incidence at the boundary and $\eta = n\cos\theta$. The refractive index n is a real number only for a non-absorbing (dielectric) material, otherwise it is complex and can be expressed in terms of the coefficient of extinction (k) by

$$n = \text{Re}(n) - jk, \quad (2.16)$$

where $\text{Re}(n)$ is the real part of the complex index n . From eq. 2.16, reflectance (R), transmittance (T) and optical losses can be evaluated. For DBR layer-stacks of periodic q layers with thicknesses d_i , in Fig. 2.4 the characteristic transfer matrix becomes a matrix product as follows:

$$\begin{aligned} \begin{bmatrix} E_0 \\ H_0 \end{bmatrix} &= \prod_{i=1}^m \begin{bmatrix} \cos\delta_i & j\frac{1}{\eta_i} \sin\delta_i \\ j\eta_i \sin\delta_i & \cos\delta_i \end{bmatrix} \begin{bmatrix} E_m \\ H_m \end{bmatrix} \\ &= [M_1][M_2] \dots [M_q] \begin{bmatrix} E_m \\ H_m \end{bmatrix} \end{aligned} \quad (2.17)$$

M_i is the matrix associated with layer $i = 1, 2, 3, \dots, q$. The phase change when the normal wave traverses the optical absorbing films is given by,

$$\delta_i = -\left(\frac{2\pi \text{Re}(n_i)d_i}{\lambda} - \frac{j2\pi k d_i}{\lambda}\right) \quad (2.18)$$

The negative sign indicates a phase change. The product of M_1 to M_q is called the characteristic matrix of the stack.

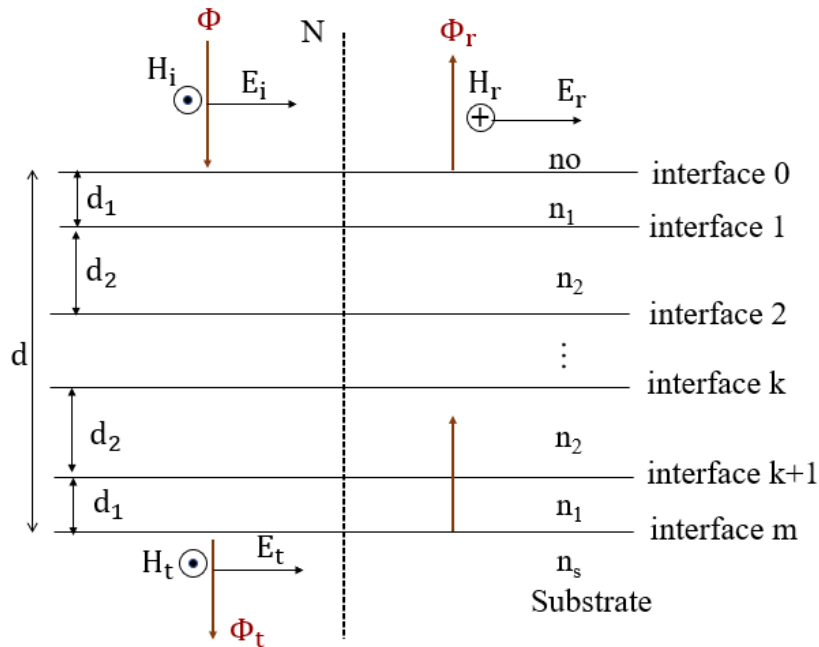


Fig. 2.4 Coherent electromagnetic wave falling onto a quarter wave Bragg reflector with a multi-layer stack with refractive indices n_1 and n_2 , from free space of index n_0 via the layer-stack to the substrate of refractive index n_s .

By normalization of the characteristic matrix to the last matrix at the interface of the film with the substrate the eq. 2.17 is written as:

$$\begin{bmatrix} B \\ C \end{bmatrix} = [M_1][M_2][M_3] \dots [M_q] \begin{bmatrix} 1 \\ \eta_m \end{bmatrix} \quad (2.19)$$

where the suffixes 1, 2, ..., m equal the number of interfaces, $B = \frac{E_0}{E_m}$, $C = \frac{H_0}{E_m}$. Hereby, $\eta_m = \frac{H_m}{E_m}$ is called the optical admittance to the substrate interface. A simple form of characteristic transfer matrix is given by the product of the optical matrix M_i for each single interface of one layer i and thickness d_i to the whole length d in the DBR stack.

$$M = \begin{bmatrix} E_0 \\ H_0 \end{bmatrix} = \prod_{i=0}^{q-1} M_i \begin{bmatrix} E_m \\ H_m \end{bmatrix} \quad (2.20)$$

$$M_i = \begin{bmatrix} M_{11} & M_{12} \\ M_{21} & M_{22} \end{bmatrix} \quad (2.21)$$

The subscripts 0 and m denotes first layer interface with free air and last layer interface to the substrate, respectively. M_{ij} , ($i \neq j$), are elements of the matrix M . The maximum reflectivity is obtained at the resonance wavelength of a quarter-wavelength layer stack with q layer pairs as:

$$R = \left(\frac{1 - \frac{n_1^2}{n_0 n_s} \left(\frac{n_1}{n_2} \right)^{2q}}{1 + \frac{n_1^2}{n_0 n_s} \left(\frac{n_1}{n_2} \right)^{2q}} \right)^2 \quad (2.22)$$

where n_0, n_s, n_1 and n_2 are the indices of the free-space, substrate, high and low index materials, respectively. The most important in the eq. 2.22, is how to choose the number of layer-pairs in dependance of n_1/n_2 to reach a reflectivity above 99 %. For negligible absorption, the transmission in the whole layer-stack can be calculated using the following expression

$$T = \frac{4\eta_0 \text{Re}(\eta_m)}{|\eta_0 B + C|^2} = 1 - R \quad (2.23)$$

where η_0 is the optical admittance of the incidence at the boundary defined by $\eta_0 = n_0 \cos\theta$. $\eta_m = \frac{H_m}{E_m} \approx n_m \cos\theta$, is the substrate optical admittance.

Reflectivity simulations of quarter-wave stacks for GaN-based and dielectric DBRs for visible spectral range are discussed in the next subsection 2.2.4. Several ways to design Bragg reflectors are discussed in different publications and books [6, 24, 36-38]. This thesis work discusses a hybrid GaN-based VCSEL cavity, which is formed by an epitaxially grown

AlInN/GaN DBR followed by the cavity region and the upper dielectric mirror consisting of an oxide based DBR, such as SiO₂/HfO₂ DBR, deposited in the final processing step.

2.2.4 AlInN/GaN DBRs and Oxide DBRs

Using a lattice matched AlInN layer one can achieve strain-free growth and reflectivities higher than 99 % for DBRs but more than 40 layer pairs are required [6-9]. The relatively large number of DBR pairs is due to the low index contrast of around 7 % for lattice matched AlInN (~18 % indium composition) relative to GaN, resulting in significant penetration of the optical wave into the DBR layers and a stopband width with a FWHM of about 30 nm wavelength [27].

The upper dielectric DBRs, usually oxide based DBRs, such as SiO₂/Ta₂O₅ and SiO₂/HfO₂ layer-stacks, have been successfully proven for the realization of crack-free highly reflective DBRs (~99.99%) and employed in high quality microcavities. Due to their higher index contrast they offer a shorter penetration depth and larger stopband width [3, 4, 39, 40]. In contrast to AlInN/GaN DBRs, SiO₂/HfO₂ DBRs have high index contrast of about 26% resulting in a relatively wide stopband width of ~100 nm and leading to high reflectance even for less than 10 Bragg pairs. Therefore, a SiO₂/HfO₂ multi-layer stack is suitable for the fabrication of GaN-based hybrid cavities for blue vertical emitters. However, both epitaxial growth of the lattice matched AlInN in group III-nitrides based DBRs as well as sputtering of HfO₂ in dielectric DBRs proceed at very small rate requiring long process times of at least 24 hours. In case of AlInN/GaN DBRs, the low growth rate (0.12 μm/h) of AlInN is due to the necessary conditions for growth of sufficiently smooth and homogeneous AlInN layers. For HfO₂ in SiO₂/HfO₂ stacks, the maximum sputtering rate is only about 0.026 μm/h in the available system for this thesis. Fig. 2.5 shows the reflectivity simulations of quarter-wave stacks for AlInN/GaN DBRs and various oxide based DBRs. Here, the stopband is set to have a maximum reflectivity at a wavelength of 405 nm. In Fig. 2.5 a and b, a reflectance close to 100 % is possible for a number of Bragg-pairs above 45 for AlInN/GaN DBR or above 11 for SiO₂/HfO₂ DBR, respectively. On either side of the stopband, the reflectance decreases abruptly and shows oscillatory behavior. The width of the stopband width depends on the refractive index contrast between the two layers. With the thickness of an additional layer on top of the DBR one can tune the reflectance to a specific value. Fig. 2.5c shows the optimum reflectance of 45xAlInN/GaN DBRs compared with those of 14xSiO₂/Si₃N₄, 11xSiO₂/HfO₂, and 11xSiO₂/Ta₂O₅ DBRs.

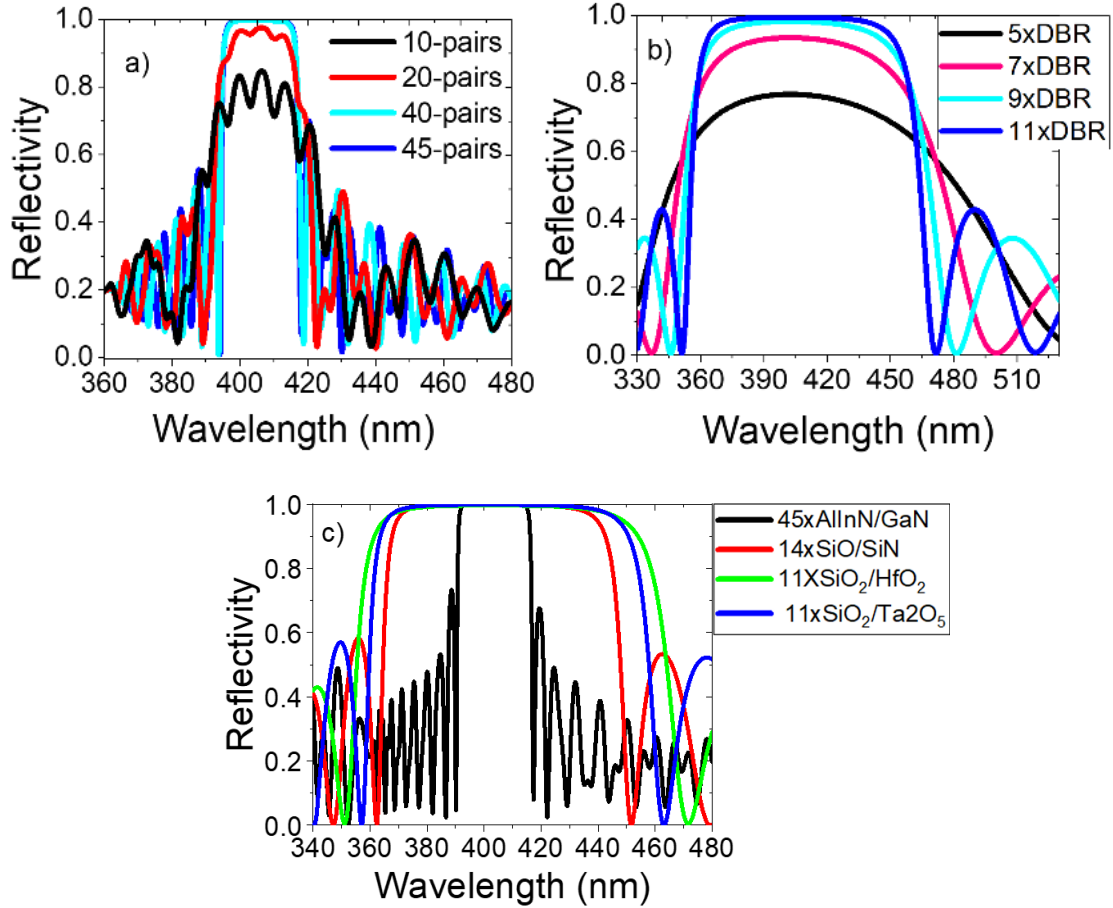


Fig. 2.5 Simulated reflectivities at about 405 nm wavelength for a) AlInN/GaN DBRs and b) SiO₂/HfO₂ DBRs for increasing numbers of layer-pairs, c) Simulated reflectance spectra for oxide DBRs and AlInN/GaN bottom DBR.

Reflectivities of a full 7λ cavity comprising 45xAlInN/GaN bottom DBR and 9xSiO₂/HfO₂ upper DBR with QWs inside are presented in Fig. 2.6. For the QWs, the imaginary part of the refractive index controls absorption or gain within the active region. Similarly, one can introduce losses into the DBR mirrors by adjusting the complex index of refraction. In DBRs, losses are either due to absorption or due to scattering at non-perfect interfaces. For the black curve, the reflectivity of a full cavity with QWs inside is simulated, where the material gain of the InGaN layers was set to be about 1000 cm^{-1} corresponding to a positive coefficient of $k = 0.0032$. For the red curve, this positive gain is offset by an optical absorption of 0.0016 ($\alpha_m \sim 500 \text{ cm}^{-1}$), where for example scattering within HfO₂ layers in the SiO₂/HfO₂ DBR layer stack was assumed. In this case, a reflectivity dip at the resonance wavelength is found. No lasing can be expected unless a sufficiently higher pumping power is applied to compensate the losses. The long cavity is necessary because of intra-cavity contacts that will be used in such GaN-based VCSEL.

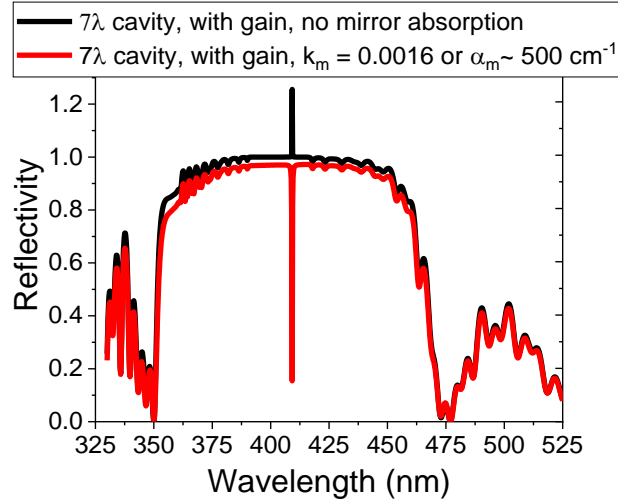


Fig. 2.6 Simulation of the full 7-lambda cavity of 45xAlInN/GaN bottom DBR and 9xSiO₂/HfO₂ upper DBR with QWs inside.

2.2.6 Optical loss effects in DBRs

If lossless materials are used, then the required reflectance can be achieved by a quarter-wave stack solely depending on the number of layer-pairs. For suitable transparent layers, the absorbance in the visible region of the spectrum can be negligible (less than 0.01%) [34] but in practice, the ultimate reflectance is limited by losses in the layers. The origin of optical losses in dielectric DBRs can be associated with scattering and absorption. Sources for absorption losses can be free carriers in doped materials or at heterojunctions whereas scattering may be introduced by rough interfaces or inhomogeneous layers [34]. In this work it is experimentally demonstrated (see chapter 6), for example, that optical absorption and scattering losses can be associated with n-type doping in AlInN/GaN DBRs. These loss mechanisms reduce the reflectance of the stack, leading to a reduction of the whole cavity performance and usually impair or inhibit lasing.

The simulation of the DBR reflectivity stopbands related to different values of absorption coefficients α show a rapid drop of the maximum reflectivity value at the stopband when absorption is increased as shown in Fig. 2.7. The effect of optical absorption on the maximum reflectivity for an AlInN/GaN DBR is represented in Fig. 2.7a while Fig. 2.7b shows a similar effect for oxide DBRs, SiO₂/HfO₂ as an example. As it can be seen, the peak reflectivity of the reference DBRs drops from maximum reflectance of ~100 % to about 86 % at $\alpha = 1000 \text{ cm}^{-1}$ when applied to the AlInN layers in 45xAlInN/GaN DBR stack (Fig. 2.7a). A similar

reflectivity drop is observed in 9xSiO₂/HfO₂ DBR stack when an absorption coefficient of $\alpha = 2200 \text{ cm}^{-1}$ for HfO₂ layers is applied (Fig. 2.7b). In addition, at each side of the peak reflectivity, the Fabry-Perot oscillations are significantly damped as absorption coefficients are increased. The large loss in reflectivity of about 15 % at $\alpha = 1000 \text{ cm}^{-1}$ is experimentally verified in highly Ge-doped AlInN/GaN DBRs (see chapter 6), where the quality of the DBR was strongly disturbed.

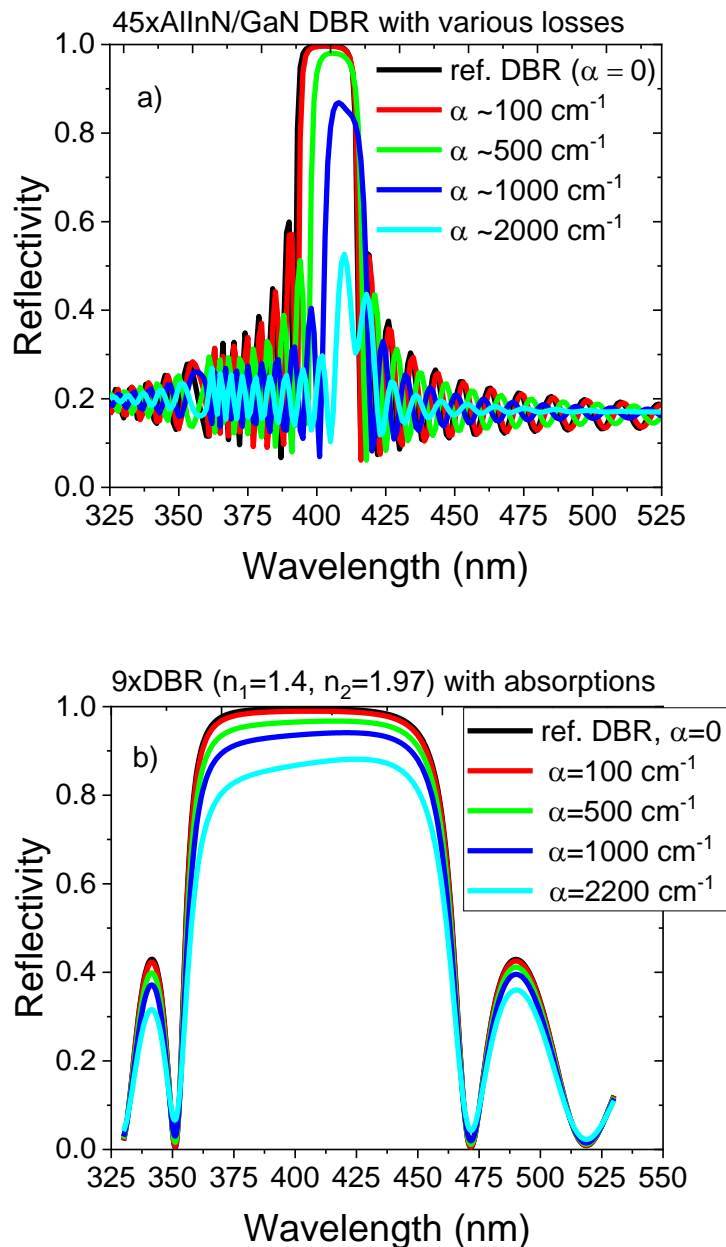


Fig. 2.7 The effect of absorptions and scattering losses in a) 45xAlInN/GaN DBR and b) 9xSiO₂/HfO₂ DBR.

2.2.6 Current transport and carrier injection for electrically pumped GaN VCSELs

For a well-designed GaN-based VCSEL, efficient carrier injection schemes must be developed enabling current densities of the order of several kAcm^{-2} . For an electrically pumped GaN-based VCSEL, carriers are injected by forward-biasing a p-n junction of a laser-diode. The electric field applied via the metal contacts must force the carriers into the center of the cavity region between the contacts. As the lateral hole transport is very limited due to the low hole mobility, any injection scheme without additional lateral current distribution mechanisms will most likely lead to strong lateral inhomogeneity of the current distribution and, therefore, to reduced optical gain. As one of such option, tunnel junctions can be employed on the p-type region whereby the lateral current distribution is achieved by the high electron mobility within the n-doped layer of the tunnel junction.

The current injection scheme of a TJ-GaN-based VCSEL with a dielectric top DBR is discussed in Fig. 2.8. Positive voltage is applied to the n-side of the TJ which puts the tunnel junction into reverse bias while the pn-junction across the MQW region is biased in forward direction as shown in the figure. Due to their high effective mass, holes have much lower mobility as compared to electrons. In p-n diode with a MQW active region, the hole transport reaches not very far from p-type region while electrons may overshoot from the n-side to the p-side region.

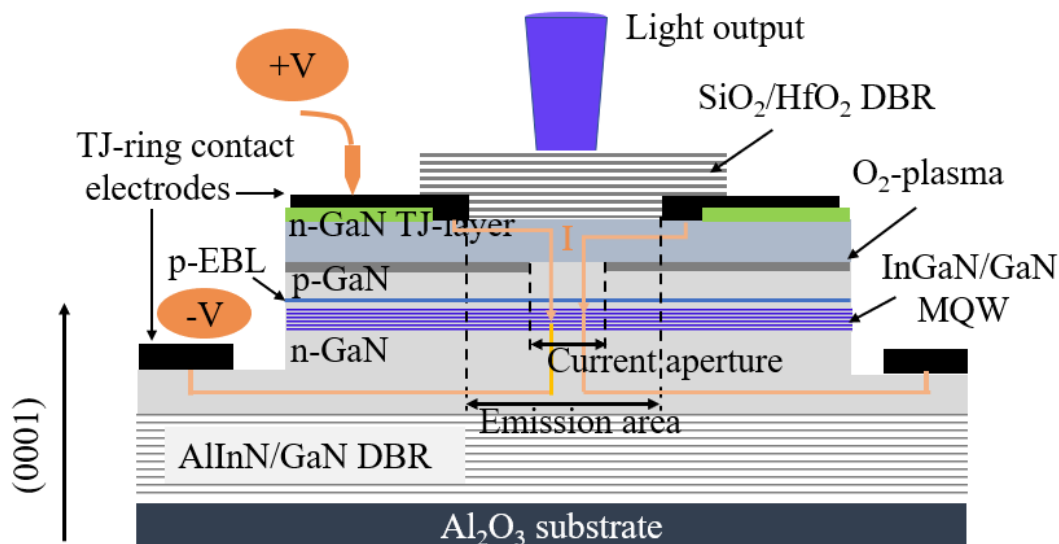


Fig. 2.8 Lateral and vertical current transport in a TJ-GaN-based VCSEL using intra-cavity electrical contacts.

This difference in electron versus hole transport, results in an optical emission from the QW nearest to the p-doped side but may also lead to potential optical losses in the QWs closer to the n-side due to insufficient population inversion. Also, the electron overshoot is known to cause electro-hole recombination in the p-region of the junction which lowers the injection efficiency as well. The design of the MQW region as well as the pn-junction itself has to take care of all these effects. Our design approach uses GaN barriers (~ 7 nm) that are slightly Si-doped to improve interfacial quality between well and barrier layers and also partially screens the QCSE [41-43]. An electron blocking layer (EBL) is implemented to account for the electron overflow over the barrier into the p-GaN.

2.3 Doping issues

The doping profile of the p-n junction is crucial to improve the light output of the quantum well region by avoiding absorption losses and to enable high injection levels, by allowing carrier transport with low series resistance. The basic theory of p-n junctions and tunnel diodes can be found in [22, 44]. This section of the work wants to discuss the Mg-doping of the p-type GaN in conventional LED devices and of GaN:Mg/GaN:Ge tunnel junction structures to be used in advanced LEDs and in VCSELs.

In GaN bulk material, Si and Ge have been proven well-suited shallow donor impurities with similar low activation energies between 17-19 meV below a doping level of 10^{19} cm^{-3} [45], leading to the ionization of all impurities at room temperature. A donor impurity concentration of about 10^{19} cm^{-3} corresponds therefore to a free electron concentration of $N_e \sim 10^{19} \text{ cm}^{-3}$, which is suitable for the n-side of a pn-junction device. However, for many GaN-based power electronic devices and optoelectronic devices a heavily n-doped GaN layer well above 10^{19} cm^{-3} is desirable, for example, for current spreading layers in tunnel junction devices, to reduce contact resistances or for conductive coatings. An option provides stress free GaN:Ge layers with carrier densities well above 10^{19} cm^{-3} that can be grown by MOVPE, while a doping concentration around $2 \times 10^{19} \text{ cm}^{-3}$ marks the upper limit for Si-doping, since higher doped GaN:Si layers usually tend to degrade [46-48]. In this work GaN:Si is used for the n-side region of LEDs and VCSELs while heavily Ge-doped GaN-layers (n^{++}) are grown on top of heavily Mg-doped p-GaN (p^{++}) realize tunnel junctions with excellent lateral current spreading on the p-side of the pn-junction device.

Mg is the only suitable acceptor impurity for p-GaN doping in group III-nitride based light emitting devices. However, the low hole mobility and maximum free hole concentrations well

below 10^{18} cm^{-3} for a Mg doping level of 10^{19} cm^{-3} are still problems to solve for MOVPE grown layers. These limiting properties of p-type GaN are caused by a large acceptor activation energy of about 170 meV and self-compensation effects at doping concentrations above 10^{19} cm^{-3} [19, 20, 49-51]. In addition, the low hole mobility and the comparably low electrical conductivity σ of p-GaN material hinders good current spreading for lateral injection [52, 53].

2.4 Tunnel junctions in GaN-based optoelectronic devices: Survey

To date, GaN-based tunnel junctions are largely used as an alternative for homogeneous current injection in many devices to improve performance [54]. Tunneling in semiconductor devices is a mature technology in many narrow bandgap devices with very thin depletion layer at the pn-junction interface enabling electrons to tunnel through it with large tunneling probability [22, 44]. However, tunneling is only little understood in wide bandgap devices [1, 4, 54, 55].

While it is difficult to obtain low resistivity values for GaN tunnel junctions (TJ) regardless of the used growth system (either MOVPE or molecular beam epitaxy or hybrid approaches), an InGaN-based tunnel junction increases absorption of visible light [54]. This tradeoff to achieve low resistivity and high transparency of the GaN-based tunnel junction complicates the device fabrication process. However, due to the advantages that tunnel junctions offer regarding current distribution in GaN-based devices, many research groups apply different approaches. Some combine heavy doping with InGaN heterojunctions [56, 57], others rely solely on heavy doping of GaN homojunctions [58-60]. The standard model for calculating the tunneling probability in such devices yield only very small values. For example, Neugebauer et al. [19] have calculated for a measured small depletion width of 10.7 nm a tunneling probability of about 10^{-27} in GaN:Ge/GaN:Mg tunnel junction diodes assuming Ge-donor and Mg-acceptor ionization energies of 19 meV and 185 meV [45, 61], respectively. This probability value is obviously too small to allow for substantial current transport. Nevertheless, demonstrated tunnel junction devices perform much better than to be expected from such basic model.

To date, a small number of reports on TJ-VCSELs based on GaN materials can be found [1, 4, 55] and none of these reports used GaN:Ge/GaN:Mg homojunctions. Aiming at a fabrication process of VCSELs employing GaN:Ge/GaN:Mg tunnel junctions, this work tries to take advantage of the feasibility of very high Ge doping concentrations in GaN in combination with engineered p-type doping to improve the tunneling process. The challenge is to grow a heavily

Ge-doped GaN layer on top of heavily Mg-doped p-type GaN in MOVPE, resulting in abrupt profiles. Previously, GaN:Ge/GaN:Mg tunnel junctions were applied to LEDs [19]. For the intended application in VCSEL devices, these tunnel junctions have to operate at current densities $>10 \text{ kAcm}^{-2}$ without large bias offset.

Chapter 3 Experimental procedures and material characterization methods

3.1 Materials growth

All samples for this thesis were grown on 2-inch c-plane sapphire substrates in an AIXTRON AIX200/4 RF-S metalorganic vapor phase epitaxy (MOVPE) reactor (Fig. 3.1). During growth, a LayTec EPI-curve[®] TT AR in-situ sensor monitors reflectance, temperature, and wafer curvature [18]. Apart from NH_3 as group-V precursor, the organic or inorganic sources of the standard precursors for III-nitride compounds and dopants are TMGa, TMIIn, TMAI, SiH_4 , Cp_2Mg , IBGe or GeH_4 , for growth of GaN, InN, AlN, and doping with Si, Mg, and Ge, respectively. The schematic gas flow in the MOVPE reactor is shown in Fig. 3.1 a and b.

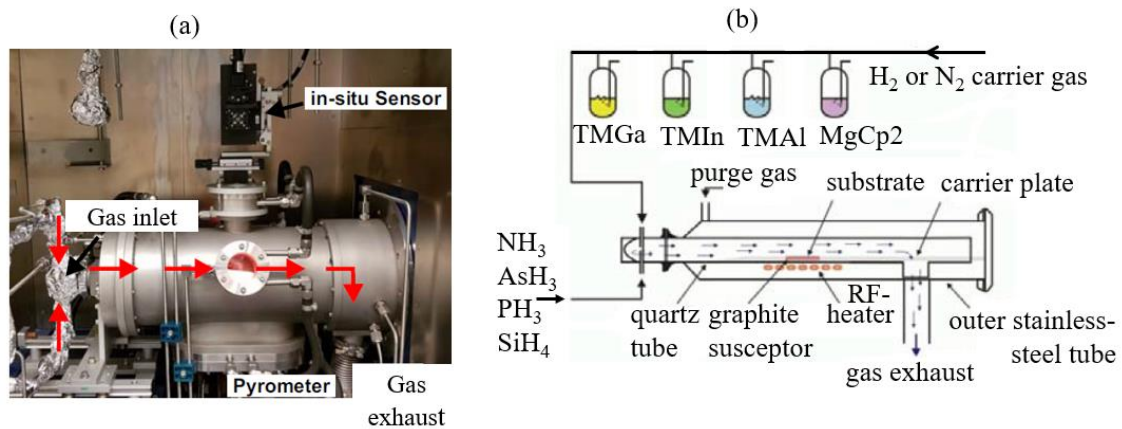


Fig. 3.1 (a) A photography of an AIXTRON MOVPE reactor and b) a scheme of gas flow in the reactor [27]

The buffer structure consists of a low temperature AlN nucleation layer followed by 200 nm AlN grown at high temperature, a 100 nm AlGaIn compositionally graded layer, an in-situ SiN mask for defect reduction and a 3 μm thick undoped GaN buffer layer. A scheme of the epitaxial structures for GaN-based LEDs and VCSELs is presented in Fig. 3.2. For growth of conventional LEDs (Fig. 3.2a1), Mg-doped p-type GaN is grown on top of MQW structures following a Si-doped n-type GaN layer. For TJ-LEDs, an additional Ge-doped GaN cap layer is grown on top of GaN:Mg (Fig. 3.2a2). For VCSELs, a similar active region as for LED-layers is grown on top of AlInN/GaN DBRs but its spectrum tuned to overlap with the desired cavity resonance and the vertical position of the quantum wells chosen to be at the antinodes of

the wave function (Fig. 3.2b). The laser structures were designed as hybrid VCSELs with an epitaxial bottom DBR and a dielectric top DBR that is deposited in the final processing step.

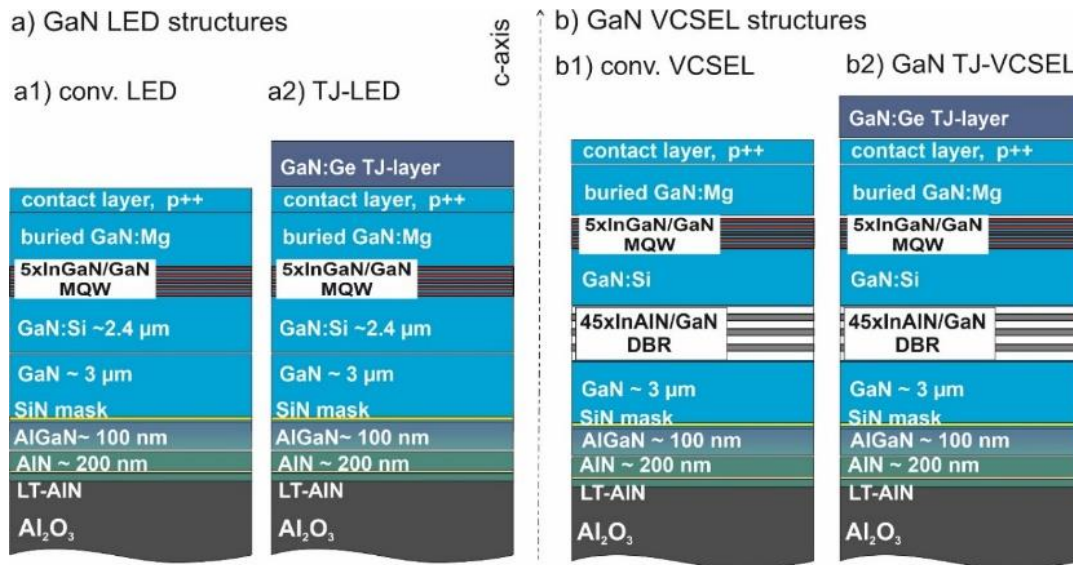


Fig. 3.2 Epitaxial layer structure for typical a) GaN-based LEDs and b) GaN-based VCSELs.

3.2 Characterization methods

Before fabrication of devices, samples were characterized by different methods. The surface morphology and the structural quality are, for example, analyzed using atomic force microscopy (AFM) and scanning electron microscopy (SEM). High-resolution X-ray diffraction (HRXRD) measurements are used to determine layer thicknesses, composition, and crystalline quality. The reflectivity spectra of the DBRs are measured by a Shimadzu UV-VIS-NIR-photospectrometer using a calibrated mirror with reflectivity higher than 99.8 % for wavelengths between 310 and 450 nm as reference.

To analyze the electrical properties of the p- and n-region such as doping concentrations, sheet resistivity, and mobility Hall effect measurement was used. Photoluminescence (PL) and electroluminescence (EL) were used to assess the emission characteristics of the samples. Hall effect measurements were called out for the assessment of carrier transport namely carrier mobility, conductivity, and carrier concentrations in doped material. Transmission line measurements (TLM) were conducted to study the metal-semiconductor contact behavior and to extract specific contact resistance material resistance.

In addition to the study of surface morphology and layer structures quality of samples by SEM, the latter and other surface profile-meter equipment were also used to measure qualitatively the

etching depth after mesa fabrication. A complete device is characterized either by continuous wave I-V measurement using Keithley 4200-SCS semiconductor parameter analyzer or by pulsed I-V measurements at room temperature. In addition, EL measurements at various injection current densities were conducted to study the emission wavelength spectra and linewidths of fabricated VCSELs.

Chapter 4 Approaches for current injection

4.1 Current distribution: ITO vs. GaN:Ge

After growth of the GaN-based VCSEL structure, micrometer sized devices were processed by photolithography. For this, contact areas and electrical injection paths have to be defined and the top mirror layers must be deposited above the cavity. This is performed step-by-step by lithographic processing using different layers of lithographic masks. Structural features like mesas are transferred onto the wafer by coating the wafer with photoresist and subsequent UV-exposure. However, due to the multiple alignment steps and limited resolution of the photoresist, the positioning of accuracy of the succeeding steps is about 1 μm , thus limiting perfect alignment for smaller device structures. Nevertheless, it is possible to reproducibly process a device with an injection area diameter of 2 μm and larger, which is a good range for GaN-based VCSEL fabrication.

The processing was done on quarter piece of 2-inch wafers. p-GaN for conventional devices was activated in a rapid thermal annealer (RTA) before further processing while for tunnel junction devices activation was done after mesa etching because the n-type GaN:Ge-capping layer inhibits hydrogen diffusion so hydrogen can only pass via the side-walls of an etched mesa [19]. The next step was cleaning in acetone, isopropanol and DI-water using an ultrasonic bath. The sample was then spin-coated either with positive resist for mesa masking or with negative resist for material deposition. A so-called soft bake was done prior to the UV-light exposure (see parameters on Appendix A).

Before exposure, the wafer was aligned to the previous lithography layers using alignment markers. For steps involving negative photoresist post-bake step was applied. Lithography ended with a developer chemical to remove resist from exposed areas, as an example see Fig. 4.1. Upon developing exposed areas, either etching or material deposition followed. For the formation of mesa structures and alignment markers (Fig. 4.1a), structures are etched by inductively coupled plasma reactive ion etching (ICP-RIE). Contact metals are deposited by electron-beam and thermal evaporation after lithographic steps defining the n- and p-type contact areas (Fig. 4.1b). In this work, ohmic-metal contacts to n-GaN layers and to indium-tin-oxide (ITO) layers were realized using Ti/Al/Ni/Au (14 nm /30 nm /10 nm /60 nm-thick, respectively) while ohmic contacts to p-GaN were realized by oxidized Ni/Au (10 nm /10 nm-thick) contacts. In some cases, different pretreatment types prior to metallization or TJ

overgrowing were investigated such as O₂ plasma treatment of p-GaN layer for passivation. Tetramethyl ammonium hydroxide (TMAH) was used for treatment of GaN:Ge sidewall-etch facets prior to ITO layer deposition for lateral current injection. The upper dielectric mirror is deposited using a reactive magnetron sputter process (for SiO₂/HfO₂ DBR).

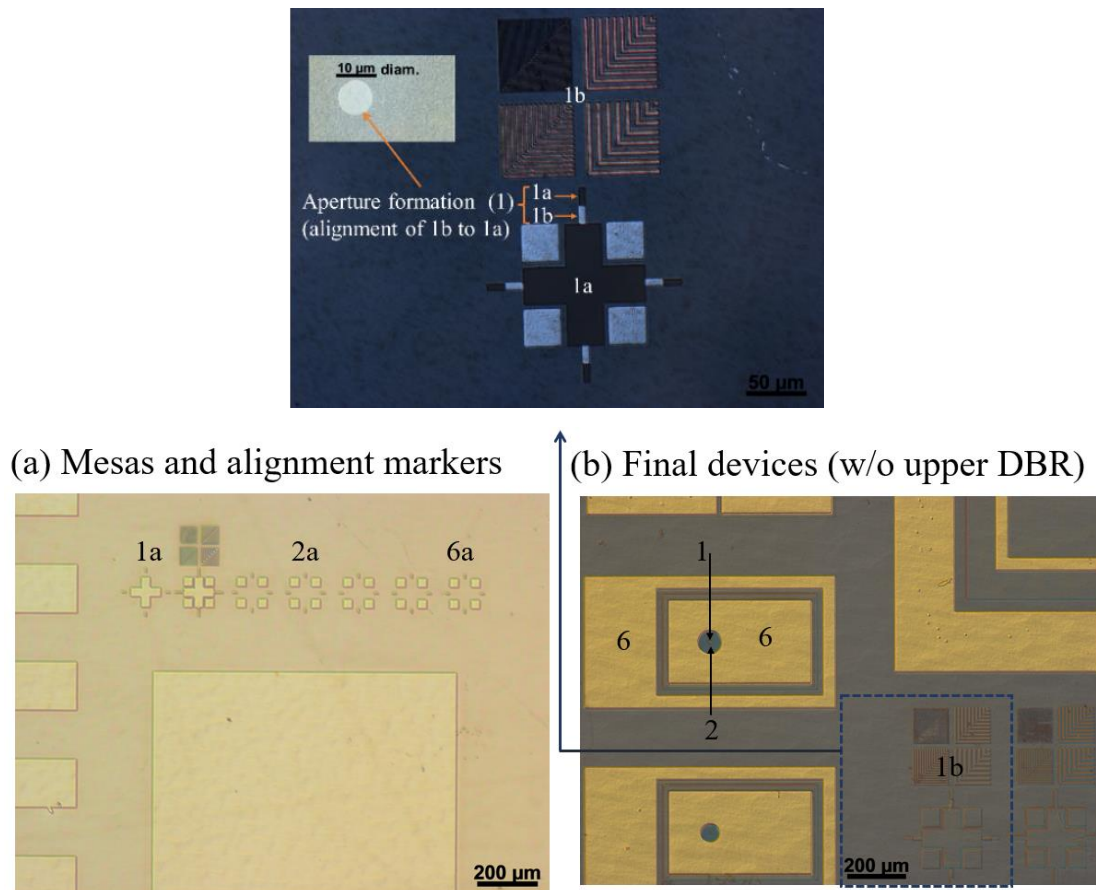


Fig. 4.1 Photography to illustrate alignment procedure. a) Alignment marker structures on a quarter wafer (2-inch) with mesa etching and b) final structures realized after several consecutive alignment steps (e.g., alignments 1b, 2b, ...6b to the markers 1a, 2a, ...6a for formation of apertures (1), passivation (2), ... TJ-contact metals (6), respectively). Zoomed view of the first alignment to design apertures for lateral current injection (top image).

4.2 Current aperture design approaches

Different current confinement schemes for lateral and vertical injection in tunnel junction VCSELs were explored in this work in order to determine their suitability for VCSEL fabrication and to compare their characteristics to that of oxide-confined current aperture approaches for conventional ITO VCSEL [1, 4, 21, 60]. The processing steps of these apertures

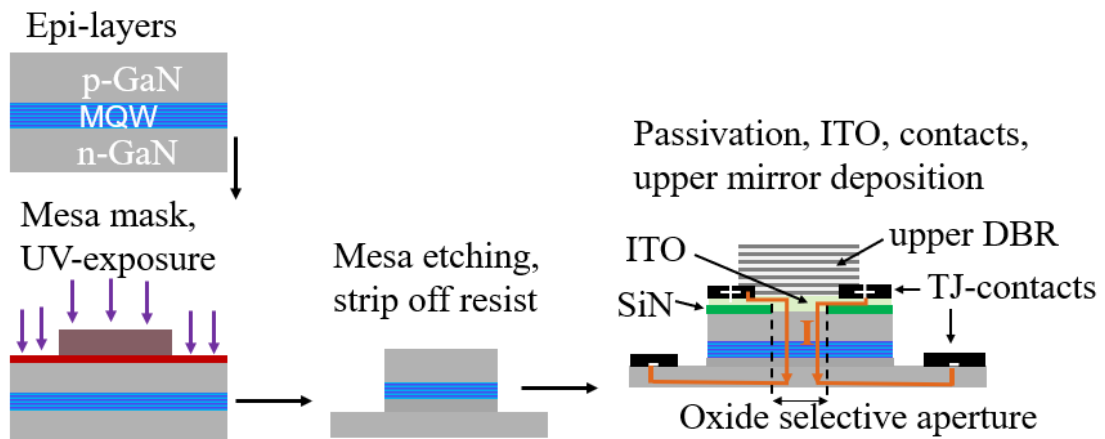
are illustrated in Fig. 4.2. Since ITO is an n-type semiconductor with a carrier density of up to $n \sim 10^{20} \text{ cm}^{-3}$, also ITO on top of p-GaN can be regarded as a tunnel junction contact like epitaxial GaN:Ge on top of p-GaN. For the first approaches (Fig. 4.2a), the current is vertically injected through the small aperture region within either an insulating SiN-layer or SiO₂-layer.

The additional GaN:Ge cap layer can be added on top of p-GaN layer in two ways. For a current aperture formed by a selective area growth process (SAG-approach) for the tunnel junction VCSEL, a GaN:Ge cap layer is overgrown on top of a plasma passivated GaN:Mg surface forming a thin oxide aperture (Fig. 4.2b). The plasma passivation allows vertical current only to pass the GaN:Ge/GaN:Mg interface within the unpassivated area of the aperture. For a second passivation approach in TJ-VCSELs, the additional GaN:Ge layer is directly grown on top of the GaN:Mg layer without any growth interruption. An aperture can be formed by etching GaN:Ge layer and additional passivation of the GaN:Mg layer. In this approach, the passivation is such that lateral current only passes through the sidewalls of the etched GaN:Ge and then reaches the GaN:Ge/GaN:Mg interface of the aperture as presented in Fig. 4.2c. An ITO layer on top of passivated GaN:Mg layer is used to form the contact to the etched GaN:Ge sidewalls. Positive voltage is applied to the n⁺ ITO-layer (for approaches in Fig. 4.2 a and c) or to the n⁺ tunnel layer (for SAG-approach, Fig. 4.2b) which puts the TJ into reverse bias while the pn-junction across the MQW region is biased in forward direction in all approaches.

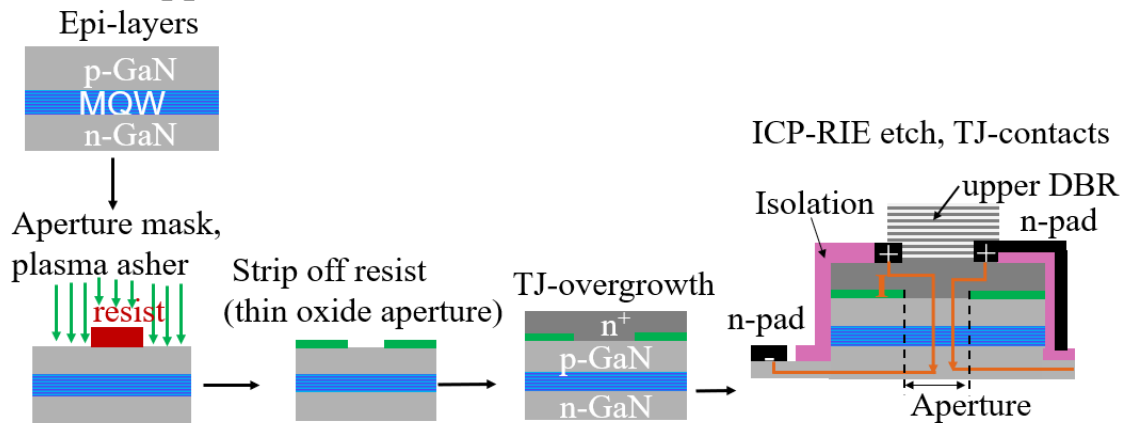
Even though the oxide aperture methods in Fig. 4.2a and SAG-approaches for TJ (Fig. 4.2b) are practical for most VCSEL confinement structures, several reports demonstrated that the oxide apertures increase thermal resistance inside the device, causing internal strain which degrades device reliability [62-64]. Other thermal effects include the cavity resonance shift to longer wavelengths (red shifts). Current aperture methods as investigated here for TJ-VCSELs take advantage of highly transparent n-GaN cap layers [1, 4] opposite to the light absorbing ITO-layers typically employed for GaN-VCSELs [4, 21].

A high accuracy of the aperture size is extremely important for the lateral injection approach in order to properly connect to the sidewalls. In addition, a smooth sidewall of the etched facets (see Fig. 4.2c) is required to further improve metal-sidewall contacts and probably to reduce current crowding issues due to inhomogeneity of current injections. Therefore, different approaches were investigated to reduce sidewall defects induced by etching and to smoothen

a) Oxide aperture for ITO-VCSEL



b) SAG – approach for TJ-VCSEL



c) Passivation approach for TJ-VCSEL

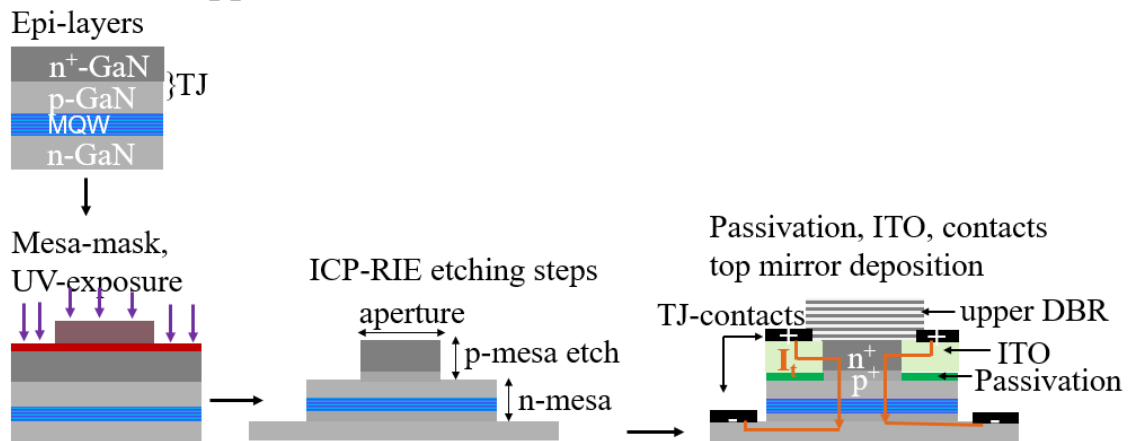


Fig. 4.2 Current injection schemes for GaN-based VCSEL and fabrication steps for a) ITO-VCSEL, b) SAG-approach and c) passivation approach for TJ-VCSELs.

sidewalls such as increasing the ICP power used for dry etching and an additional wet chemical treatment after etching by tetramethyl ammonium hydroxide (TMAH) [64]. The lithography to achieve smooth sidewall facets of the p-GaN mesa for lateral injection is very challenging. The TMAH treatment (Fig. 4.3a) requires the use of a hard mask (e.g., Ni-mask) to protect the aperture surface because TMAH reacts with any exposed GaN material, resulting in decorated defects which may increase scattering losses. The additional masking leads to a slight increase of the aperture size as compared to the initial aperture size, which must be taken into account. The aperture size increases by around $0.5\ \mu\text{m}$ in diameter. In the first experimental test, the top p-GaN surface was covered with a $100\ \text{nm}$ thick SiN passivation layer after mesa etching, which covers the sidewall as well. However, after aperture opening by etching with SF_6 as dry etching gas, the SiN layer on the aperture-edge was not etched, resulting in a coating of the sidewall facet and an aperture ring dx (see dark contrast of Fig. 4.3b). The additional steps required to obtain smoother sidewalls are mainly sources of dimension losses of the aperture size during processing.

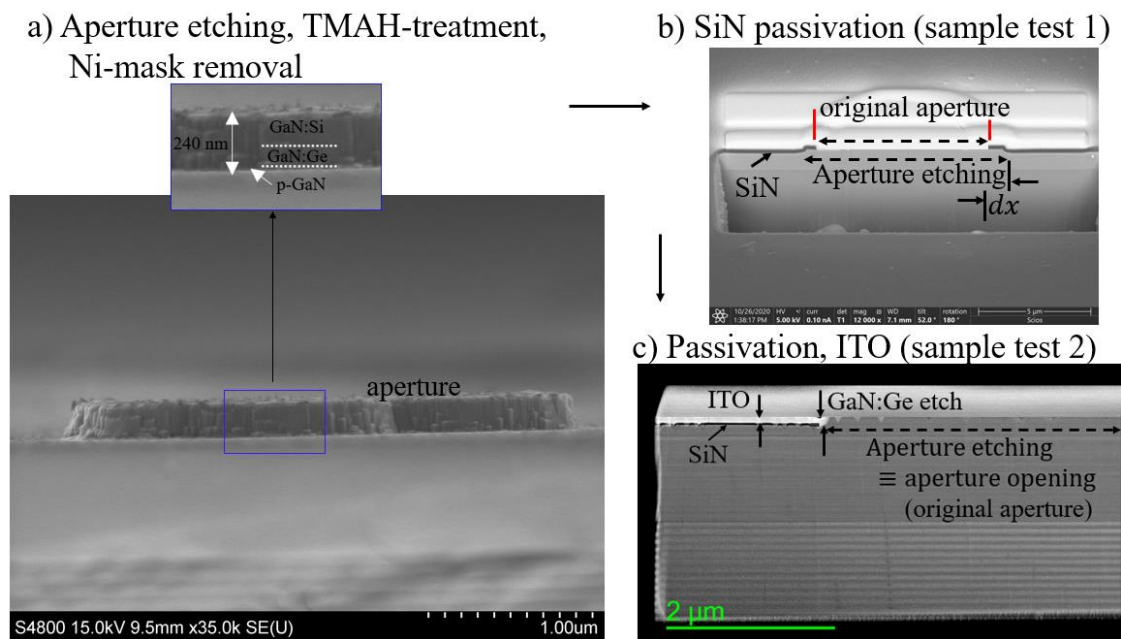


Fig. 4.3 a) A side view SEM image of an etched aperture after TMAH treatment. b) SEM image showing size reduction of an original aperture due to the processing conditions and c) SEM image for optimized process parameters to fit an aperture opening with the original aperture by dry-etching for lateral current injection scheme.

Nevertheless, the aperture size increase of $0.5\ \mu\text{m}$ could be counterbalanced by a small adjustment of lithographic parameters (Fig. 4.3c). For satisfactory results, the exposure time

was increased from 1.5 to 2 s at 22 mW/cm², while the development time was decreased from 30 to 25 s for negative resist. Subsequently, after SiN passivation, the lithography for aperture opening employed positive photoresist (Ma-P1240) at the standard exposure parameter (70s at 22 mW/cm²) and an increased development time (from 40 to 60 s in Ma-D331 developer).

4.3 Summary

This chapter discussed different lithographic steps used to process GaN-based structures on quarter pieces of 2-inch wafers by including current injections confinement, contact metal deposition and upper mirror deposition for GaN-based VCSELs. Different current confinement schemes for lateral and vertical injection in TJ-VCSELs were discussed and compared with the oxide-confined current aperture approach for conventional ITO-VCSELs. The aperture designed by passivation approach for TJ-VCSELs can be more beneficial for current distribution as compared to the oxide-confined current aperture for ITO-VCSELs or to selective area overgrowth approaches for TJ-overgrown VCSEL structures. The additional approaches to reduce sidewall defects as induced by dry etching and to smooth sidewalls require a high accuracy of aperture size, which can be realized using optimized process parameters.

Chapter 5 Development of VCSEL structures

5.1 GaN:Mg/GaN:Ge tunnel junctions

5.1.1 Optimization of Mg-doping in p-type GaN for tunnel junctions

The electrical characteristics of GaN-based TJ-LEDs depend on several factors like hole concentration in the p-type GaN layer, the doping profile of the p^{++}/n^{++} tunnel junction, or the contact resistance of the metal contacts. Maximum light output can only be obtained with optimized I-V characteristics. The optimization strategy was relying on a study of the electrical and optical properties in dependence of the growth sequence and of the acceptor activation within the Mg-doped layers within the tunnel junction region. Mg-doping was done by supply of the metalorganic precursor (Bis-)cyclopentadienyl-Magnesium (CpMg).

Table 5.1 and Fig. 5.1 summarize results of Hall effect measurements such as the sheet resistivity (R), hole concentration (p) and hole mobility (μ) of p-GaN layers for varying CpMg-fluxes. The GaN growth rate was kept at $0.6 \mu\text{m/h}$ which ensures smooth surface morphologies for growth temperatures around $800\text{-}850 \text{ }^\circ\text{C}$. Around 1 sccm CpMg flow, the lowest resistivity and highest hole concentration was obtained while the carrier mobility slightly decreases with increasing doping concentrations. A hole concentration of $5.5 \times 10^{17} \text{ cm}^{-3}$ and a low resistivity of $0.84 \Omega\text{cm}$ were achieved with Mg-concentration of around $2 \times 10^{19} \text{ cm}^{-3}$. The observed hole concentration values of the p-GaN layers are in good agreement with the previously reported values by Kaufmann et al. [51] and Kozodoy et al. [66].

Improved contact resistances to p-GaN layers were achieved by exceeding the optimum precursor flow for bulk GaN layers by a factor of 4 for about the last 15 nm layer thickness. This p^{++} contact layer does not change the results of the Hall-effect measurements but improves the linearity of the I-V curves across the metal contacts for the Hall measurements. For thicker layers doped at such CpMg flows, an abrupt increase in series resistance and a decrease of the carrier concentrations were observed accompanied by the appearance of inversion domains.

As shown in Fig. 5.2, photoluminescence features in the spectra of GaN:Mg are characteristic for specific Mg-concentrations and can be related to free hole concentrations by comparison to measured Hall data for the same sample. The absolute intensity of a blue luminescence (BL) band around 400 nm wavelength is a fingerprint for free hole concentrations as confirmed by

Table 5.1 Sample series to optimize Mg-doping in p-type GaN layer.

CpMg-flow (sccm)	R (Ωcm)	μ (cm^2/Vs)	P (cm^{-3})
0.25	1.03	18	3.3×10^{17}
0.75	0.95	14	4.6×10^{17}
1	0.84	13	5.5×10^{17}
2	1.14	12	5.0×10^{17}
4	1.5	10	3.8×10^{17}

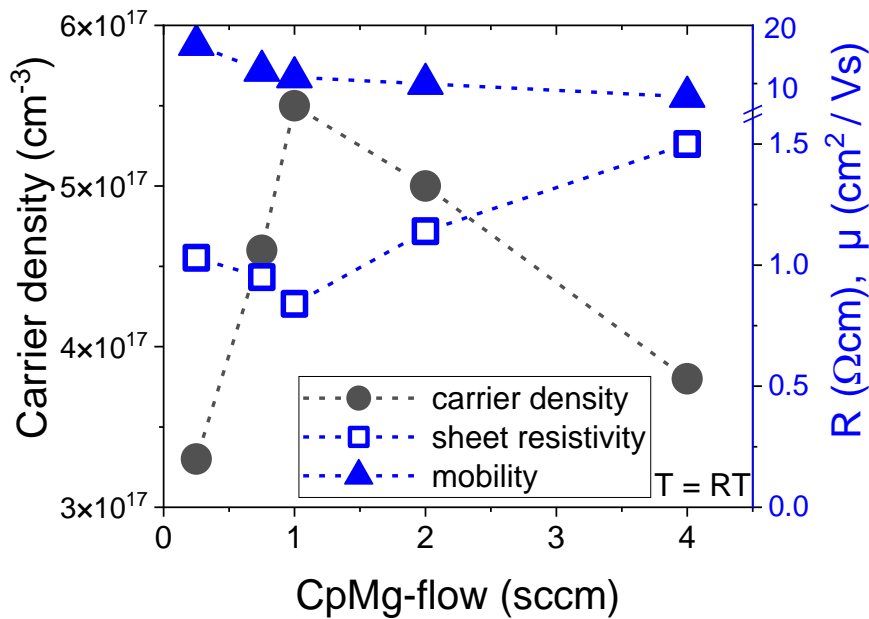


Fig. 5.1 Hole concentration, mobility and resistivity of p-GaN versus CpMg-flow rate. The dashed line connecting data points are only guides to the eye. The optimum values for bulk GaN:Mg layers are found for an CpMg-flow of 1 sccm.

the Hall effect measurements addressing the maximum intensity to $[p] = 5.5 \times 10^{17} \text{ cm}^{-3}$ and $[\text{Mg}] \sim 2 \times 10^{19} \text{ cm}^{-3}$. A broader luminescence band at longer wavelengths ($\sim 450 \text{ nm}$) appears when the Mg concentrations in thicker layers exceeds the optimum value. It is also connected with the inversion domains that start to appear (see Fig. 5.3). Different explanations for the origin of the blue luminescence (BL) in highly p-doped GaN layers ($[\text{Mg}] > 10^{19} \text{ cm}^{-3}$) were discussed in various reports, addressing it to a recombination between deep donors and Mg acceptors (donor-acceptor pair transitions) [67-69].

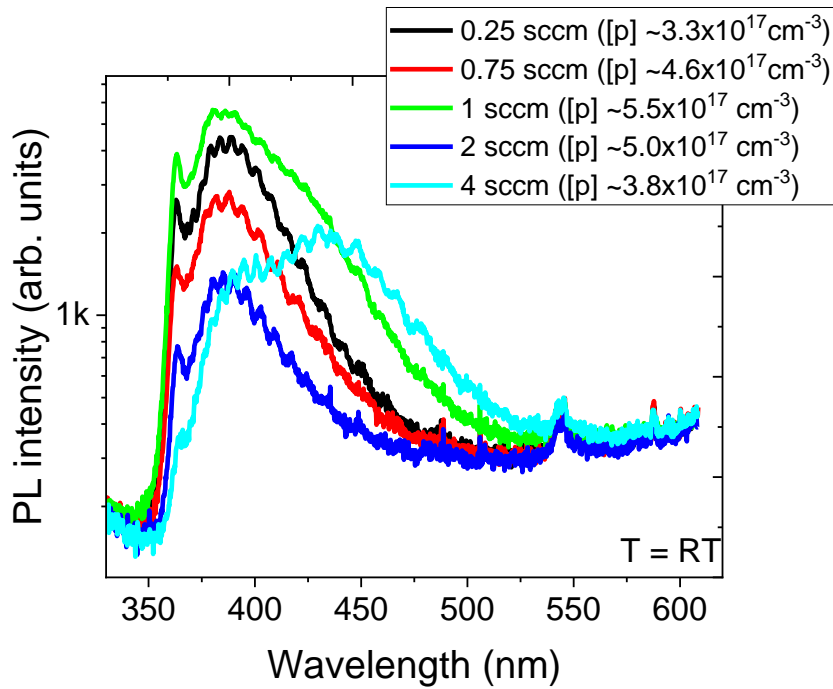


Fig. 5.2 PL intensity of p-GaN doped with various Mg concentrations.

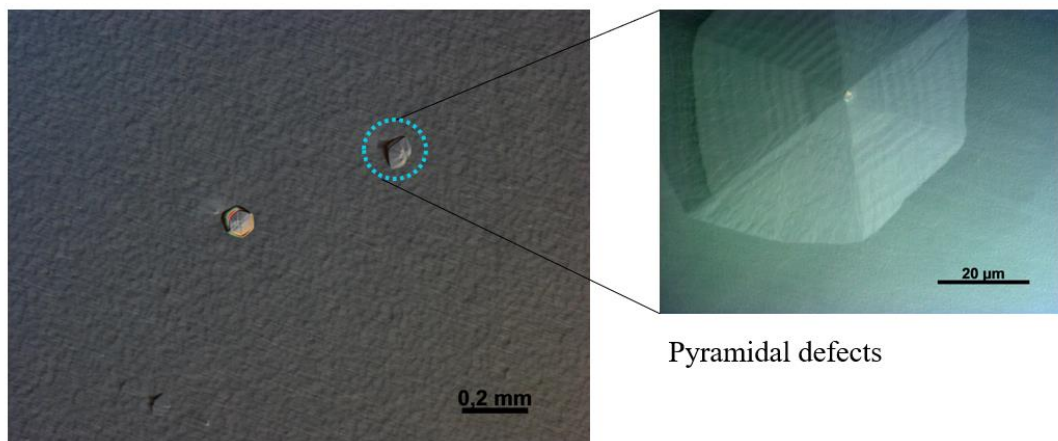


Fig. 5.3 Nomarski microscope image of the GaN:Mg surface for Mg-doping (at high C_{pMg} -flow) of a bulk GaN layer as used for the contact region. Zoomed view of an inversion domain-related pyramidal defect.

5.1.2 Comparison of large-area LEDs and TJ-LEDs

In tunnel junction LEDs, the GaN:Mg layer is buried underneath a GaN:Ge layer ($[n] \sim 10^{20} \text{ cm}^{-3}$) which prevents hydrogen diffusion towards the surface. For efficient p-GaN activation, the buried GaN:Mg layer in TJ-LEDs must be thermally activated after etching in order to allow hydrogen diffusion through the etched mesa-sidewall [19]. Conventionally, GaN:Mg of

standard LED can be activated before mesa-etching since hydrogen can be released via the wafer surface. Here, a rapid thermal annealing (RTA) was used for acceptor activation. For the metal contacts to p-GaN, e-beam evaporated Ni/Au (10 nm / 10 nm) layers and RTA-treated for 5 min in O₂ atmosphere were used. Note that this contact exhibits significant light absorption. A Ti/Al/Ni/Au (14/33/10/60) nm metal stack was deposited on n-GaN as a surrounding frame around the mesa for the n-contact. In case of TJ-LEDs, the n-contact to the top GaN:Ge layer of the LED structure was also only a frame covering a small outer area hereby avoiding absorption losses. The thickness and doping parameters for the p-region of all LEDs in this study are presented in Table 5.2. The full LED structure is shown as inset of Fig. 5.4.

For optimization of TJ-LEDs, first the L-I-V characteristics for various CpMg-flows at the p⁺⁺/n⁺⁺ junction were analyzed using the sample series as described in Table 5.2. This is necessary as the details of the dopant distribution were only vaguely accessible by depth resolving methods such as SIMS. In this series, the CpMg-flow during growth of the buried 200 nm thick p-type GaN was fixed at 0.75 sccm ($[p] = 4.6 \times 10^{17} \text{ cm}^{-3}$) while the doping during growth of the 15 nm thick GaN:Mg layer at the junction were corresponding to CpMg-flows of 0.75, 1.5 and 3 sccm for TJ-LED₁, TJ-LED₂, TJ-LED₃, respectively. The IBGe flow in the subsequently grown 100 nm thick GaN:Ge cap layer was fixed at 0.75 sccm ($[n] > 10^{20} \text{ cm}^{-3}$) for all TJ-LEDs. The CpMg-flow at the contact layer of a reference standard (std) LED was also 3 sccm (cf. TJ-LED₃).

For all LEDs in this sample series, the maximum room-temperature photoluminescence intensity from the MQW region was found to be at about 450 nm wavelength. The L-I-V characteristics of LEDs in this series (std-LED, TJ-LED₁₋₃) are presented in Fig. 5.4. Light output of TJ-LEDs was always larger than for the std LED since an oxidized Ni/Au contact is less transmissive than GaN:Ge layers at these wavelengths. The additional thin p-GaN region with increased Mg concentration decreased the forward series resistance and lowered the turn-on voltage ($V_{\text{on}} \sim 4 \text{ V}$) for TJ-LED₃ as compared to ($V_{\text{on}} \sim 5 \text{ V}$) of the other two TJ-LED_{1,2}. However, the light output power of TJ-LEDs also decreased by about 25 % (at 0.1 A) when the CpMg-flow was increased by a factor of 4 (from 0.75-3 sccm). As can be seen in Fig. 5.4, the thin layer with increased Mg-doping at the TJ-interface is crucial for the efficiency of the tunneling process. By comparing std-LED devices with TJ-LED₃ devices, the similar Mg-doping (3 sccm) at either the interface to the Ni/Au metal contact or at the tunnel junction to

Table 5.2 Sample structures to optimize Mg-doping in 1 mm² std-LEDs and TJ-LEDs.

Sample number	Buried GaN layer structure, p		Contact layer structure, p ⁺⁺		GaN:Ge capping layer structure, n ⁺⁺	
	Thickness (nm)	CpMg-flow (sccm)	thickness (nm)	CpMg-flow (sccm)	thickness (nm)	IBGe-flow (sccm)
std-LED	200	0.75	15	3	none	none
TJ-LED ₁	200	0.75	15	0.75	100	0.75
TJ-LED ₂	200	0.75	15	1.5	100	0.75
TJ-LED ₃	200	0.75	15	3	100	0.75

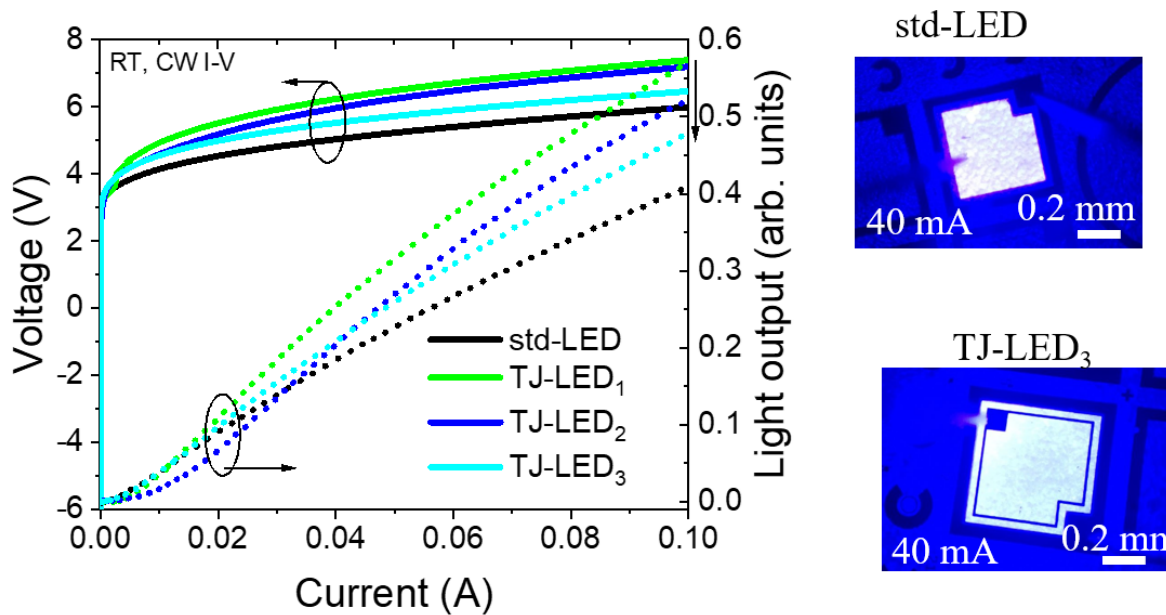


Fig. 5.4 The L-I-V characteristic of 1 mm² LEDs for an increased CpMg-flow either at the interface to the Ni/Au contact (std-LED) or at the TJ-interface to the GaN:Ge layer (left). Images of the LED emission at 450 nm wavelength at 40 mA current (right).

GaN:Ge, leads to a comparable turn-on voltage of ~ 4 V in the I-V characteristic for std-LED devices and TJ-LED₃ devices but with nearly 20 % more brightness for TJ-LED₃ devices (also visible by the microscopic images in Fig. 5.4, right side). In addition, both LEDs have similar low series resistances, resulting at a current of 0.1 A in operating voltage of 6 V for the std-LED devices and 6.5 V for the TJ-LED₃ devices, respectively. Furthermore, a better I-V characteristic of LED was achieved for further increase of CpMg-flow at both buried p-GaN layer and p⁺⁺-contact layer. The additional LEDs, std-LED2 and TJ-LED4, were grown with CpMg-flow of 10 sccm at the buried p-GaN layer and high Mg concentration (400 sccm flow) at the p⁺⁺-contact layer. At this doping scheme, both LEDs exhibit a low turn-on voltage of 2.8

V and 3.4 V for std-LED2 and TJ-LED4, respectively, with a similar series resistance of about $1 \times 10^{-4} \Omega \text{cm}^{-2}$ (Fig. 5.5). This showed both the contact resistance and the tunneling can be strongly improved by excessive Mg doping in thin layer regions. Although TJ-LED4 is still brighter than std-LED2, the respective light output for both types of LEDs drops to around half of the intensity of the previous samples (Fig. 5.4), probably due to the change of the GaN-crystal quality at the p^{++}/n^{++} -layer interface due to the increased Mg-doping at the p^{++} -contact.

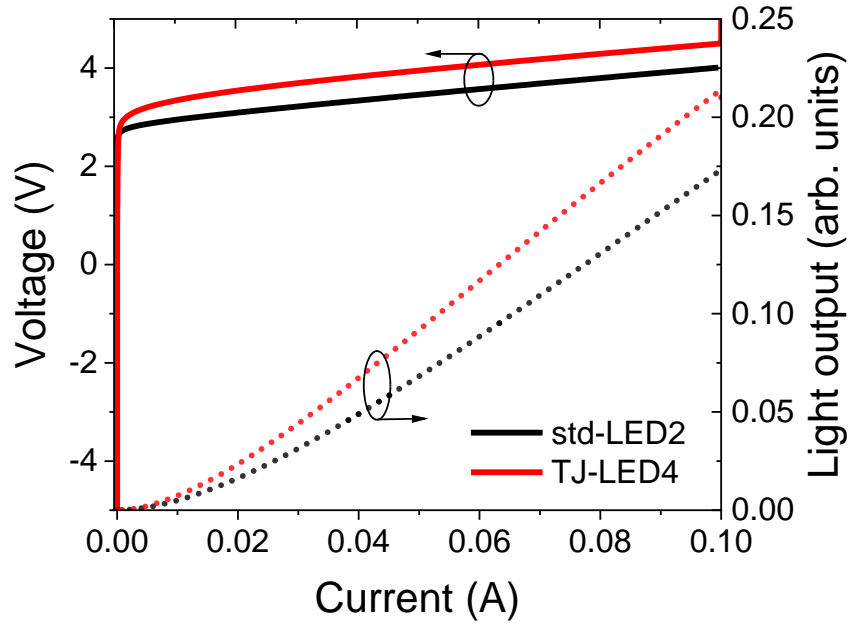


Fig. 5.5 I-V characteristics for 1 mm² std- and TJ-LEDs exhibiting a reduced resistance at the tunnel junction contact using excessive CpMg-flow within a thin GaN:Mg region at the junction.

The L-I characteristic is dependent on the internal quantum efficiency (IQE) and external quantum efficiency (EQE) of an LED. The EQE of an LED is defined as the ratio of the number photons emitted from the surface of an LED to the number of electron-hole pairs as generated by the injected current and can be therefore calculated as:

$$\begin{aligned}
 \text{EQE} &= \frac{\text{number of emitted photons outside an LED}}{\text{number of } e - h \text{ pairs injection}} \\
 &= \frac{\text{measured light output of the LED device}}{\text{current density}}
 \end{aligned} \tag{5.1}$$

Fig. 5.6 shows the EQE of reference LED structures presented in Fig. 5.4 with the CpMg flows as presented in Table 5.2. The peak IQE is calculated using the experimental data for the EQE. The calculation is based on an interpolation of the recombination rate equation at maximum EQE with ABC + f(n) model by Dai et al. [70] and Nippert et al. [71, 72] which yields the following expression.

$$IQE_{\text{peak}} = \frac{Q\text{-value}}{Q\text{-value} + 2} \quad (5.2)$$

where the value of the parameter Q can be found by a least-square fitting of the interpolated ABC + f(n) data [70]. As expected, the EQE of TJ-LED₃ at the current density of 10 Acm⁻² is also 30 % higher than the EQE of reference std-LED (Fig. 5.6a). The increase of EQE for the TJ-LEDs is caused by a higher light extraction efficiency (LEE) due to a lower light absorption of the GaN:Ge spreading layer and lower optical loss by thermal quenching. The absorption coefficients of GaN:Ge layer and oxidized Ni/Au contact layer in the spectral range of 420-450 nm wavelength were determined from separate optical measurements to be around 115 cm⁻¹ for GaN:Ge layer ([n] ~ 1x10²⁰ cm⁻³) corresponding to an absolute absorption value < 1 % by a 100 nm GaN:Ge layer, while about 50 % absorption losses occur for a Ni/Au contact.

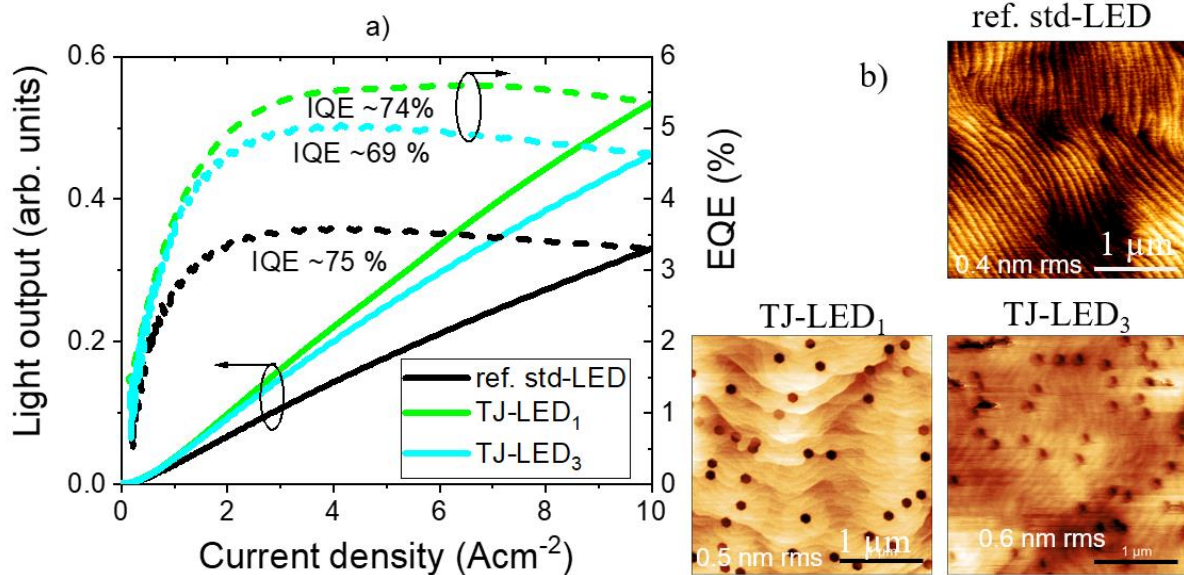


Fig. 5.6 a) EQE-L-J characteristics for std- and TJ-LEDs according to table 5.2 b) AFM image of these LEDs illustrating the size increase of V-pits upon GaN:Ge growth. The EQEs for std-LEDs are mainly lowered by the absorption of Ni/Au contacts.

In addition, V-shaped pits present on GaN:Ge surfaces grown in nitrogen ambient may increase the escape probability of photons. Interestingly, the IQE is almost equal for both LEDs

indicating a similar carrier injection into the MQW region. The remaining slight reduction of the IQE for TJ-LEDs is perhaps due to the increase of the width of the pits by the GaN:Ge layer grown under nitrogen. Dislocations manifest in AFM images (Fig. 5.6b) where growth steps disappear or coalesce (mixed and screw dislocations) or where depressions occur (edge dislocations) [73-75]. During GaN:Ge growth under nitrogen these V-pits grow in size with increasing layer thickness. While it is possible to avoid the size increase of V-pits by growing GaN:Ge in hydrogen and/or at a temperature above 1000 °C its applicability has to be checked with regard to the MQW properties.

5.1.3 Tunnel junction micro-LED structures combined with current aperture approaches

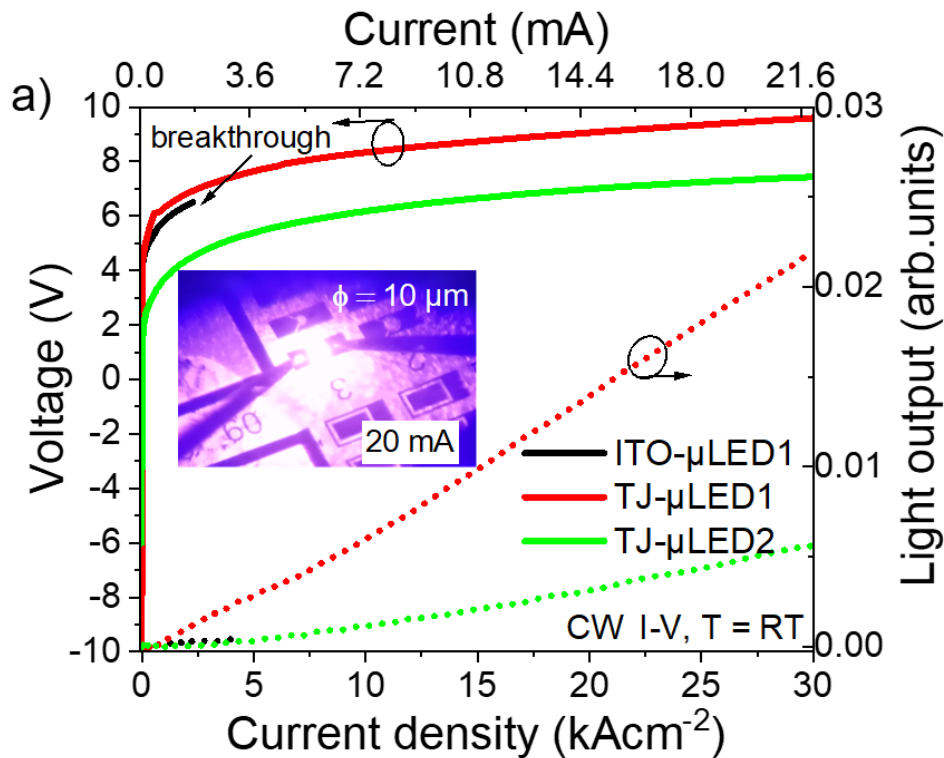
The current aperture methods designed for lithographic processing of intra-cavity contacts of GaN-based VCSELs (discussed in section 4.2) were tested first for conventional ITO- μ LEDs and for TJ- μ LEDs with different doping concentrations in the tunnel junction layers (Table 5.3). The current injection in these micro-LEDs (aperture sizes between 2 and 10 μ m) reached several kA/cm² which represents an important step towards VCSEL operation. The first sample series consisted of different types labelled ITO- μ LED1, TJ- μ LED1 and TJ- μ LED2 and are characterized by oxide-defined aperture structures (Fig. 5.7). The two TJ- μ LEDs were grown using the same parameters as for the reference ITO- μ LED1, except that a GaN:Ge cap layer was added on top. In the case of TJ- μ LED1, the GaN:Ge was overgrown on top of an oxygen plasma treated GaN:Mg surface of a std-LED while for TJ- μ LED2 the additional GaN:Ge layer was directly grown on top of the GaN:Mg layer without any growth interruption. For the TJ- μ LED2 current injection occurred only through the sidewalls of the etched GaN:Ge layer. CpMg-flows of 10 sccm in the main p-GaN layers and 400 sccm in the top p-GaN contact layers were used for this first sample series.

Typical I-V curves of ITO-LED1, TJ-LED1, and TJ-LED2 with 10 μ m feature size of circular current injection areas are presented in Fig. 5.7a, along with the different current aperture diagrams shown in Fig. 5.7b. As an ITO layer is n-type ($n \sim 10^{20}$ cm⁻³), it can be regarded as a TJ contact to the p-GaN layer, i.e. n⁺⁺/p⁺⁺ tunnel junction contact, (Fig. 5.7b1) and it may form an ohmic n-contact to the sidewalls of the GaN:Ge layer of the GaN:Ge/GaN:Mg tunnel junction, Fig. 5.7b3. The ITO- μ LED1 and TJ- μ LED1 have comparable I-V characteristic at

Table 5.3 Summary of growth parameters for GaN layers in the micro-LEDs for test of the various current aperture approaches as described in section 4.2.

	Sample name	CpMg-flow (sccm)	Cap layer (sccm)	With EBL	Aperture design (Also see Fig. 5.7b)
Series 1	ITO- μ LED1	10+400	none	No	oxide aperture (b1)
	TJ- μ LED1	10+400	IBGe, 0.33	No	SAG-approach for TJ (b2)
	TJ- μ LED2	10+400	IBGe, 0.33	No	passivation approach for TJ (b3) w. metal-sidewall contact
Series 2	ITO- μ LED2	20+400	none	Yes	oxide aperture (b1)
	TJ- μ LED3	10+40	IBGe, 0.33	Yes	passivation approach for TJ (b3) /with ITO-sidewall contact
	TJ- μ LED4	20+20	GeH ₄ , 0.1	Yes	passivation approach for TJ (b3) /with ITO-sidewall contact
	TJ- μ LED5	20+80	GeH ₄ , 0.1 SiH ₄ , 1	Yes	passivation approach for TJ (b3) /with ITO-sidewall contact
	TJ- μ LED6	20+400	GeH ₄ , 0.1	Yes	passivation approach for TJ (b3) /with ITO-sidewall contact

1 kAcm⁻² of 5.8 V and 6.3 V, respectively, but the latter has much more light output. Also, with TJ- μ LED2 current injection and reasonable light emission is achieved demonstrating the general feasibility of this approach. While TJ- μ LED2 has the lowest operation voltage of 3.8 V, this reduction is likely due to a leakage in the metal contacts and aperture sidewall. The current leakage and absorption losses at the edges of the apertures (Fig. 5.7b3) may have reduced the light output of TJ- μ LED2 as compared to TJ- μ LED1. These leakage and light absorption losses were reduced in the next sample series by optimized sidewall treatments and by replacing the metals with the ITO to form the contact to the etched GaN:Ge sidewalls. The ITO- μ LED1 is unstable and, even though its light output is lower than that of TJ- μ LED1, devices started to degrade at current densities above 3 kAcm⁻². In contrast, TJ- μ LEDs 1 and 2 could be driven at very high current densities and operated under continuous wave (CW) conditions up to 30 kAcm⁻² without failure. The inset of Fig. 5.7a shows a homogeneous emission of TJ- μ LED1 at this current density of 30 kAcm⁻² through an aperture diameter of 10 μ m. In addition, the capability of these μ LEDs to operate at very high current densities with very high light output power densities render them useful for novel LED applications in



b) Aperture designs

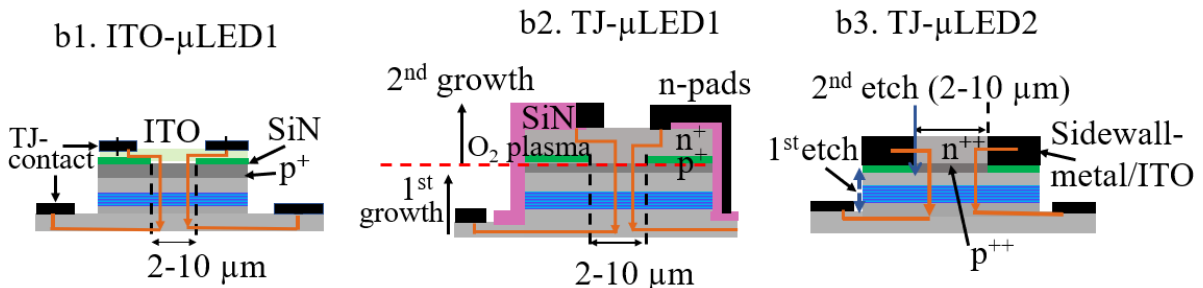


Fig. 5.7 Typical I-V characteristics of $10\ \mu\text{m}$ -LEDs (a) processed in 3 different current aperture methods (b). The inset is photograph image of the homogeneous emission of the $10\ \mu\text{m}$ TJ-LED1.

particular for μLED displays [38]. An example of an alphabetical display with 3 letters on a $1\ \text{mm}^2$ mesa of GaN TJ-LED1 was tested at a current of 40 mA (Fig. 5.8). In this diode, the area of the 3 letters A, B, and C was protected by positive photoresist during O_2 plasma passivation process (see parameters of the treatment in the Appendix A). After removal of the photoresist, the sample was overgrown with GaN:Ge. The passivation allows current only to pass the GaN:Ge/GaN:Mg interface in the unpassivated area of the letters.

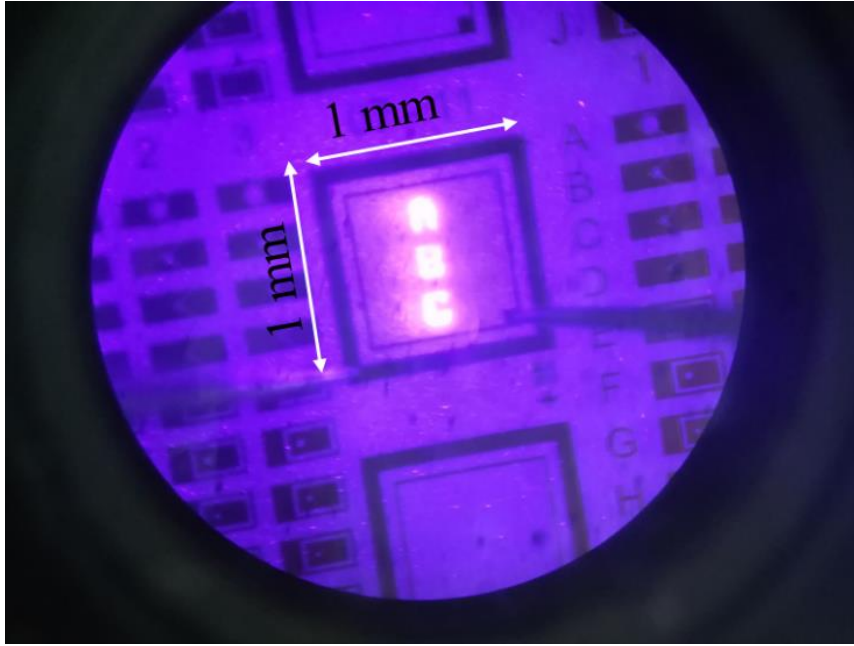


Fig. 5.8 A photograph image of an alphabetical display out of a 1 mm² mesa for TJ- μ LED1.

Using the same approaches for the current apertures, the second micro-LEDs series was studied for the impact of doping on the I-V and emission characteristics (cf. Table 5.3). Fig. 5.9 shows the L-I-V characteristics of TJ- μ LEDs 3-6 and ITO- μ LEDs 1 and 2. The doping in the buried p-GaN layer and at the interface is relatively low for TJ- μ LED3, whereas the p-doping was doubled (20 sccm CpMg-flow) for the buried p-GaN layer in TJ- μ LED4 but without high Mg-doping at the TJ interface. For TJ- μ LEDs 5 and 6, the doping in the buried p-GaN layer is similar to TJ- μ LED4 but increased by a factor of 4 at the TJ interface layer for TJ- μ LED5 and 20 times (400 sccm) for TJ- μ LED6, respectively. The latter doping is repeated for the p-GaN contact layer in ITO- μ LED2. TJ- μ LED5 features another 260 nm thick GaN:Si (SiH₄, [n] $\sim 3 \times 10^{18}$ cm⁻²) layer which was grown on top of the GaN:Ge tunnel junction layer in order to reduce the width of the V-pits on the surface which is crucial for the upper mirror deposition. However, this additional layer needs further optimization as it has implications on the tunnel junction properties and therefore the current injection.

In this series, TJ- μ LED4 (highest Mg-doping for the buried p-GaN, but moderate Mg-doping concentrations in the contact layer yields the best I-V characteristic and highest light output compared with TJ- μ LED5 and TJ- μ LED6 (both with increased Mg-doping in the p-GaN contact layers). TJ- μ LED4 has an I-V curve comparable to the I-V curves of reference ITO- μ LED1 and ITO- μ LED2 with slightly higher light output. The turn-on voltage for the best TJ-

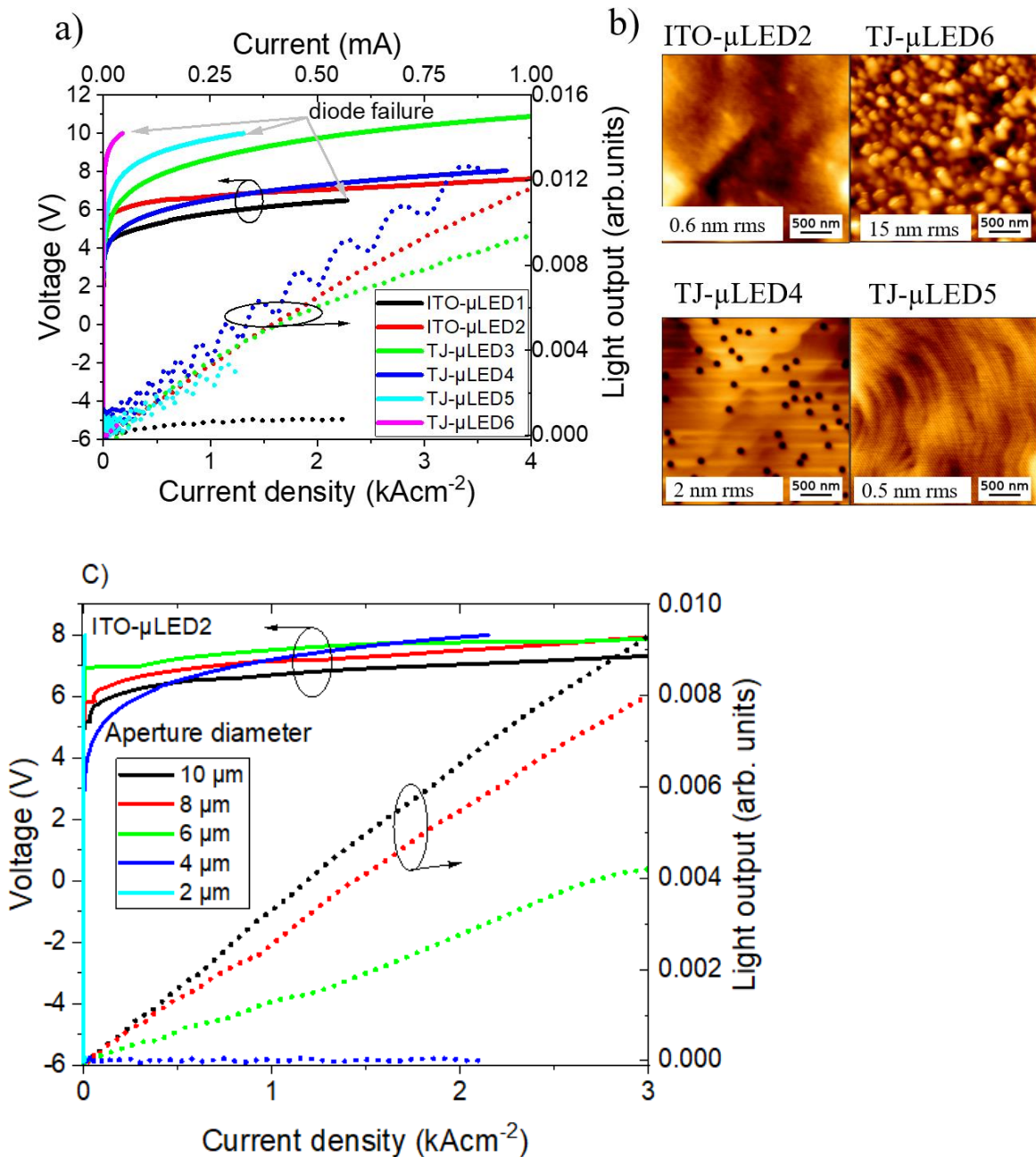


Fig. 5.9 The I-V characteristics of $10\ \mu\text{m}$ ITO- μLED devices and TJ- μLED devices with various Mg-doping schemes employing 3 different current aperture methods (a), AFM images ($3\times 3\ \mu\text{m}^2$ scans) of respective μLED surfaces (b), and comparison of I-V curves of the ITO- $\mu\text{LED}2$ devices for apertures varying from 2 to $10\ \mu\text{m}$ (c).

LED4 is 4.5 V, ~ 1 V lower than the best ITO- $\mu\text{LED}2$. However, an increased series resistance is found for TJ- $\mu\text{LED}4$ leading to higher operating voltage of 7.7 V at $4\ \text{kAcm}^{-2}$. This higher series resistance is likely due to the lateral contact formation between GaN:Ge and ITO (Fig. 5.7b3).

Unlike the ITO- μ LEDs, an additional excessive Mg-doping concentration at the contact layer in combination with an increased Mg-doped in the buried p-GaN for TJ- μ LED6 led to increased defect densities as can be seen in AFM pictures (Fig. 5.9b). These increased defect densities could be avoided by adjusting to the CpMg flow at the p⁺⁺ layer and adding an additional GaN:Si layer on the top of GaN:Mg/GaN:Ge tunnel junction layers (TJ- μ LED5). At low current densities, the light intensity measurements show variations (oscillations) for TJ- μ LED4-6 (all with increased Mg-doping in the buried p-GaN layer, Table 5.3) which is connected with a spotty emission around the aperture edges. A possible cause is current crowding at the aperture sidewall and current leakage paths in case of the lateral current injection scheme.

It is likely that the intensity variations are influenced by the type of doping scheme. For comparison, TJ- μ LED3 devices with Mg-doping of 10+40 sccm showed a stable output. Those TJ- μ LED devices with higher CpMg flow in the buried p-GaN layer, albeit being much brighter, were also very fragile as they easily showed breakthrough behavior at higher current flows. This may have been caused by strong thermal heating or a short-circuit at higher electric fields correlated with the observed filamentation of the current paths. Poor contact schemes on the aperture sidewalls are also a possible cause.

The combination of high p-doping in the buried p-GaN layer and high p-doping at the buried p-GaN contact layer resulted in lower quality of the TJ- μ LEDs when an oxygen plasma treated p-GaN surface was overgrown with GaN:Ge. These devices also showed instable operation. To explain this, one could argue that the plasma treatment reduced the effective p-doping in the contact layer or that the oxide layer introduced a small charge capacitor (e.g., GaO) in between the p-GaN and the overgrown layer. Furthermore, the plasma induced passivation layer might have been too thin allowing for leakage from the overgrown GaN:Ge to the p⁺-GaN layer.

5.2 Half-cavity VCSEL structures

5.2.1 Tuning of cavity resonance

Fabrication of half-cavity VCSEL structures started with a 45-fold AlInN/GaN DBR epitaxially grown on sapphire substrates. Within the DBR, the GaN layers were grown at a temperature of 1100 °C and 200 mbar reactor pressure using H₂ carrier gas while AlInN layers were grown at a temperature of 780 °C and 70 mbar pressure using N₂ carrier gas. These growth conditions for AlInN ensured lattice-matched growth to GaN with an indium content of around 18 %. The nominal layer thicknesses of the AlInN and GaN quarter-wavelength layers were 44 nm and 40

nm, respectively, to yield a stopband position at around 415 nm and a theoretical stopband reflectivity of 99.9 %.

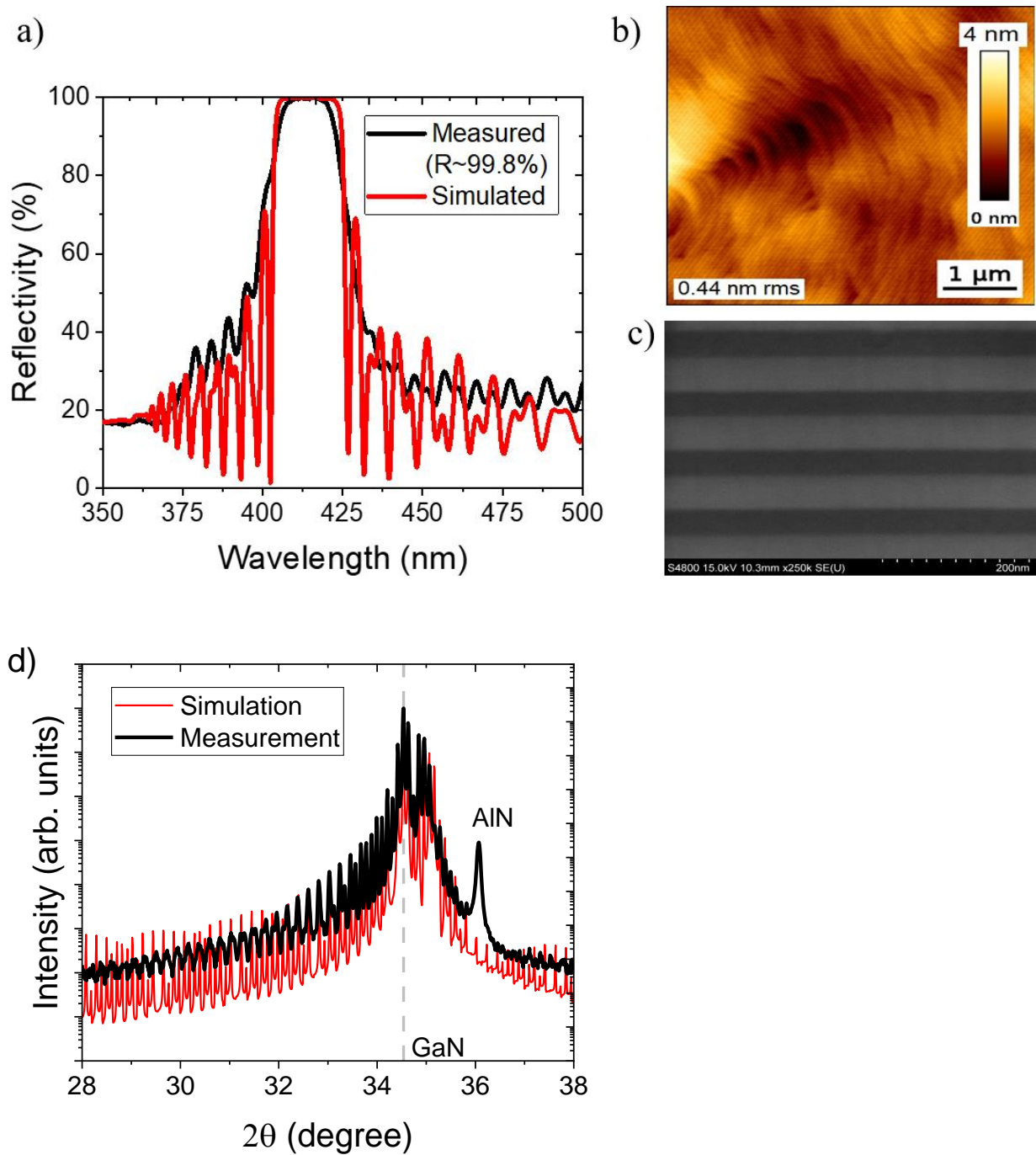


Fig. 5.10 Properties of a 45xAlInN/GaN DBR. a) Measured and simulated reflectance b) AFM images c) SEM cross-section images d) HRXRD $\theta/2\theta$ -scans around GaN (0002) reflection and respective simulation.

Fig. 5.10 shows the spectral properties of such AlInN/GaN DBR which served as bottom mirror in the VCSEL structures. The maximum measured reflectivity amounts to 99.8 % with a stopband FWHM of about 34 nm. High optical and structural quality of the DBRs confirmed by the simulated spectrum (Fig. 5.10a). The reduced Fabry-Pérot-oscillations at both sides of the stopband is caused by a layer thickness gradient across the wafer in combination with the averaging effect of a relatively large measurement spot size ($\sim 2 \times 8 \text{ mm}^2$). Both surface morphology and interface quality were qualitatively assessed by AFM and SEM measurements. A smooth surface with a root mean square (rms) roughness of $\sim 0.44 \text{ nm}$ for a $5 \times 5 \text{ }\mu\text{m}^2$ size scan was revealed by the AFM image (Fig. 5.10b). Fig. 5.10c depicts a cross-section SEM image of the DBR showing the periodic structure with the AlInN layers (bright contrast) and the GaN layers (dark contrast). Constant layer thicknesses and smooth interfaces, prove a good quality of the AlInN/GaN DBR.

Also, constant compositional quality, constant periodicity, and smooth interfaces of bottom DBR was confirmed by a high-resolution X-ray diffraction (HRXRD) measurement as well (Fig. 5.10d). Superlattice fringes were observed across a large angular range. According to respective simulation of the diffraction pattern, an indium content of 18 % in AlInN and a layer thickness of 46 nm/41 nm for AlInN and GaN, respectively, was determined.

5.2.2 Optimization of the p-doped region in half-cavity structures

To assess the impact of p-doping on the electrical and optical properties of GaN-based VCSELs, the I-V characteristics of standard LED structures and half-cavity were compared (Fig. 5.11). These devices had a circular aperture of $30 \text{ }\mu\text{m}$. Thereby, two different doping schemes for the p^{++} -contact layer were tested. For the basic diode structures refer to section 3.1 (Fig. 3.2). For LED1 and VCSEL1 the CpMg flow as compared to the bulk GaN:Mg growth was increased by a factor of 4 during growth of the p^{++} -contact layer while for LED2 and VCSEL2 the CpMg-flow was increased by a factor of 40. The stopband of VCSEL1 had a maximum reflectivity of about 99 % at a wavelength of around 415 nm. With the lower doping for the p^{++} -layer, LED1 and VCSEL1 devices operated with comparably high turn-on voltages of 5 and 6 V, respectively, and with a similar operating voltage of 7.5 V at a current density of 1 kAcm^{-2} . For higher forward current densities, the high series resistance caused breakthrough of the diodes. For the higher doping of the p^{++} -contact layer, the turn-on voltage was reduced by 2 V. Thus, turn-on voltages of 3 V and 4V were observed for LED2 and VCSEL2 devices, respectively, while the voltages measured at 1 kAcm^{-2} were 3.7 V for LED2 devices and 6 V for VCSEL2

devices. VCSEL2 devices showed a 10 times higher light output as compared to VCSEL1 devices.

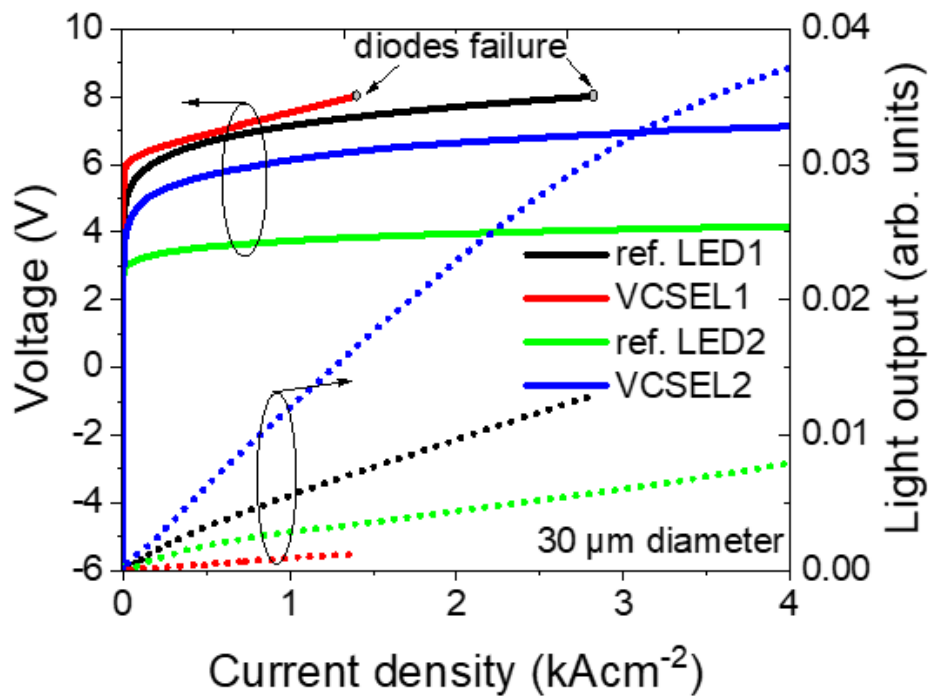


Fig. 5.11 I-V characteristics for standard LEDs and half-cavity VCSEL diodes with different $CpMg$ -flow during growth of the p^{++} -region. LED1 and VCSEL1 had 4x increased flow, LED2 and VCSEL2 had a 40x increased flow as compared to the bulk GaN:Mg growth.

5.2.3 Growth related issues of cavity properties

In the small research-type MOVPE reactor, layer structures like highly reflective AlInN/GaN DBR usually exhibit a radial thickness gradient across the wafer. This is due to temperature gradients across the wafer (caused by wafer curvature) and due the different depletion of the reacting species in the gas phase. This is a great challenge for the growth design of DBRs, since already a small lateral thickness gradient with thickness changes of $\pm 2\%$ would lead to a stopband wavelength shift of $\pm 8\text{ nm}$ [14]. It therefore was unavoidable to observe spectral matching of the specified cavity resonance with the MQW spectral properties only within limited radial distance from the center of the wafer.

Fig. 5.12 shows a schematic drawing of two VCSEL structures, from which one (VCSEL diode 3) is characterized by a non-intentionally detuned cavity, while the other (VCSEL diode 4) was

corrected to match MQW emission and cavity resonance. Experimentally, VCSEL diode 3 had a stopband red-shifted by 26 nm with respect to the MQW emission wavelength (Fig. 5.13a). The photoluminescence (PL) peak was at 407 nm wavelength while the maximum reflectivity of 98% was measured at 433 nm. Unfortunately, a particle issue (Fig. 5.13b, inset) within the reactor during growth negatively impacts the reflectivity measurement. Due to the large measurement spot of the photospectrometer, the measured stopband reflectivity was reduced 92 % (Fig. 5.13b, inset) and the sideband oscillations were smeared out.

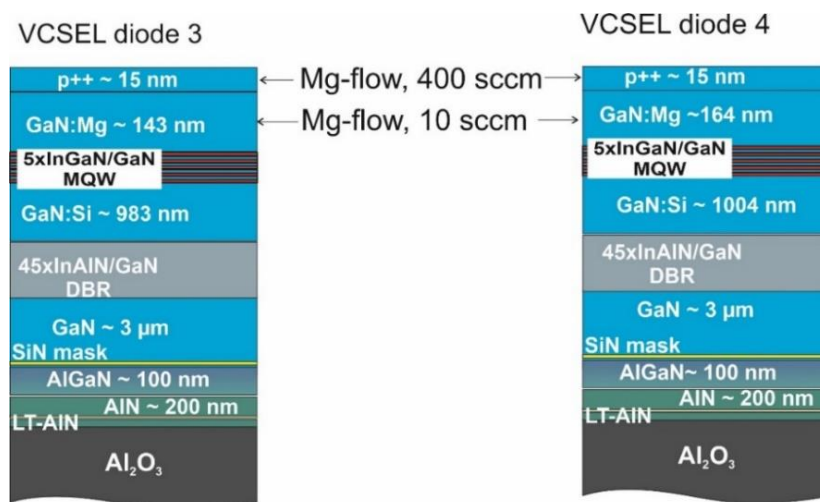


Fig. 5.12 A schematic layer structures for conventional VCSEL diodes 3 and 4.

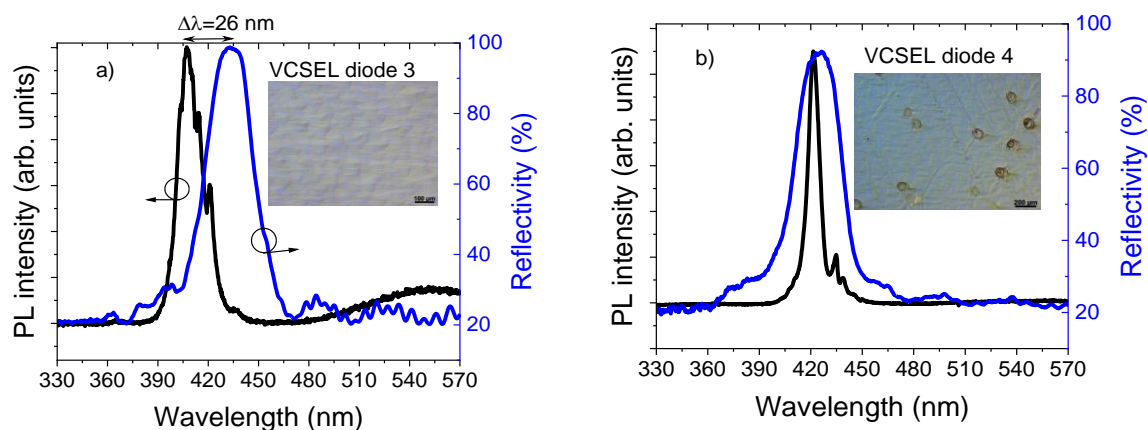


Fig. 5.13 Reflectivity and PL emission spectra for a) detuned and b) resonant VCSEL diode structures. Insets are Nomarski microscopy images of the wafer surface after growth revealing a large number of particles in b).

The FWHM of the emission peak for VCSEL diode 3 was 38 nm while it was reduced to 33 nm for VCSEL diode 4. This narrowing of the emission spectrum is the effect of the matched

cavity resonance. Fig. 5.14 shows the I-V characteristics of the half-cavity VCSEL diodes 3 and 4 with oxidized Ni/Au metal contacts covering the full diode area. The I-V curves for VCSEL diode 3 showed lower operation voltage than VCSEL diode 4 devices (Fig. 5.14a). The increased voltages for diode 4 might have been caused by a disturbed p-type doping due to the high particle defect density on the surface (see Fig. 5.13b, inset). The maximum current densities in the I-V curves were limited by the maximum current of the setup (100 mA). While the light output from mesas with diameters of 100 μm were comparable for both diode types, for smaller VCSEL diode 4 devices with diameter of 50 μm or 30 μm were significantly brighter (despite the high particle density) than VCSEL diode 3 devices (Fig. 5.14b), which might be attributed to the better resonance matching of the microcavity.

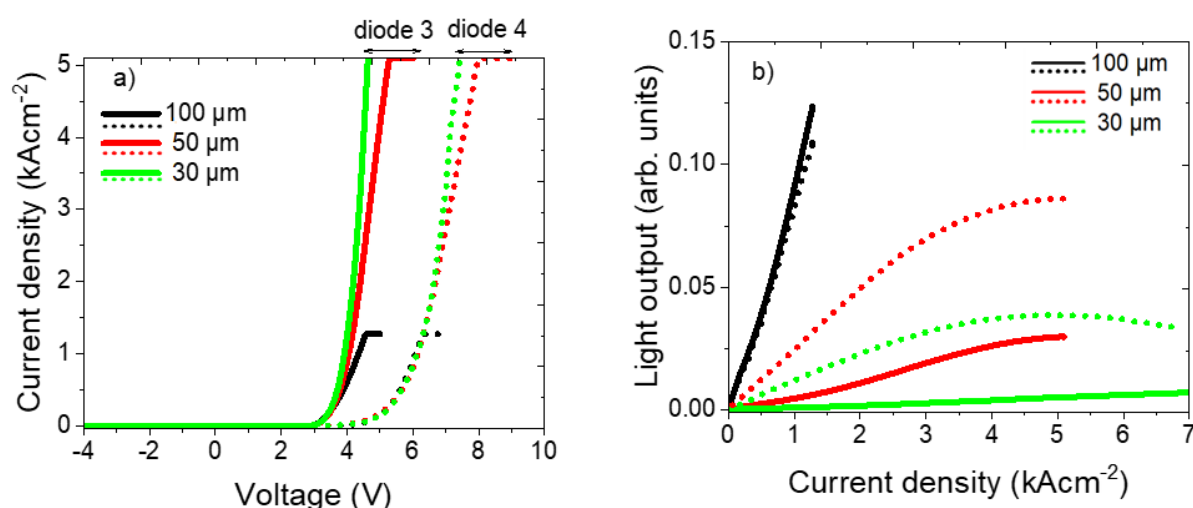


Fig. 5.14 a) I-V characteristics for half-cavity VCSEL diode 3 type with detuned cavity and for VCSEL diode 4 type with resonant cavity b) light output for VCSEL diode 3 type (solid lines) and for VCSEL diode 4 type (dotted).

5.2.4 ITO-VCSELs vs. TJ-VCSELs

In this section, results from half-cavity VCSEL structures with an ITO layer or with GaN:Ge tunnel junctions to laterally distributed current injection are presented. The growth conditions were tuned to ensure a good structural quality, resonance of stopband and emission for all VCSELs. The growth of the active region was first tested by growing conventional ITO-LED and GaN TJ-LEDs 1 and 2 as reference diodes. Subsequently, a 7λ -cavity ITO-VCSEL reference and TJ-GaN VCSEL1-3 were grown with similar p-doping schemes. Table 5.4 shows an overview of the sample structures used in this series. While the CpMg-flow in the buried

bulk p-GaN layer was 20 sccm for all samples, the CpMg-flow for the p⁺⁺-contact layer was 400 sccm for ITO-LED, ITO-VCSEL, TJ-LED2 and TJ-VCSEL3. TJ-LED1 had no p⁺⁺-layer while for TJ-VCSEL2, the p⁺⁺-layer was doped with a moderate CpMg-flow of 80 sccm. TJ-VCSEL2 features a 260 nm thick GaN:Si cap layer ([n]~3x10¹⁸ cm⁻³) grown on top of the GaN:Ge layer to smoothen the surface. A GeH₄ flow of 0.1 sccm ([n]~ 1x10²⁰ cm⁻³) was used for GaN:Ge layers in TJ-diodes. All samples of this series employed a 20 nm thick AlGaIn:Mg (CpMg-flux of 200 sccm) electron blocking layer (EBL) positioned at 17 nm above the MQW to block electron-overflow into the p-region. All VCSEL cavities had a peak reflectivity at about 415 nm wavelength which was in resonance to the emission of the InGaIn QWs at least in some parts of the wafer.

Table 5.4 Overview of half-cavity VCSEL structures with either ITO layers or TJ structures for current distribution.

Sample name	Mg-flow in buried GaN	Mg-flow in upper contact layer (p ⁺⁺)	Doping flow in TJ-layer (n ⁺⁺) / cap layer
ITO-LED	20 sccm	400 sccm	none
ITO-VCSEL	20 sccm	400 sccm	none
TJ-LED1	20 sccm	20 sccm	GeH ₄ , 0.1 sccm
TJ-LED2	20 sccm	400 sccm	GeH ₄ , 0.1 sccm
TJ-VCSEL1	20 sccm	20 sccm	GeH ₄ , 0.1 sccm
TJ-VCSEL2	20 sccm	80 sccm	GeH ₄ , 0.1/ SiH ₄ , 1 sccm
TJ-VCSEL3	20 sccm	400 sccm	GeH ₄ , 0.1 sccm

Fig. 5.15 shows AFM images of the respective surfaces of structures. For TJ-LED2 and TJ-VCSEL3 with maximum CpMg-flow the subsequent grown GaN:Ge layer surfaces suffer strong roughening. In contrast to these TJ-diodes, a comparably doped ITO-VCSEL still shows a smooth surface. However, the surface morphology already appears different to typical GaN surfaces which are characterized by step-flow growth. It might be that first inversion domains were formed by the heavy Mg-doping and that those inversion domains were responsible for the significant roughening when the growth continued with GaN:Ge. The AFM images of the

other TJ-diode types show that these diodes also can have a smooth surface with comparable rms values to that of conventional diodes (TJ-LED1 and TJVSEL1,2).

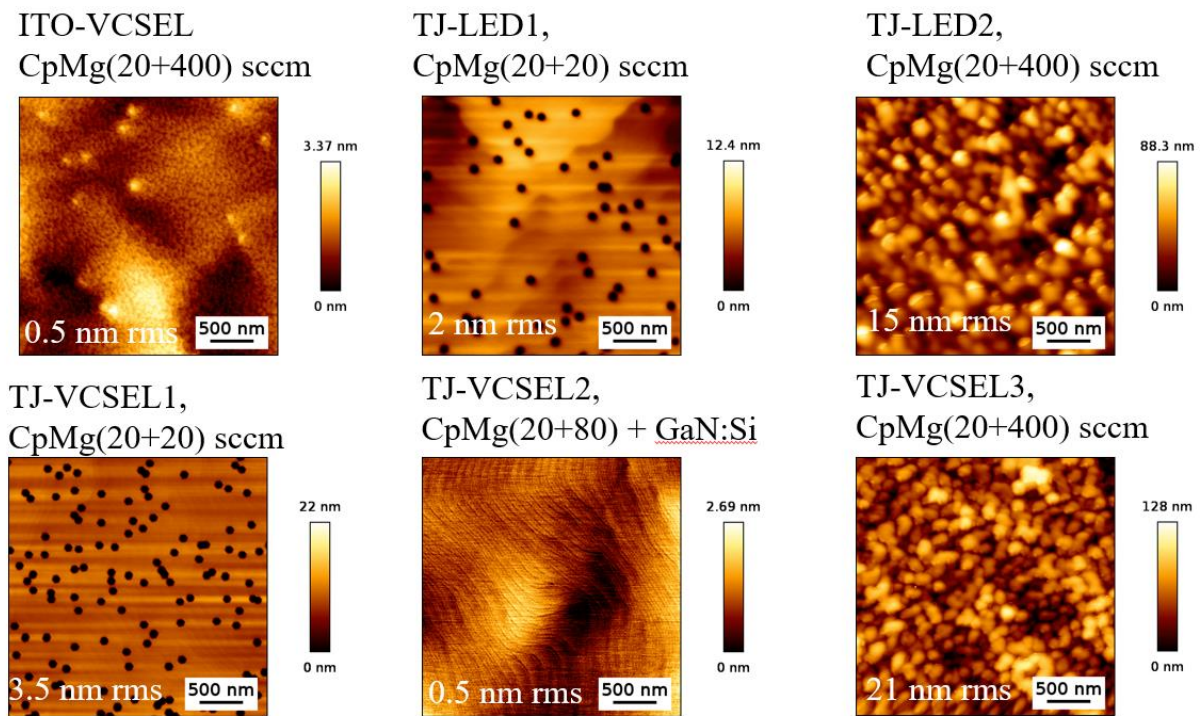


Fig. 5.15 AFM images, 3x3 μm² scans, of ITO-VCSEL, TJ-LED1,2, and TJ-VCSEL1,2,3 with varied high p-doping concentration at the interface layer.

The roughening for TJ-diodes with maximum CpMg-flow for the p⁺⁺-layer can be also observed by in-situ reflectivity measurements at 405 nm wavelength (Fig. 5.16). During growth of the TJ-VCSEL3 the reflectivity suddenly drops indicating a severe surface degradation whereas this drop is not present during the growth of TJ-VCSEL1. Accordingly, the surfaces were completely different with rather smooth morphology for TJ-VCSEL1 and a very rough morphology for TJ-VCSEL3. The surface of TJ-VCSEL1 also exhibits the V-pits which are typical for GaN:Ge grown under nitrogen atmosphere and at low temperature.

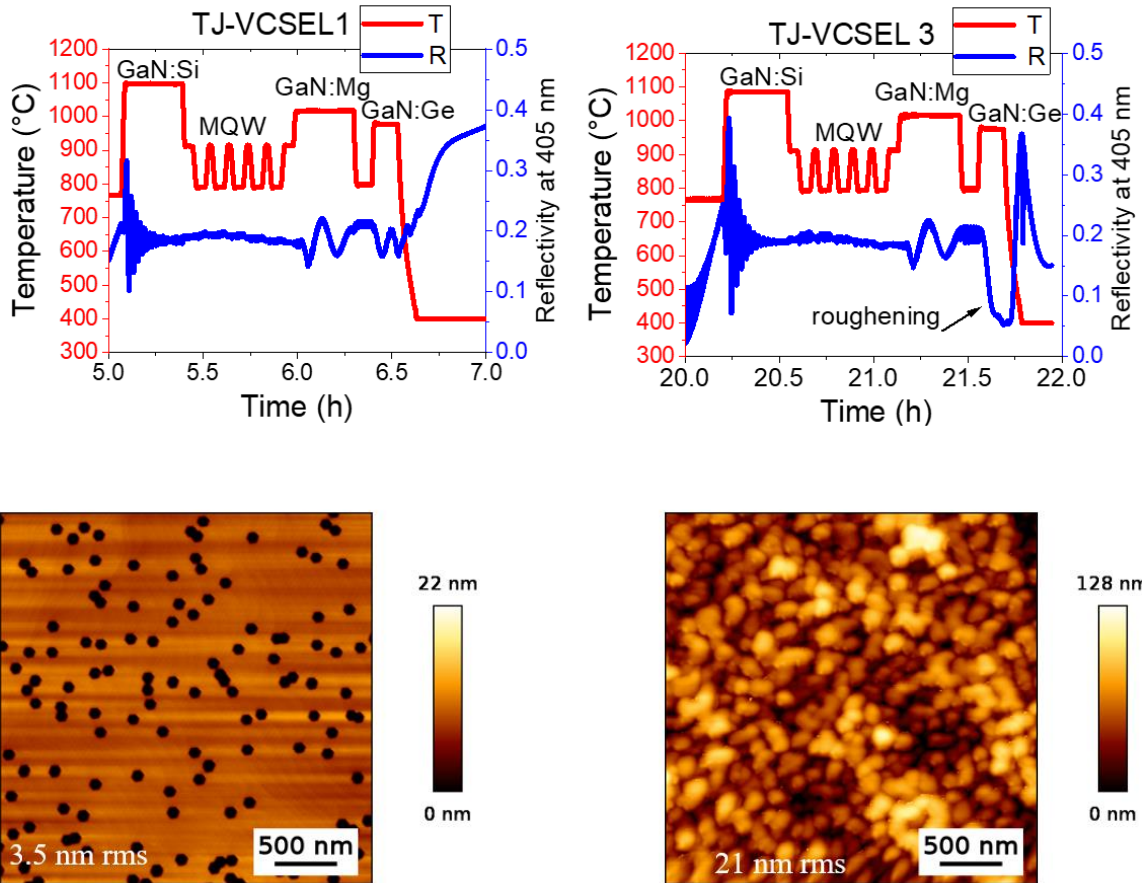


Fig. 5.16 In-situ reflectivity data of two different CpMg-flows of 20 sccm (left) and 400 sccm (right) during growth of the p-GaN interface layer in TJ-VCSELs structures. A significant drop in reflected intensity was observed in the subsequently grown GaN:Ge layer when a high CpMg-flow was chosen, indicating surface roughening, as confirmed by AFM (bottom row).

The HRXRD analysis of the conventional ITO-VCSEL diode showed that the structural quality of the DBR and the active region were comparable to the reference DBR structure (described above in 5.2.1) and to the InGaN/GaN MQW properties of reference LED structures (Fig. 5.17). Pronounced superlattice fringes originating from the periodic MQW and DBR structures were visible over a large angular range. This implies that the interface quality and periodicity of the DBR were similar in the VCSEL structures.

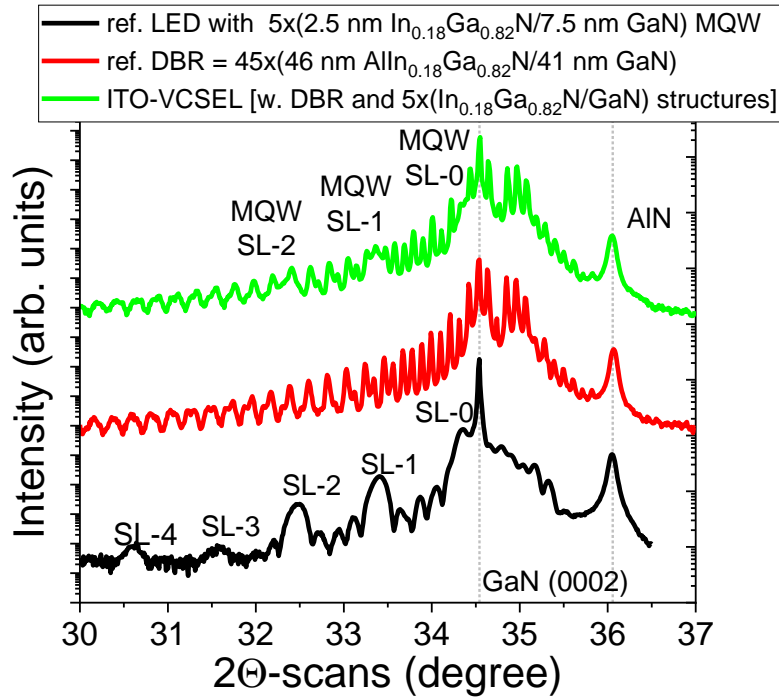


Fig. 5.17 HRXRD (0002) $\theta/2\theta$ -scans for conventional half-cavity ITO-VCSEL structures compared to 45xAlInN/GaN DBR and 5xInGaN/GaN LED reference structures.

Fig. 5.18 shows the PL (a) and reflectance (b) spectra of the conventional VCSEL reference diode (ITO-VCSEL). The reflectivity measurement at the center and towards the edge (spot center was set ~ 0.5 inch off center position) revealed a blue-shift of the stopband from 414 to 405 nm comparable with the PL peak shift of 9 nm from the wafer-center to the wafer-edge (Fig. 5.18a). Since no variation of the indium content in the QWs was detected from HRXRD measurements, the PL wavelength shift is caused by the shift of the cavity resonance. In proximity of the wafer-center no significant shift of the stopband or PL was observed due to the similar optical properties. The peak and integrated intensities as function of current injection for a 6 μm aperture diameter are presented in Fig. 5.19a. The intensity linearly increases as a function of the current, that increases roughly from 8 μA (10 Acm^{-2}) up to a maximum of 6.4 mA (22.5 kAcm^{-2}). At current densities above 22.5 kAcm^{-2} diodes were destroyed. The inset shows an electrically driven half-cavity ITO-VCSEL with 6 μm device at a current density of 22.5 kAcm^{-2} . The bright spots that are visible around the aperture are artifacts from the mesa facets. Fig. 5.19b shows EL measurements at different injection current densities. As can be seen, the EL emission peak in this device was measured at around 411 nm. The FWHM of the EL spectra of 6 μm aperture half-cavity ITO-VCSEL increased from 5 nm to 8 nm when current density was increased from 10 Acm^{-2} to 22.5 kAcm^{-2} , respectively.

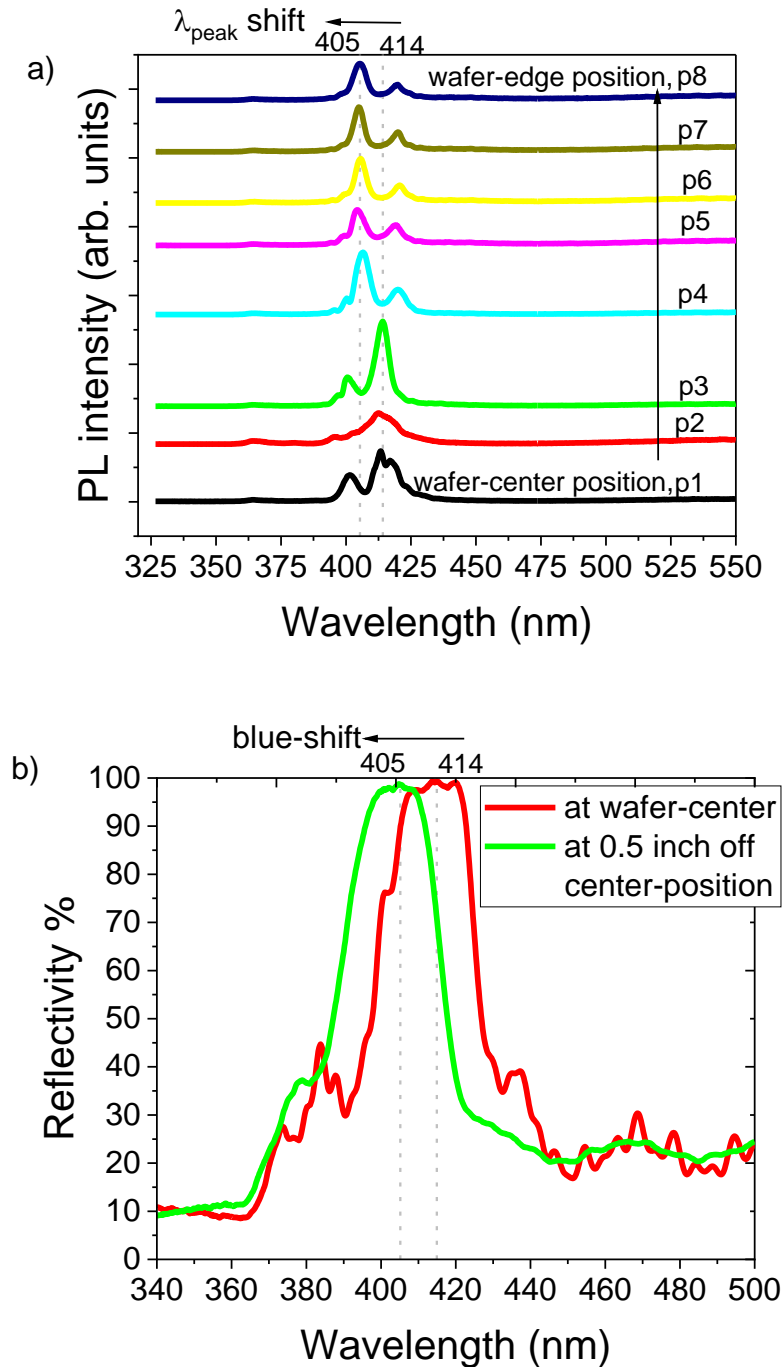


Fig. 5.18 a) PL and b) reflectivity mapping across a wafer of a conventional half-cavity ITO-VCSEL diode structure.

Fig. 5.20a shows the room temperature cw L-I-V characteristics of ITO-LED, ITO-VCSEL, TJ-LEDs 1 and 2, and TJ-VCSELs 1, 2, and 3 devices (as described in Table 5.4) with an aperture diameter of 10 μm . The devices were processed as schematically shown in Fig. 5.20b. For standard pn-diodes, SiN passivation was used to confine the current within the aperture diameter and ITO was deposited on top of the aperture as current spreading layer (Fig. 5.20b1).

In tunnel junction diodes, the first mesa-etch defined the basic device size and went down to the n-GaN below the active region. This step was followed by a second etching step that defines the aperture size. Here, the etching process went through the (n⁺⁺/p⁺⁺)-TJ ending in the bulk p-GaN layer. Afterwards, the surface of the p-GaN layer was passivated with a thin SiN layer (~15 nm). In the next step an ITO layer was deposited with thickness corresponding to the etching depth (~100 nm). The ITO layer formed a lateral contact to the “aperture mesa” sidewalls permitting current injection through the sidewalls of the etched n⁺⁺ GaN tunnel junction layer (Fig. 5.20b2).

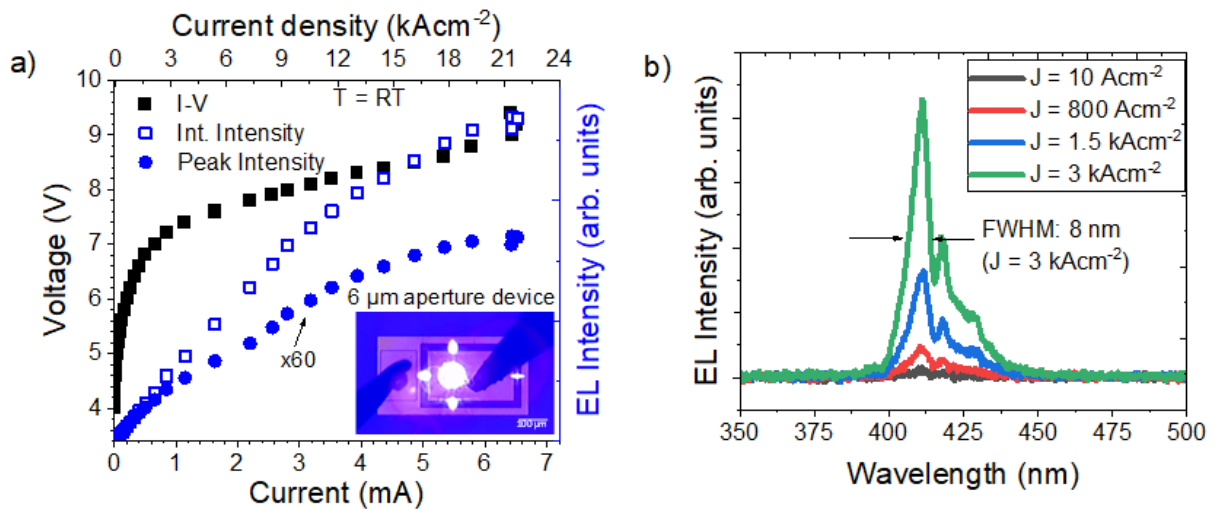


Fig. 5.19 a) Operating voltage and EL intensity as function of current-density for a 6 μm aperture device of half-cavity ITO-VCSEL. The inset shows spontaneous emission at a current density of 22.3 kAcm⁻². b) Typical EL emission spectra of a 6 μm device at various current densities from 10 Acm⁻² to 3 kAcm⁻².

For a current density of 100 Acm⁻², a 10 μm-aperture conv. ITO-VCSEL structure required a bias voltage of 4.3 V. This is 1 V lower than for the best TJ-VCSEL1 devices. However, the TJ-VCSEL1 devices had the highest optical power at 8 kAcm⁻² injection current with 40% more light output than ITO-VCSEL devices. At 8 kAcm⁻² the operating voltage was 8 V for ITO-VCSEL devices and 10 V for TJ-VCSEL1 devices. Unfortunately, only ITO-VCSEL diodes showed good I-V characteristics and light output for all aperture diameters (Fig. 5.21). For the other diode types, with increased p-doping at the interface layer, early breakthrough occurred at current densities of around 1 kAcm⁻². Comparing the morphological and structural properties of the tunnel junction diodes as determined by AFM and HRXRD better I-V characteristics and

higher light output correlated with better surface morphology and crystallinity. VCSEL devices with an additional GaN:Si layer (TJ-VCSEL2) on top of the TJ-region to cover the surface of V-pits also showed worse I-V characteristics and light output as well as early breakthrough, with lower emission and failed at low current density.

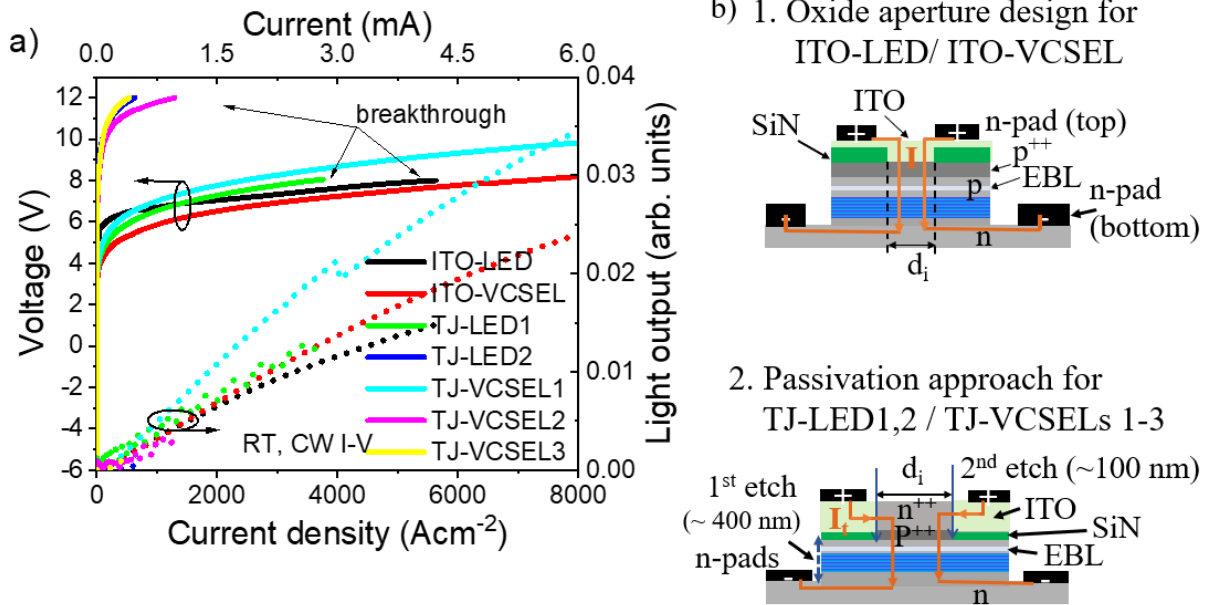


Fig. 5.20 a) I-V characteristics of ITO-VCSEL and TJ-VCSEL diodes compared with reference LEDs. b) Schematic view of the current aperture approaches for b1) standard ITO-diodes processing and b2) TJ-diodes processing.

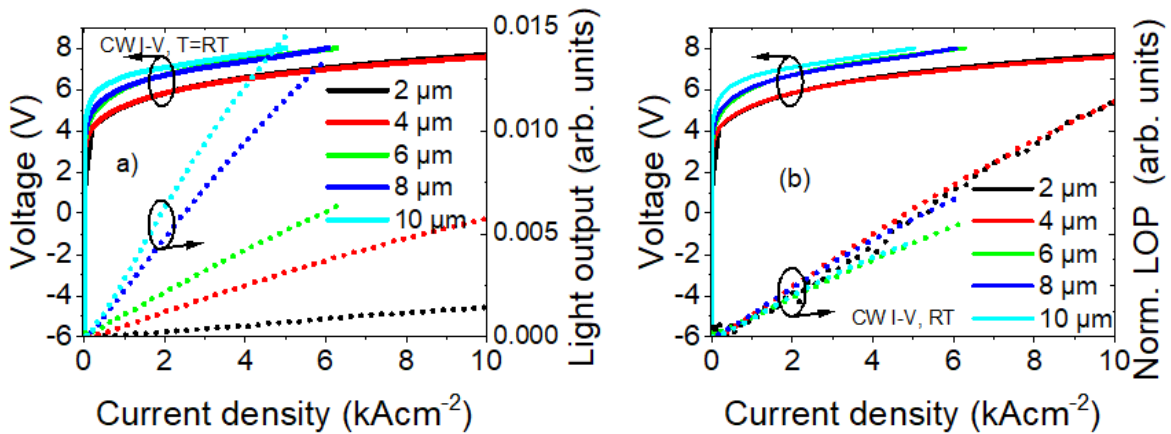


Fig. 5.21 The I-V characteristic of the conventional ITO-VCSEL reference diode with (a) relative light output for apertures between 2 and 10 μm and (b) Normalized light output to the area of the aperture.

5.3 Fabrication and characterization of full-cavity structures

5.3.1 Fabrication of the dielectric top DBR

For the fabrication of the upper DBR, $\text{SiO}_2/\text{HfO}_2$ $\lambda/4$ layers were investigated. Fig. 5.22 shows measured reflectivity and transmission of a 9-fold $\text{SiO}_2/\text{HfO}_2$ upper DBR deposited by reactive RF-sputtering on a double side polished (DSP) sapphire substrate. The DBR exhibited a maximum reflectivity of the stopband of 98 % at a wavelength of 415 nm with a FWHM of about 100 nm. The calculated losses within the DBR (by eq. 2.23) at the center of the stopband was 2 % which is high value considering the expected transparency of the materials at this wavelength. The high optical loss together with the averaging measuring spot set up and database values in the software caused a non-well fitted measured reflectivity by simulation (Fig. 5.22a). The simulation of transmission in Fig. 5.22b shows that at shorter wavelengths the losses even increased to higher values due to strong optical absorption in (at least) one of the DBR layers. At higher wavelengths pronounced oscillations are observed for measured reflectivity and transmission, showing a reduced absorption but with increased scattering losses.

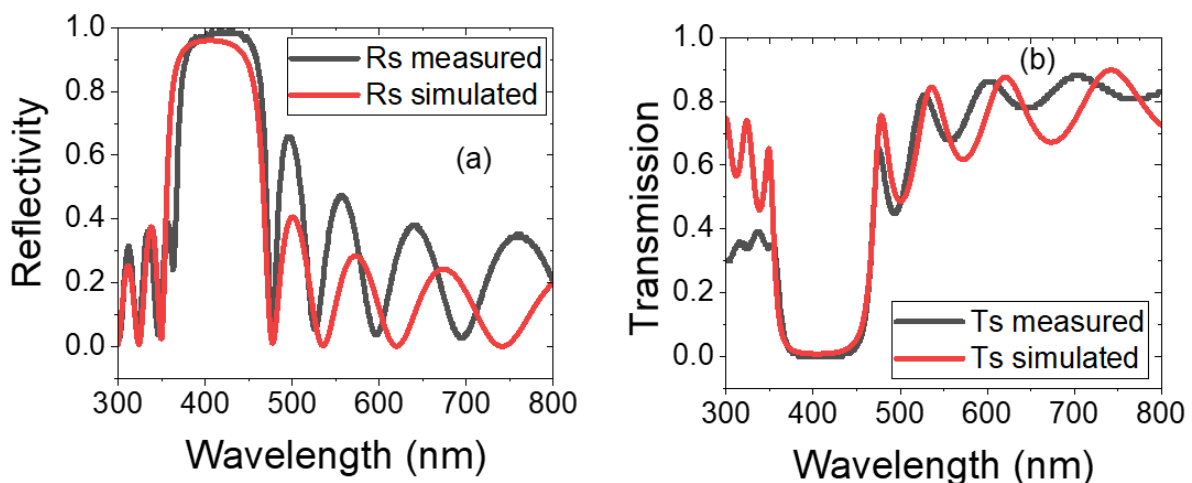


Fig. 5.22 a) Reflectivity (R_s) and b) transmission (T_s) of a 9-fold $\text{SiO}_2/\text{HfO}_2$ DBR test structure for a resonant wavelength of 415 nm.

In the SEM image shown in Fig. 5.23 the SiO_2 and HfO_2 layers exhibit rough interfaces. While the initial layers of the DBR were smooth the roughness increased with the number of deposited layers. Since the $\text{HfO}_2/\text{SiO}_2$ interface always represented the rougher interface the sputtered conditions of the HfO_2 needs to be improved. Additional X-ray reflectivity (XRR)

measurements also failed as no Kiessig-oscillations could be observed. $\text{SiO}_2/\text{Ta}_2\text{O}_5$ dielectric DBR structures provide another approach and were deposited by e-beam evaporation in past investigation. However, this deposition was even more challenging due to the difficulty for evaporating stoichiometric and smooth SiO_2 layers. The electron beam tends to burn holes in the SiO_2 pellets leading to very unstable deposition rates and non-uniform films.

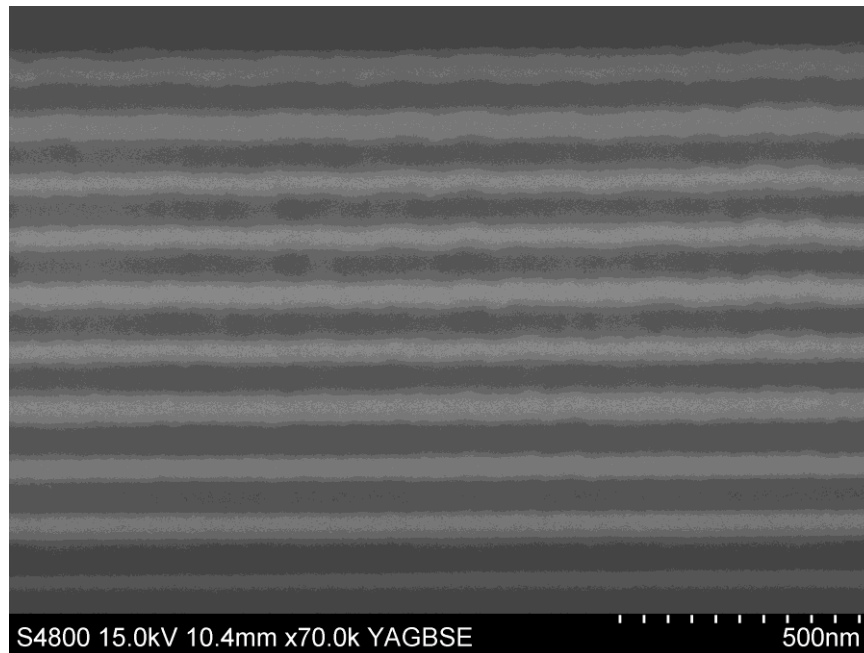


Fig. 5.23 Cross sectional SEM image of the 9-fold $\text{SiO}_2/\text{HfO}_2$ DBR test structure.

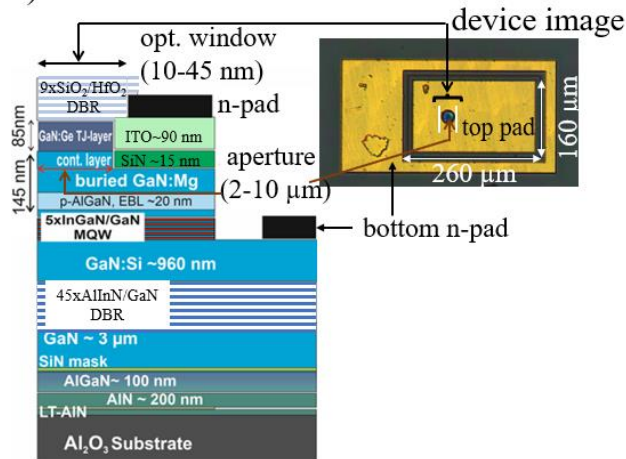
Despite the imperfections of the top dielectric DBR, a full-cavity VCSEL structure was processed using a lift-off process to define the cavity area. For lift-off process, a combination of an O_2 plasma asher and BOE pretreatment step was developed. Without this pretreatment the deposited mirror layers peeled off from the aperture. In a first step, the surface of the processed wafer including the metal contact was cleaned in a plasma asher with an O_2 plasma for 24 s at a power of 50 W to remove any residuals from the previous lithography. After the following lithography to define the deposition area for the top DBR, same O_2 plasma asher cleaning process was used again. Prior to the DBR deposition, BOE was applied for 25 s to remove residual oxides. The BOE process should be kept short enough to maintain the undercut of the photoresist openings and to avoid possible structural degradations of the ITO layer.

5.3.2 Optical and electrical characteristics

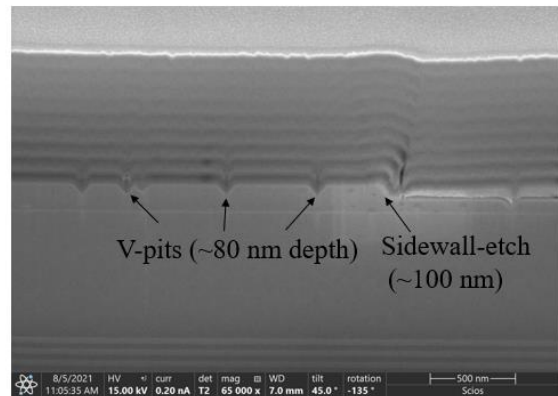
The sample structure of the 7λ -cavity TJ-VCSEL1 and a cross sectional STEM image of this VCSEL are shown in Fig. 5.24. In Fig. 5.24b several V-pits defects on the GaN surface are

visible. Fig. 5.24c shows electron microscope image of a TJ-VCSEL1 structure including the top DBR. The deposition of the SiN layer to passivate the etched surface was imperfect as there remained an elevation of the boundary to mesa region which leads to a disruption of the subsequent ITO layer and some of the DBR layers. The upper DBR also showed significant roughness.

a) TJ-VCSEL1 structure



b) SEM image of TJ-VCSEL1



c) STEM of a TJ-VCSEL1 (45° tilt)

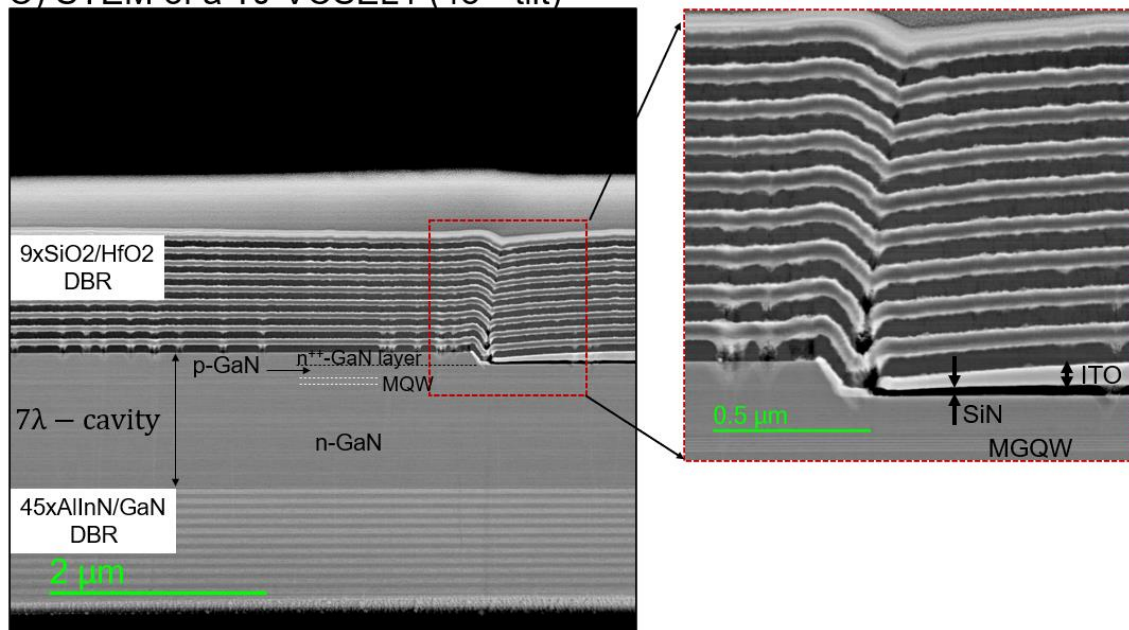


Fig. 5.24 a) Schematic of the layout of the 7λ -cavity TJ-VCSEL1 structures including a device photograph. b) Large view of the cavity structure. c) Closer inspection of the transition region from the cavity area to the contact region showing the disruption of the ITO layer due to an elevation in the first SiN layer.

Light-current-voltage-measurements for full-cavity ITO-VCSEL and TJ-VCSEL1 devices were performed at room temperature under continuous wave (cw) operation. Fig. 5.25 a and b show typical L-I-V characteristics for 8 μm and 6 μm aperture diameter devices, respectively. Both VCSEL structures have a comparable I-V curve but the light output of the TJ-VCSEL1 devices at $\sim 25 \text{ kAcm}^{-2}$, 8 μm aperture, (Fig. 5.25a) or at 10 kAcm^{-2} (6 μm aperture) (Fig. 5.25b) was twice that of ITO-VCSEL devices. The light intensity for TJ-VCSEL1 was even up to 10 times higher for devices with 10 μm aperture (see Fig. 5.25c and d). The higher brightness of TJ-VCSEL1 devices demonstrates the higher transparency of the GaN:Ge current spreading layer. One can see that the I-V curves and optical emission for the ITO-VCSEL devices were strongly dependent on the aperture diameter (Fig. 5.25c) while the I-V characteristics of TJ-VCSEL1 devices were more or less independent of the aperture diameter (Fig. 5.25d). The scattering of the ITO-VCSEL devices can be related to the ITO deposition process.

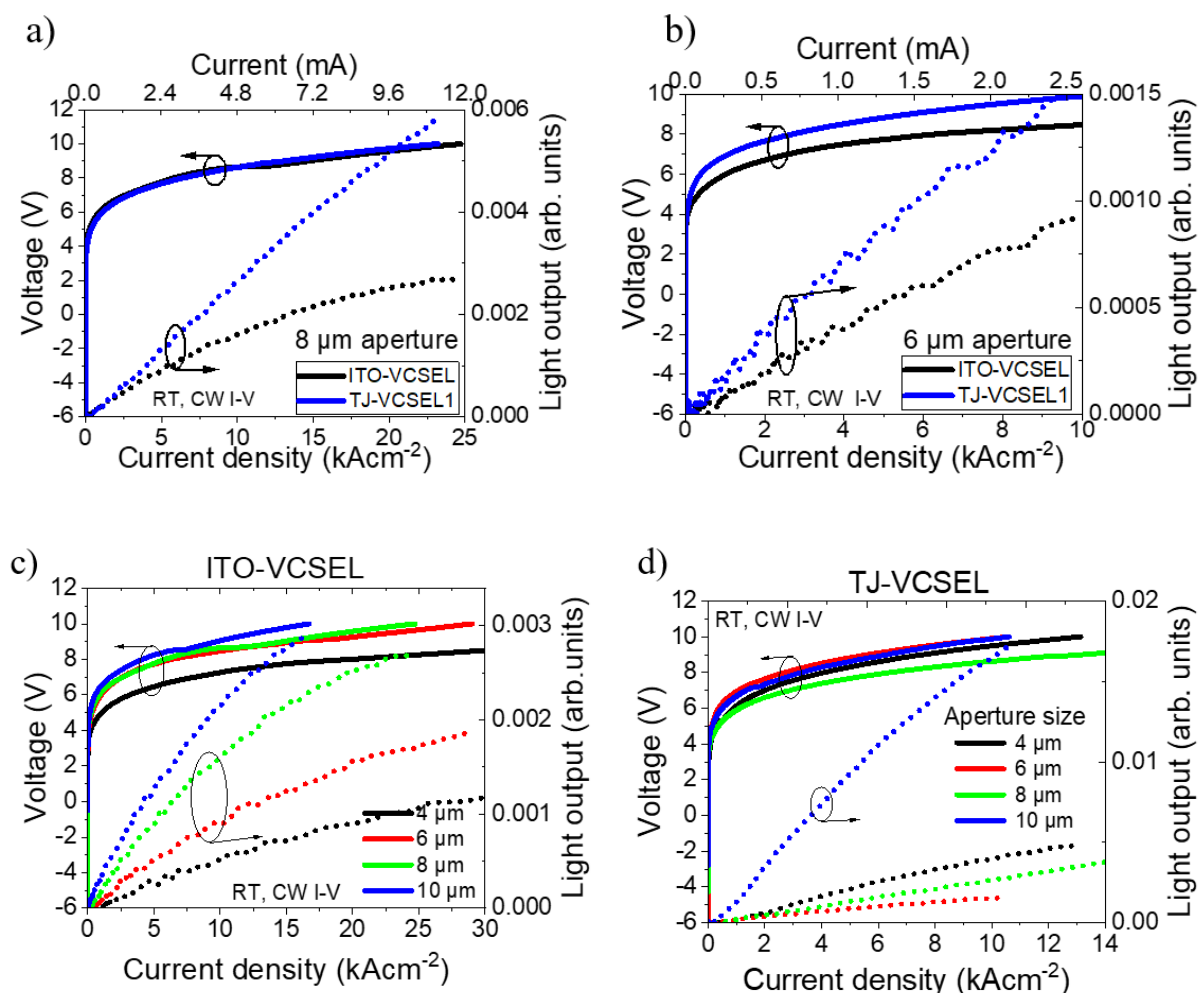


Fig. 5.25 Room temperature cw I-V characteristics and light output for a) 8 μm aperture and b) 6 μm aperture TJ- and ITO-VCSEL devices. Aperture diameter dependence of the light output of ITO-VCSEL (c) and TJ-VCSEL1 (d) devices.

Pulsed I-V measurements were conducted to extend the limit of the applicable current density and to possibly achieve lasing conditions (Fig. 5.26). Using 1 % duty cycle, diodes operated at current density up to 30 and 65 kAcm⁻² depending on aperture size (2-10 μm). Similar measurements on TJ-VCSEL1 devices (not shown) failed already at current densities below the cw maximum value of 14 kAcm⁻². It might be possible that the oxide passivation layers of these devices do not withstand the spikes in the electric field amplitudes that are present under the pulsed operating conditions.

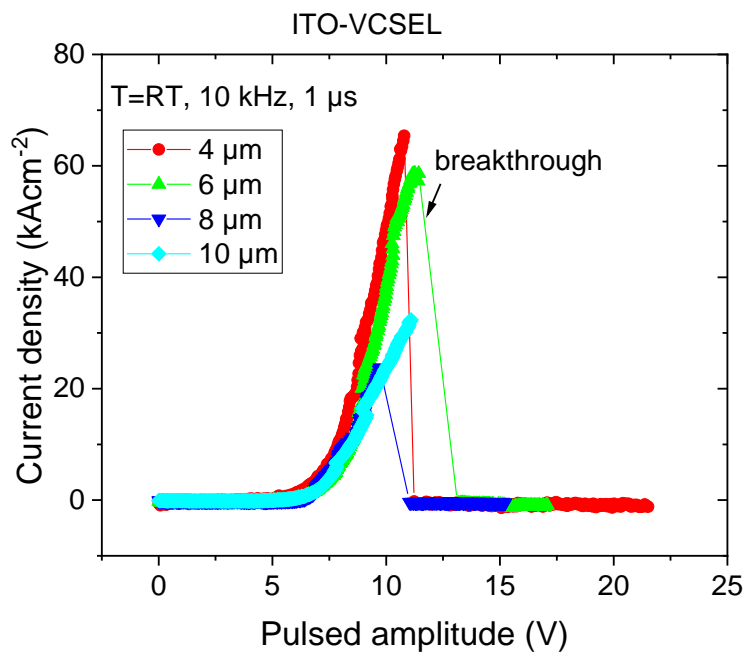


Fig. 5.26 Pulsed I-V measurements, 1 % duty cycle, for ITO-VCSEL devices.

Under pulsed operation the ITO-VCSEL devices withstand current densities up to 60 kAcm⁻². The onset of lasing could not be deduced from the L-I curve as there is no transition to a steeper L-I characteristic. At high current densities, the slope of the light output even decreased (Fig. 5.25c). For some of the TJ-VCSEL1 devices (see Fig. 5.27), the light output showed a transition at current density of 0.5 kAcm⁻² where the light output shows a steeper light output, which might be associated to the onset of the superluminescence.

A superluminescent diode (SLD) is produced when a laser gain medium is in its population inversion state, however the feedback is not sufficiently to switch to laser operation, resulting in much larger spectral emission width [77-79]. It is not easy to distinguish laser operation from the superluminescence regime taking only L-I measurement. Therefore, additional measurements

on the spectral linewidth above threshold current were conducted (Fig. 5.28) to confirm if the observed transition also corresponds to the onset of spectral linewidth narrowing [14, 77].

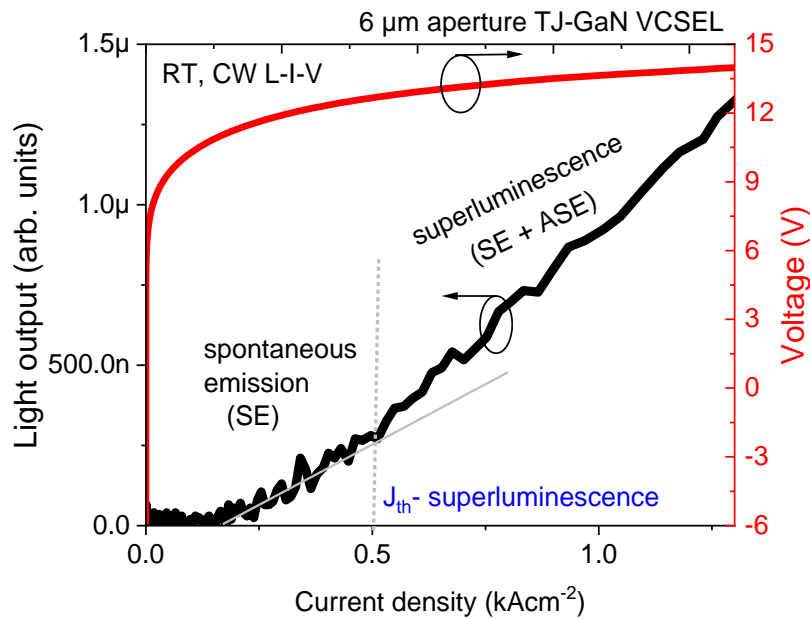


Fig. 5.27 L-I-V characteristics for a 6 μm diameter TJ-VCSEL1 showing an estimation for the threshold current densities for spontaneous (SE) and amplified spontaneous emission (ASE).

As can be seen in Fig. 5.28, both types of VCSEL-structures exhibited spectral broadening. The emission spectra of a 10 μm aperture ITO-VCSEL (Fig. 5.28a) are compared with that of a 4 μm aperture TJ-VCSEL1 (Fig. 5.28b). The spatially averaged spectra clearly showed a cavity mode for both VCSEL devices. At current density of 200 Acm^{-2} , devices showed a broader emission of 5 nm FWHM. For comparison, the spectral FWHM of half-cavity ITO-VCSEL devices was around 7 nm. For TJ-VCSEL1 devices, many peaks emerged after the first emission (at 100 Acm^{-2}) (Fig. 5.28d, inset). It maybe that many peaks of these devices are related to the fluctuations of the EL measurement conditions or could be the different cavity modes which can be distinguished if lasing in many modes would be achieved. In addition to a too low quality of the dielectric top mirror, it can be argued that the V-pits present on the surface of TJ-VCSEL1 structures cause the reduction of the cavity quality. Q-quality factor of the cavity in these VCSEL devices was calculated to be around 84.

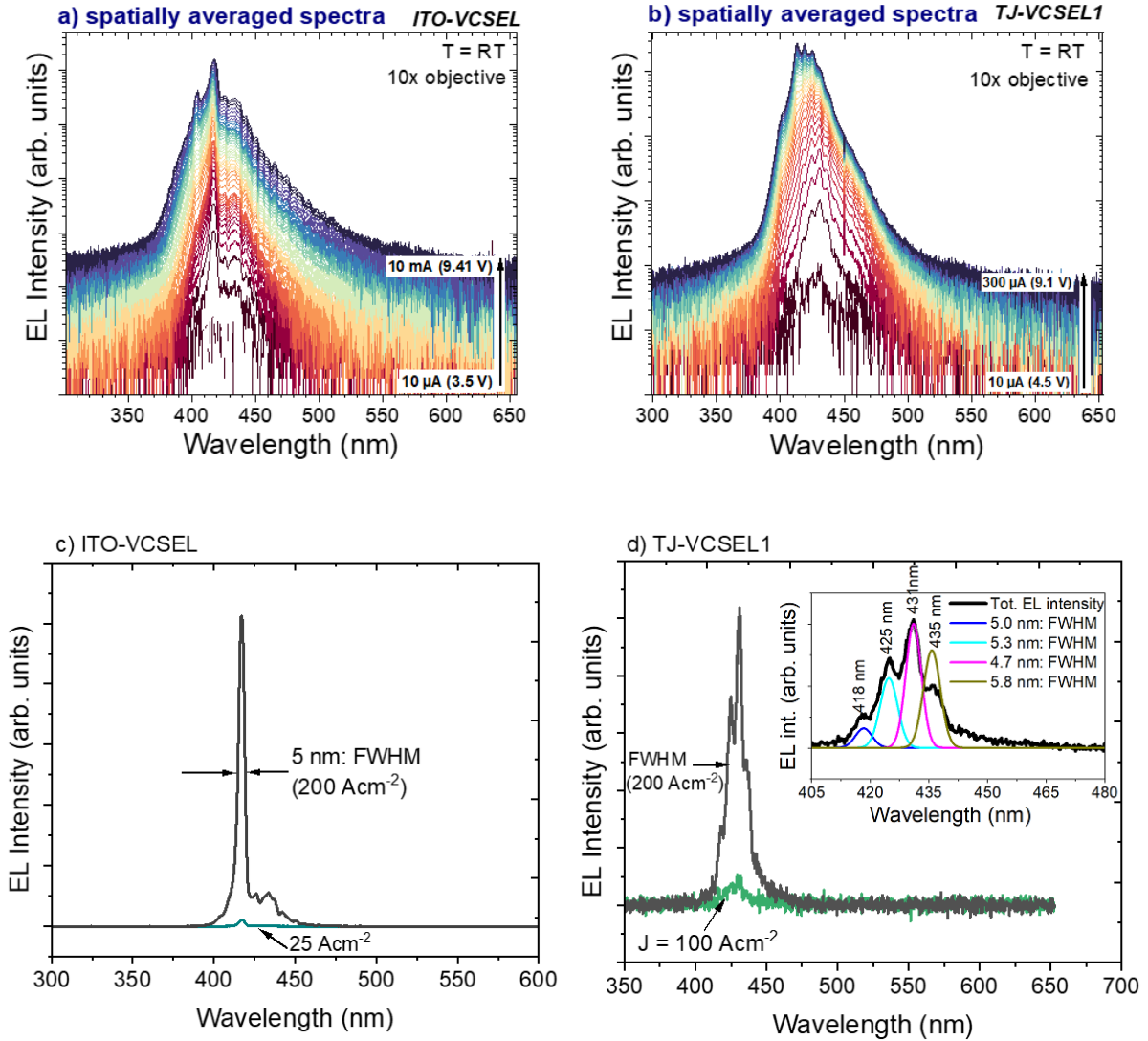


Fig. 5.28 Current injection dependent emission spectra of a) ITO-VCSEL device b) TJ-VCSEL1 device. In c) and d) individual spectra taken at 200 Acm^{-2} are compared.

Fig. 5.29 shows that these threshold current densities for superluminescence were slightly dependent on the aperture diameter. Each data point in the figure represents an average of four values measured in different VCSEL devices. For $6 \mu\text{m}$ and $4 \mu\text{m}$ aperture diameters, the VCSELs have threshold current densities values of 0.5 kAcm^{-2} and 4 kAcm^{-2} , respectively.

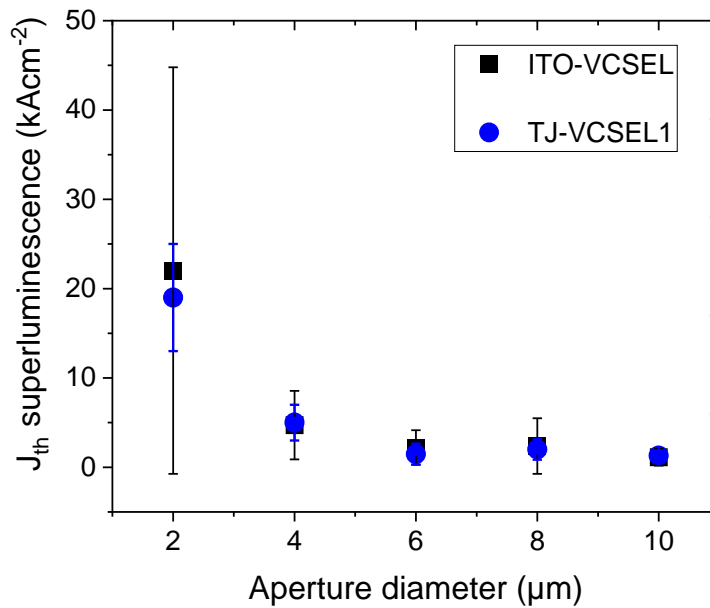


Fig. 5.29 Superluminescence threshold current density for ITO- and TJ-VCSEL devices in dependance on the aperture size.

5.4 Summary

In this chapter, different doping schemes for the p-side region with regard to current-voltage characteristics and processing strategies were investigated for ITO-LEDs and TJ-LEDs to find the best approach for VCSEL fabrication. However, the best scheme for LEDs is not generally ideal for TJ-VCSELs due to surface roughening. TJ-VCSEL devices with better light output than conventional ITO-devices at current densities up to 22 kAcm^{-2} could be realized which is a consequence of the lower absorption of the GaN:Ge layers. Although lasing could not be observed due to quality issues of the top dielectric mirror, the onset of superluminescence at a threshold current density of 0.5 kAcm^{-2} (7.2 V) was observed. Issues to be solved remain for the top DBR deposition, surface morphology and the passivation of the p-side region.

Chapter 6 Highly reflective and conductive AlInN/GaN DBR

6.1 N-type doping of AlInN/GaN multilayer stacks

In the previous chapter, VCSEL structures with low turn-on voltage were demonstrated, although stimulated emission could not be observed most likely due to a too low quality of the upper dielectric mirror. In these structures, the lower reflector was realized by an undoped AlInN/GaN DBR that is highly resistive. Therefore, intra-cavity electrical contacts had to be applied which required a rather large thickness of the cavity to ensure effective current spreading. The longer optical cavity of VCSEL devices the smaller gets the longitudinal optical confinement factor which increases the threshold current density [30]. Therefore, GaN-based VCSELs with an extra-cavity contact on the backside of a n-doped AlInN/GaN DBR would allow for a reduction of the cavity thickness. However, the electrical resistance of AlInN/GaN-based DBRs increased by large polarization fields and a significant conduction band offset of about 1.0 eV between GaN and AlInN [11, 14].

Few studies about the vertical electrical conductivity in n-type AlInN/GaN layers have shown that Si and Ge dopants are suitable donor species to address the band offsets and to screen the polarization fields at the transition from AlInN to GaN [12, 17, 80]. Thereby, e.g., to achieve ohmic characteristics and a high reflectivity in n-doped AlInN/GaN DBRs, Si-modulation doping at the interfaces of AlInN and GaN layer stacks was applied in one report [13]. Additionally, composition grading at the interfaces in combination with modulation doping by Si was suggested [12, 81]. However, such n-type AlInN/GaN DBRs require a complex growth process and the achieved resistance is still relatively high. In previous work, our research group reported on Ge-modulation doping to realize GaN/GaN:Ge DBRs [82]. This approach takes advantage of the refractive index change occurring at very high carrier concentrations due to the Burstein-Moss-effect and it was developed to avoid issues related with lattice mismatch and the very different growth conditions of AlInN and GaN. Although an efficient vertical current transport was achieved for GaN/GaN:Ge DBRs, the small refractive index contrast between GaN and GaN:Ge leads to a narrow stopband width and very long effective cavity length. Therefore, GaN/GaN:Ge DBRs are not suited for the realization of GaN-based VCSELs. In this chapter, highly reflective and conductive AlInN/GaN DBRs are demonstrated by adjusting Ge-doping in the AlInN and GaN layer stacks. First, the impact of Ge- and Si-doping on a simple GaN/AlInN/GaN stack was studied to determine a suitable doping range for detailed

investigation. Then periodic AlInN/GaN heterostructures were experimentally investigated to achieve high vertical conductivity in 10 pairs of n-type AlInN/GaN layer [17]. Finally, optimized Ge-doping values were applied to achieve both highly conductive and reflective AlInN/GaN DBRs suitable for GaN-based VCSEL applications [18].

To study the effects of Ge- and Si-doping on the vertical conductivity of lattice-matched AlInN/GaN DBRs, a simulation of the conduction and valence band profiles according to different doping levels in GaN and AlInN based on a self-consistent solution of the Schrödinger-Poisson-equation using the commercial software Nextnano was performed. From this simulation, doping concentrations well above 10^{19} cm^{-3} are determined in both AlInN and GaN layers to reduce the polarization charge induced enhancement in barriers heights at the AlInN/GaN interfaces [17]. Empirically, a carrier density above 10^{19} cm^{-3} can be achieved for GaN:Ge [46, 82], while a doping concentration around $2 \times 10^{19} \text{ cm}^{-3}$ marks the upper limit for Si-doping in MOVPE, since at higher doping levels GaN:Si layers usually tend to degrade [47]. Here, the Ge-doping and Si-doping concentrations necessary for conductive AlInN/GaN DBRs were experimentally assessed.

The growth of samples was performed in the MOVPE system described in section 3.1. For Ge-doped DBRs, an 800 nm thick GaN:Ge buffer layer was grown below the AlInN:Ge/GaN:Ge DBR. Isobutylgermane (IBGe) was used as precursor for Ge-doping while silane (100 ppm SiH_4) diluted in hydrogen was used for the growth of short multilayer stacks (short DBRs, s-DBRs). GaN:Ge and GaN:Si layers were grown at a temperature of $1100 \text{ }^\circ\text{C}$ at 200 mbar pressure using H_2 carrier gas while Ge- or Si-doped AlInN was grown at a temperature of $745 \text{ }^\circ\text{C}$ at 70 mbar pressure using N_2 carrier gas. These growth conditions for AlInN ensured lattice-matched growth to GaN with an indium content around 18 %. The generally low stability of AlInN and known Ge-memory effects [30] during MOVPE growth put limits on the n-doping in AlInN stacks. The determination of the resulting carrier concentration in AlInN is also not straightforward since the two-dimensional electron gas that forms at the GaN/AlInN interface complicates reliable Hall-effect measurements. In addition, the growth of thick homogeneous AlInN layers is not possible, since layers with thicknesses above 100 nm tend to degrade by changing to a columnar growth mode [83]. Nevertheless, the IBGe and SiH_4 fluxes in n-doped AlInN layers were optimized during MOVPE growth of a first simple sample series with their I-V characteristics presented Fig. 6.1. Nominal thicknesses of these GaN/AlInN/GaN heterostructures were 800 nm/40 nm/200 nm, respectively. The doping concentration of the GaN layers was chosen at a constant level around $1 \times 10^{19} \text{ cm}^{-3}$, while the doping of AlInN was

varied. The electrical measurements were performed by measuring the vertical current transport through separated mesas with a size of $200 \times 100 \mu\text{m}^2$ and a lateral spacing of $20 \mu\text{m}$ (Fig. 6.1, insets). In Fig. 6.1a, the impact of Si-doping of AlInN was investigated. Initially, increasing the SiH_4 flow from 1 to 25 sccm the current transport monotonously improved across the heterostructure, while a further increase of SiH_4 flow to 42 sccm increased the resistivity again.

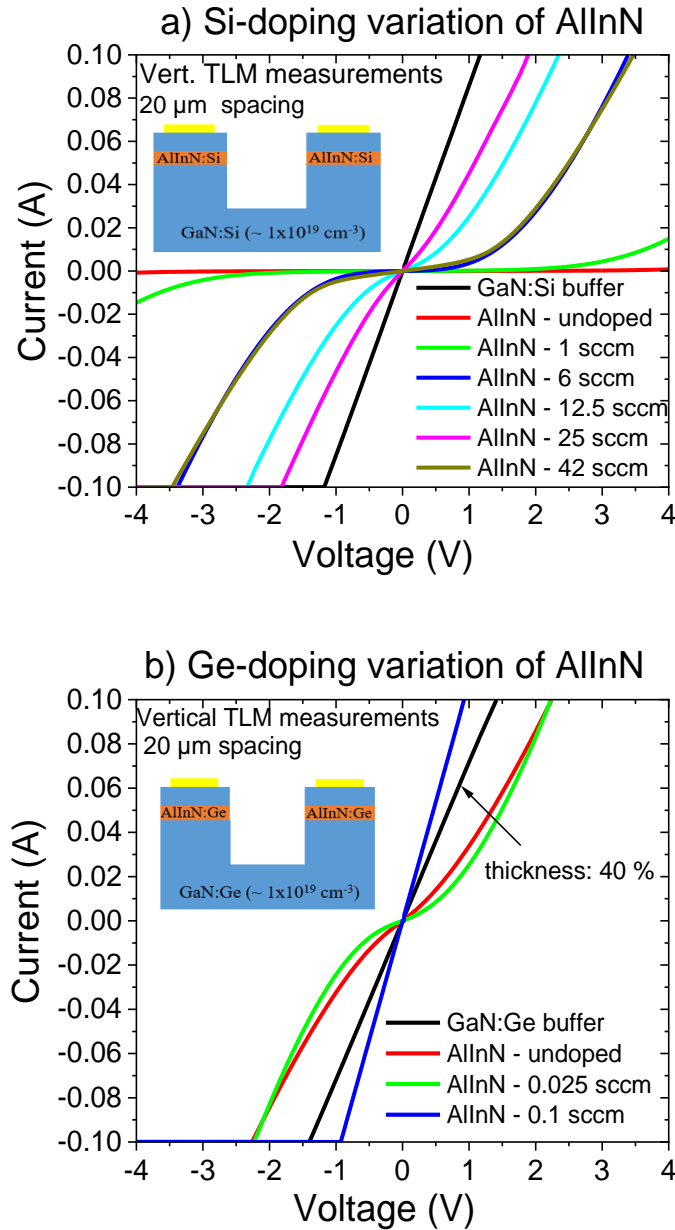


Fig. 6.1 I-V characteristics for (a) Si-doped and (b) Ge-doped GaN/AlInN/GaN heterostructures. Insets show the sample layout for vertical electrical TLM measurements with a lateral spacing of $20 \mu\text{m}$ between terminals.

Although the conductivity can be controlled by a variation of the AlInN:Si doping, even the structure with the lowest resistance still showed a slight S-shape in the I-V curve, i.e. non-ohmic behavior. Additional experiments were carried out using DTBSi as precursor for Si-doping of AlInN. The same trend was observed in the IV-characteristics with slightly higher resistivities. Subsequently, it was studied if better results can be achieved by the application of Ge-doping (Fig. 6.1b). Interestingly, a structure with nominally undoped AlInN sandwiched by GaN:Ge layers already showed a significant conductivity, which could be related to a Ge-memory effect occurring after growth of the GaN:Ge buffer. The origin of the Ge memory effect is not fully resolved but most likely promoted by the much lower growth rate of AlInN. While no significant change in the I-V curve for a small IBGe dopant flow of 0.025 sccm during AlInN growth was observed, ohmic current-voltage characteristics were realized when the doping flow was increased to 0.1 sccm. Therefore, Ge-doping appears to be better suited for the realization of low-resistive AlInN/GaN interfaces.

In the next step, the potential of Si- or Ge-doping for the fabrication of conductive AlInN/GaN superlattices was investigated by growing AlInN/GaN multilayers with 10 or 45 periods. Based on the results on single AlInN/GaN heterostructures, sample structures as shown in Table 6.1 were grown with different dopant flows. In a first sample series, n-type doping of 10-fold GaN/AlInN/GaN DBRs (s-DBRs) was studied for the type of dopant (Si or Ge, or a combination thereof). Thereafter, a second sample series aiming at high reflectivity mirror properties studied 45-fold AlInN/GaN DBRs labeled as samples A, B, C, and D. While sample A is an undoped reference AlInN/GaN DBR where the optical properties were unaffected by doping, the GaN:Ge layers of the other samples were grown with a constant IBGe flow of 28 $\mu\text{mol}/\text{min}$ corresponding to a carrier concentration of $1.6 \times 10^{19} \text{ cm}^{-3}$. AlInN layers in samples A and B, were not doped while the IBGe flow during growth of the AlInN layers of samples C and D was 87 nmol/min and 350 nmol/min, respectively. As the reflectivity is the most critical parameter in VCSEL design, the ideal DBR reflectivity spectra were calculated using the AnalysR software from Laytec. With refractive indices of $n_{\text{GaN}} = 2.54$ and $n_{\text{AlInN}} = 2.3$, the nominal layer thicknesses of the AlInN and GaN quarter-wavelength layers were chosen to 43 nm and 40 nm respectively for initial targeting of a stopband center wavelength of around 400 nm and a theoretical stopband reflectivity of 99.9 %.

Table 6.1 Overview of nominal dopant species and GaN carrier concentration or molar flow rate for the AlInN part in 10-fold DBRs (s-DBRs) and 45-fold DBRs.

Sample	[Si] in GaN	[Ge] in GaN	SiH₄ in AlInN	IBGe in AlInN
s-DBR1	1.1x10 ¹⁹ cm ⁻³	-	110 nmol/min	-
s-DBR2	-	1.4x10 ¹⁹ cm ⁻³	110 nmol/min	-
s-DBR3	-	5.8x10 ¹⁹ cm ⁻³	-	-
s-DBR4	-	5.8x10 ¹⁹ cm ⁻³	110 nmol/min	-
s-DBR5	-	5.8x10 ¹⁹ cm ⁻³	-	350 nmol/min
DBR A	-	-	-	-
DBR B	-	1.6x10 ¹⁹ cm ⁻³	-	-
DBR C	-	1.6x10 ¹⁹ cm ⁻³	-	87 nmol/min
DBR D	-	1.6x10 ¹⁹ cm ⁻³	-	350 nmol/min

For multilayers with 10-layer pairs, Fig. 6.2 shows the corresponding I-V characteristics when measuring vertical current transport. As vertical transport is measured from the top, the current flows vertically through 20 layer pairs and laterally through the highly conducting GaN:Ge buffer layer. For a Si-doped multilayer stack (s-DBR1), the GaN:Si layers were doped to the maximum possible carrier concentration before layer degradation occurs (1.1x10¹⁹ cm⁻³) while the AlInN layers were doped with a SiH₄ flow of 110 nmol/min. The I-V-curve of the 10-fold stack showed non-linear behavior. When the GaN:Si layers were replaced by GaN:Ge with a comparable electron concentration ($n = 1.4 \times 10^{19} \text{ cm}^{-3}$), while the AlInN:Si doping remained unchanged, a comparable non-ohmic I-V-curve resulted (s-DBR2). These non-linear I-V curves imply that the maximum achievable Si-doping concentrations for AlInN in s-DBR1 and s-DBR2 structures is not sufficient for efficient current transport [17]. According to the band profile simulation the free electron concentration in AlInN can be assumed below 1.10¹⁹ cm⁻³.

To improve the electrical conductivity, the carrier concentration of the GaN:Ge layers was increased to 5.8x10¹⁹ cm⁻³ which would not be possible with Si-doping in a MOVPE environment. While no intentional doping during growth of the AlInN layers was applied for s-DBR3, the AlInN layers of s-DBR4 were doped with a SiH₄ flow of 110 nmol/min and for s-DBR5 AlInN was doped with a IBGe flow of 350 nmol/min. Remarkably, similar linear I-V characteristics with strongly reduced resistance were observed for all three s-DBRs (Fig. 6.2). The minor impact of doping the AlInN on electrical characteristic can be explained assuming

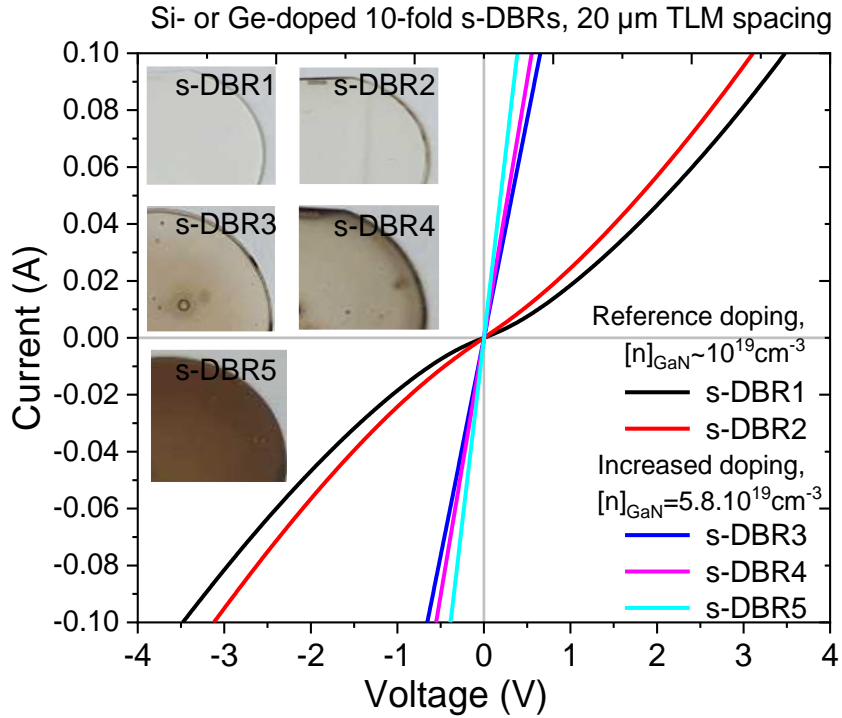


Fig. 6.2 I-V-characteristics of Ge- or Si-doped 10-pair AlInN/GaN DBRs (s-DBRs) when current is injected vertically through the DBR. The samples description can be found in table 1. The inset shows corresponding photographs of quarter wafers. Note that particles induce an additional darkening of the sample.

again a pronounced Ge memory effect. The lowest vertical resistance was observed for s-DBR5 with intentionally doped AlInN:Ge layers using an IBGe flow of 350 nmol/min. However, the wafer showed a brownish appearance, as shown in the inset of Fig. 6.2. This onset of the brownish color change was already observed for s-DBR3 and s-DBR4 which have the same Ge doping concentration in the GaN layers. Since this color change was not observed even for thick GaN:Ge layers with carrier concentration exceeding $1 \times 10^{20} \text{ cm}^{-3}$, one can mainly attribute it to light absorption or scattering in the Ge-doped AlInN layers, eventually caused by point-defects like Ge-atoms at interstitial sites or Ge induced change in In-incorporation. Carlin et al. also observed a brownish appearance of undoped AlInN layers [9]. By increasing the carrier gas flow, the authors were able to remove the brownish color. Interestingly, the Si-doped structures appeared transparent. Additional experiments are required to clarify if the brownish appearance is either related to the growth conditions for AlInN layers itself or to other mechanisms as, e.g., a modified In-incorporation by a Ge-adlayer during growth.

6.2 Structural properties of Ge-doped AlInN/GaN DBRs

Fig. 6.3 shows photographs, AFM and SEM images of the series of DBR structures described in the preceding chapter (Table 6.1). While the undoped structures DBR A and DBR B, with Ge-doping only in the GaN layers, had a transparent appearance, the slight brownish color change was visible for structure C with moderately doped AlInN layers. When the doping of the AlInN layers was further increased for sample D, the color of the DBR even turned black indicating a strong absorption and/or scattering of light within the structure (Fig. 6.3a). Interestingly, the AFM images showed a comparable surface morphology characterized by step-flow growth mode for all samples (Fig. 6.3b), with root-mean-square (rms) roughness values of 0.5, 0.6, 1.0 and 1.5 nm for DBRs A, B, C and D on $10 \times 10 \mu\text{m}^2$ surface areas, respectively.

The fact that the uppermost layer in each structure was GaN, implies that the surface morphology of structure D is not deteriorated thoroughly by the Ge-doping. However, there was a small increase of the rms-value from 0.5 nm for the undoped DBR A to 1.5 nm for the highly doped DBR D likely correlated with an increased AlInN/GaN interface roughness [6]. SEM images of the four DBRs confirmed the periodic sequence of the multilayers (Fig. 6.3c). The DBRs A, B and C have a high structural quality with smooth interfaces. However, the highly doped DBR D was characterized by blurred, undefined interfaces and by an apparent thickness increase of the AlInN layers (dark contrast) as well as a thickness reduction of the GaN layers (grey contrast). In addition, small voids were seemingly generated within the AlInN:Ge layers. The degradation of AlInN already started within the very first AlInN layers but was not increasing within the subsequently grown layers so that a curing effect by GaN growth with regard to surface roughness can be deduced. Nevertheless, it could be concluded that the IBGe-doping flow of 350 nmol/min during AlInN layer growth in DBR D is too high to maintain a high structural quality.

In Fig. 6.4, the in-situ reflectivity signals at a wavelength of 405 nm and the wafer curvature for the undoped DBR A, the moderately doped DBR C and highly doped DBR D were compared. The reflectivity signature looks very similar for DBR A and DBR C (Fig. 6.4a). Therefore, no detrimental influence of the adjusted Ge-doping on the DBR properties was deduced. However, the highly doped DBR D showed a reduced amplitude and modulation height of the reflectivity signal during growth of the upper DBR periods. This implies a

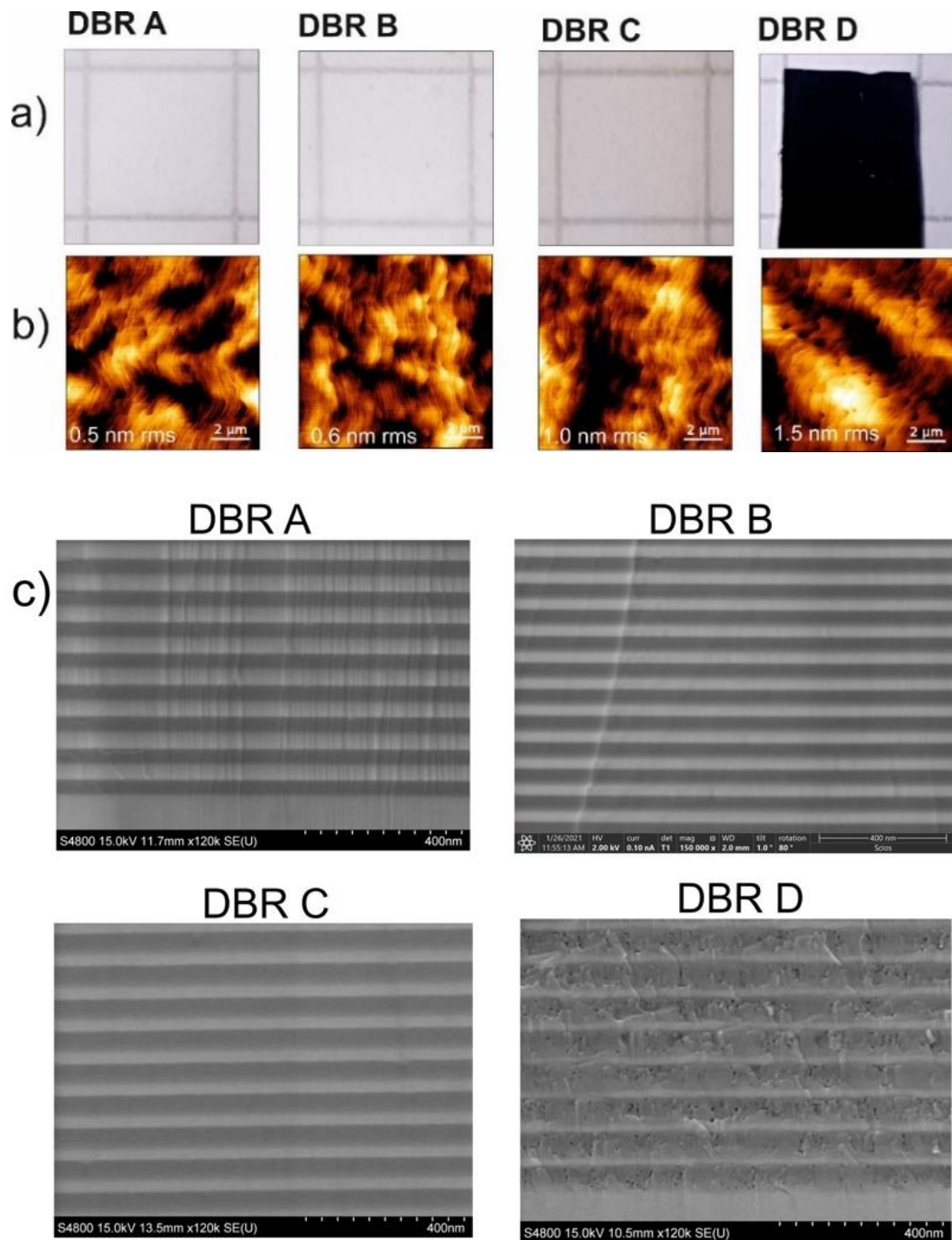


Fig. 6.3 a) Photographs (wafer lying on quad paper with 5 mm line distance), b) AFM images ($10 \times 10 \mu\text{m}^2$) and c) SEM cross-section images of AlInN/GaN DBRs A, B, C and D.

significant loss of light due to light absorption within the AlInN:Ge layers and/or scattering at the deteriorated AlInN:Ge/GaN:Ge layer interfaces. Regarding the in-situ curvature transients (Fig. 6.4b), again DBR A and C were comparable, while DBR D exhibited an increased evolution of compressive stress after growth of the first layer pairs (leading to a more negative

slope during AlInN growth). One would expect that this stress was caused by compositional changes in the AlInN layers associated with an increased indium

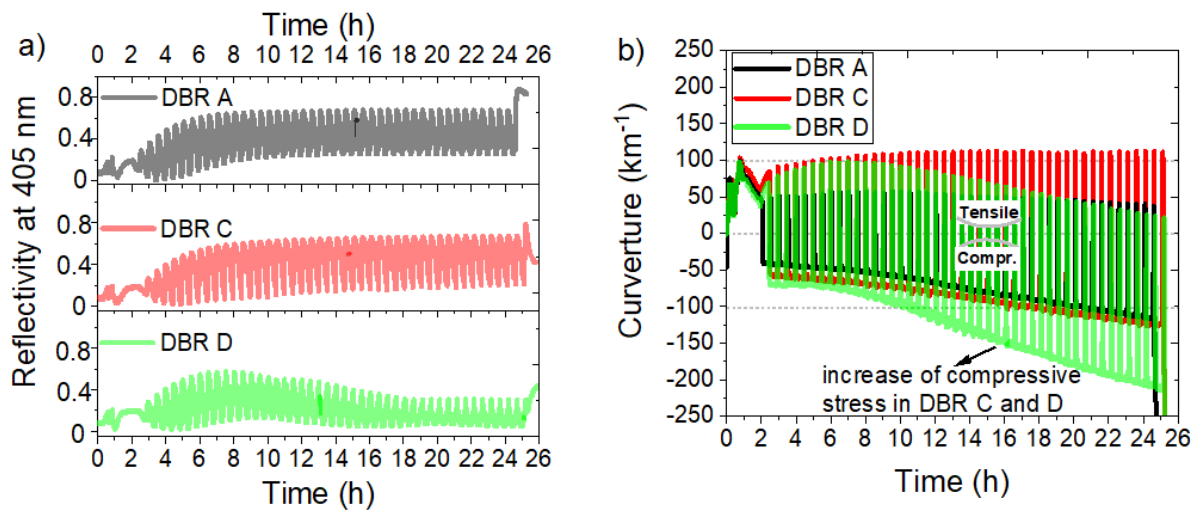


Fig. 6.4 a) In-situ reflectivity at 405 nm and b) in-situ curvature monitored during growth of 45-fold AlInN/GaN DBRs A, C, and D.

incorporation. However, X-ray diffraction data yielded a comparable indium-content for all samples. Therefore, the compressive stress might have been caused by excessive incorporation of Ge into the lattice. The pronounced curvature change when switching from AlInN to GaN conditions for the doped DBRs (as well as the curvature increase at the end of the GaN buffer during growth of the doped DBRs) was caused by higher growth temperature of the GaN:Ge layers. Nevertheless, no generation of tensile stress was observed during growth of the Ge-doped layer opposite to Si-doping of thick GaN layers where edge and mixed type dislocation movement may occur [46]. This is an additional advantage of using Ge as dopant as it helps to prevent crack formation in the DBRs structures.

Fig. 6.5 shows high resolution XRD $\theta/2\theta$ -scans around the GaN (0002) reflection for all samples. Superlattice (SL)-peaks caused by the DBR periodicity were visible for all samples. Their distance is related to the thickness of one AlInN/GaN layer pair. In comparison to DBRs B and C (with undoped or moderately doped AlInN layers), the SL-peaks of the DBR A were present over a wider angular range. Therefore, DBR B and C exhibited a slightly increased interface roughness due to Ge-incorporation, either by unintentional doping due to a Ge-memory effect (DBR B) or by intentional Ge-doping of AlInN (DBR C). Interface roughening was even more evident for the highly Ge doped DBR D. Here, SL-peaks are strongly damped

and vanished quickly for higher orders (larger angles). Both a disturbed DBR periodicity and a reduced homogeneity of layer thicknesses can be made responsible for the change.

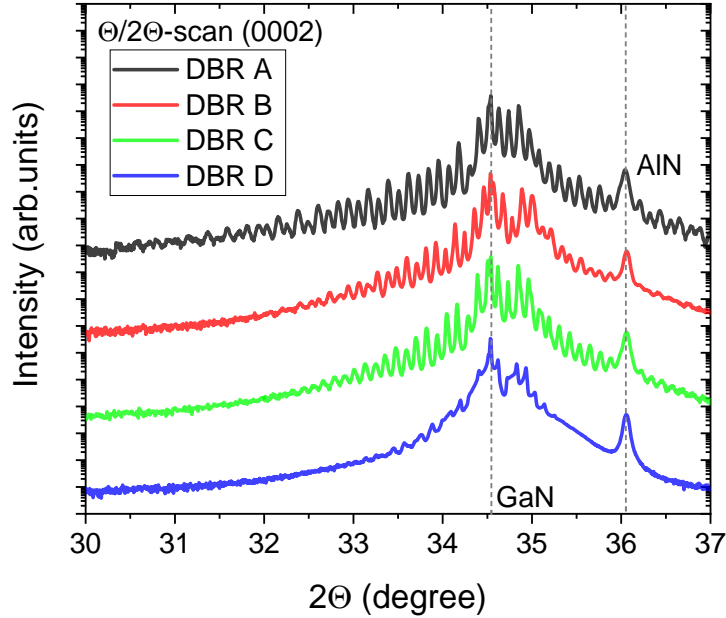


Fig. 6.5 High-resolution X-ray diffraction (0002) $\theta/2\theta$ -scans for DBRs A, B, C and D.

6.3 Electrical and optical properties of Ge-doped AlInN/GaN DBRs

The resistivity of the DBRs was determined by TLM on mesa structures defined by standard photolithography and ICP-RIE. Fig. 6.6 illustrates the measurement geometry and the resulting current path for this type of measurement. After etching through the whole DBR structure down to the GaN:Ge buffer layer, standard n-contact pads (Ti/Al/Ni/Au) were deposited on top of the mesas. By probing two consecutive contact pads, the current passed two times vertically through the whole 45x AlInN/GaN DBR and crosses the GaN:Ge layer in lateral direction as shown in Fig. 6.6a. Therefore, the total resistance (R_{Total}) measured by using four contact probes was composed of the sheet resistance (R_s) of the GaN:Ge layer between the two mesas, two times the contact resistance (R_c) of the metal/semiconductor interface, and two times the vertical series resistance of the DBR (R_{vert}). The current thereby crossed in total 180 AlInN/GaN and GaN/AlInN interfaces. Thus, the total resistance in dependence of the distance d between two consecutive mesas can be expressed as follows:

$$R_{\text{Total}} = \left(\frac{R_s}{w}\right) d + 2R_c + 2R_{\text{vert}} \quad (6.1)$$

where w is the width of the mesa structure. The effective area of the TLM contact pad is the product of width (w) and transfer length (ℓ) of the mesa by $200 \times 100 \mu\text{m}^2$, respectively. Fig. 6.6b shows the current density in dependence of the applied voltage for the DBRs when contacting two adjacent mesas with a distance of $20 \mu\text{m}$. The undoped DBR was highly resistive, whereas the Ge-doped DBRs showed ohmic behavior. Here, DBR D exhibited the lowest resistance while the undoped reference DBR A had virtually no conduction within a bias range of 10 V. While DBR C also had ohmic I-V characteristics with slightly increased resistance (compared to DBR D), DBR B exhibited a reduced conductivity with a resistance that was approximately two orders of magnitude higher. In comparison to the highly conductive 10-pair GaN:Ge/AlInN short DBR with a GaN:Ge doping of $5.8 \times 10^{19} \text{ cm}^{-3}$ (see Fig. 6.2, s-DBR3), the GaN:Ge doping of the 45-pair DBR B was only $1.6 \times 10^{19} \text{ cm}^{-3}$. Apparently, the reduced GaN:Ge doping led to a higher resistivity but also to a higher transparency of the DBR structure B as marked by image of this DBR B in Fig. 6.3a and by the high reflectivity stopband in Fig. 6.7. Therefore, the Ge-memory effect did not provide sufficiently high electron concentration in the AlInN layers and intentional Ge-doping was necessary.

A typical evaluation by TLM of the total resistances is given for DBR C (Fig. 6.6c). After determination of the contact resistance R_C between the n-contacts and the uppermost GaN:Ge layer by measuring surface TLM structures without isolated mesas, the specific vertical resistances of the DBR stacks of DBRs C and D were calculated to $5 \times 10^{-4} \Omega\text{cm}^2$ and $1 \times 10^{-5} \Omega\text{cm}^2$ respectively according eq. 6.1. Although the resistance of DBR D was the lowest, this structure is not suited for devices due to its high optical losses (Fig. 6.7). Nevertheless, the specific resistance of the moderately doped DBR C was still lower than of a previously reported n-type AlInN/GaN DBR by Ikeyama et al. [13], and good optical characteristics suitable for GaN-VCSEL fabrication were achieved.

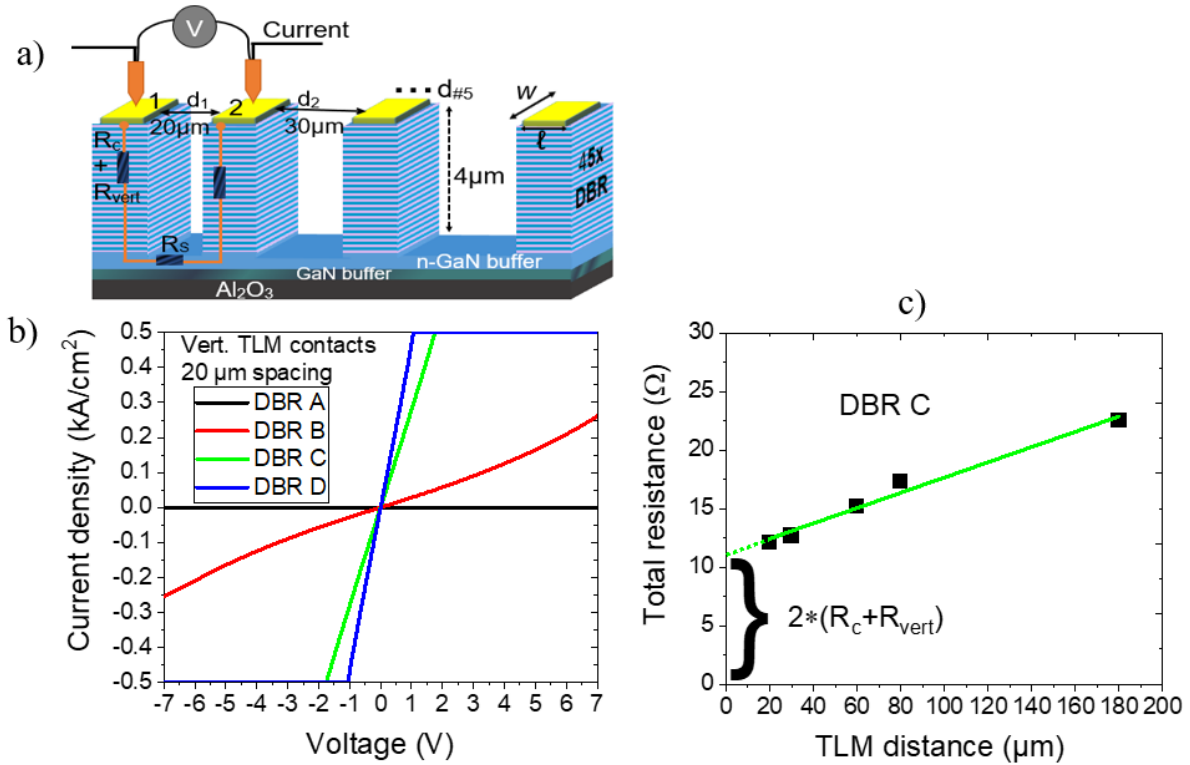


Fig. 6.6 a) Illustration of the fabricated TLM structures for vertical current measurements b) J-V characteristics for DBRs A, B, C and D. c) Total resistance versus distance between adjacent TLM contacts for DBR C.

Fig. 6.7 depicts the reflectance spectra of the DBR structures. The undoped sample A exhibited a well-pronounced stopband with a center wavelength of 397 nm and a maximum reflectivity above 99.8 %. The stopband height was slightly reduced to 99 % for DBRs B and C together with a slight reduction of the stopband width in comparison to DBR A. It is likely that the growth process of Ge-doped AlInN/GaN DBRs can be further improved to eliminate the small impact on the optical properties while maintaining a superior current transport through the mirror. As expected, DBR D showed a strong reduction of the maximum stopband reflectivity. Despite its black appearance, the maximum reflectivity of sample D was still at 86%.

In the following, transfer matrix simulations were conducted to get an estimation of the absorption coefficient and the interface roughness within the DBR structures [5, 30, 33, 34]. From previously performed transmission measurements on thick Ge-doped GaN layers with a carrier concentration of $2 \times 10^{19} \text{ cm}^{-3}$, we found an absorption coefficient of approximately 40 cm^{-1} for GaN:Ge. Taking this absorption coefficient into account, the simulation predicts a reduction of the maximum stopband reflectivity by 0.1 %, only. Therefore, we concluded that

the main cause for the reduced reflectivity of the doped DBRs was the deterioration of the AlInN layers.

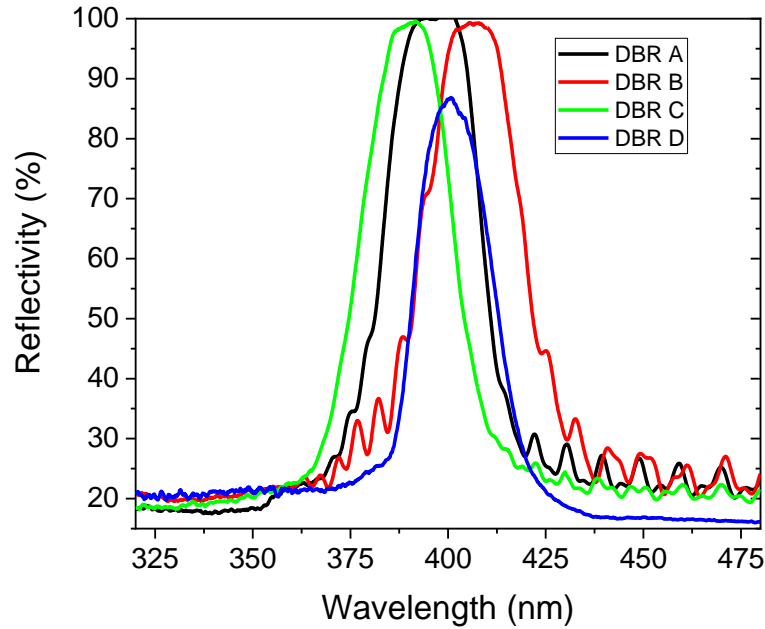


Fig. 6.7 Reflectivity spectra of DBRs A, B, C, and D.

Fig. 6.8 shows the simulated reflectance spectra of all DBRs used in this study. Assuming no additional absorption within the AlInN layers, the simulation of the undoped DBR A fits well to the measured reflectivity confirming its high optical and structural quality. For a better agreement between the measured and simulated stopbands, a spectral broadening parameter of 4 nm was implemented, corresponding to a layer thickness gradient of 1 % across the measuring spot, which is a reasonable value for layers grown in our system. This parameter had to be considered due to the large measurement spot ($\sim 2 \times 8 \text{ mm}^2$). However, the measured intensities of the side band oscillations were slightly lower than the simulated intensities for DBR C while they are much lower for DBR D. This confirms the slight degradation of the interfaces in DBR C and strongly degraded interfaces in DBR D as confirmed by HRXRD measurements (Fig. 6.5). For a satisfactory simulation of DBR B with nominally undoped AlInN and DBR C with moderately doped AlInN layers, the loss coefficient of AlInN had to be increased to 10 cm^{-1} and 40 cm^{-1} , respectively. In addition, an increased

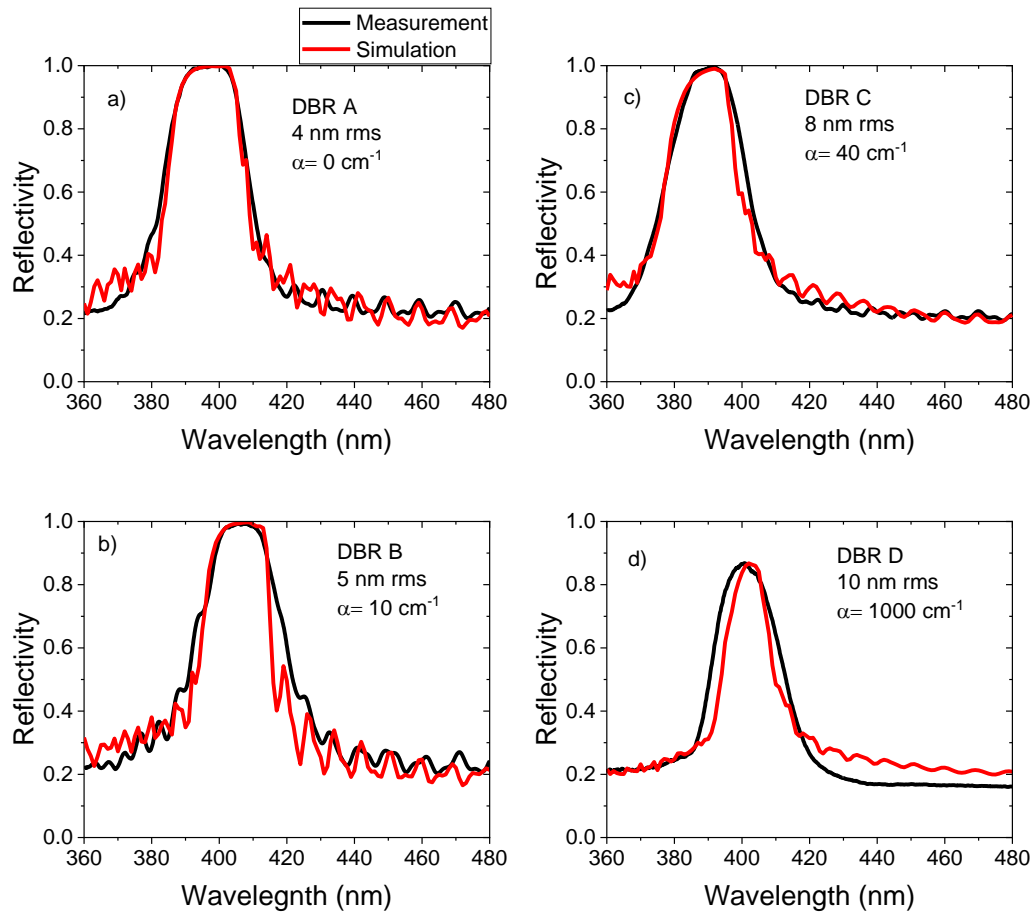


Fig. 6.8 Transfer matrix simulations of experimental reflectivity spectra for DBRs A, B, C and D.

interface roughness of the AlInN/GaN interfaces must be considered. This was done in the simulations by an increase of the spectral broadening by 1 nm (DBR B) and 4 nm (DBR C) in addition to 4 nm spectral broadening of the undoped DBR A. The reduced height and width of the stopband, as well as the black appearance of DBR D was considered by higher loss coefficient of approximately 100 cm^{-1} for the AlInN:Ge layers. The significant roughening of the AlInN/GaN interfaces was taken into account by a spectral broadening of additional 6 nm in comparison to DBR A.

6.4 Analysis of conductance mechanisms

The temperature dependence of the DBRs were compared to study the impact of doping on the resistivity. In this study, temperature-dependent I-V curves were recorded in a liquid nitrogen cooled cryostat over a temperature range of 77- 400 K in 20 K steps. Electrical connections

were realized by wire bonding in four-point-probe geometry onto 2 adjacent mesas with a size of 1 mm², excluding the influence of wire resistance in all measurements.

Fig. 6.9 shows the resistivity as a function of temperature for DBRs A, B, C and D. The highly conductive DBRs C and D showed an increase of the resistance with temperature. This can be explained by a very weak temperature dependence of the carrier concentration n and reduction of the mobility μ with increasing temperature according to the following resistivity relation:

$$\rho = \frac{1}{e \cdot n \cdot \mu}. \quad (6.2)$$

Furthermore, capacitance-voltage (C-V) measurements showed no bias dependence of capacitance for all samples which excludes the existence of any potential barriers or space charge regions.

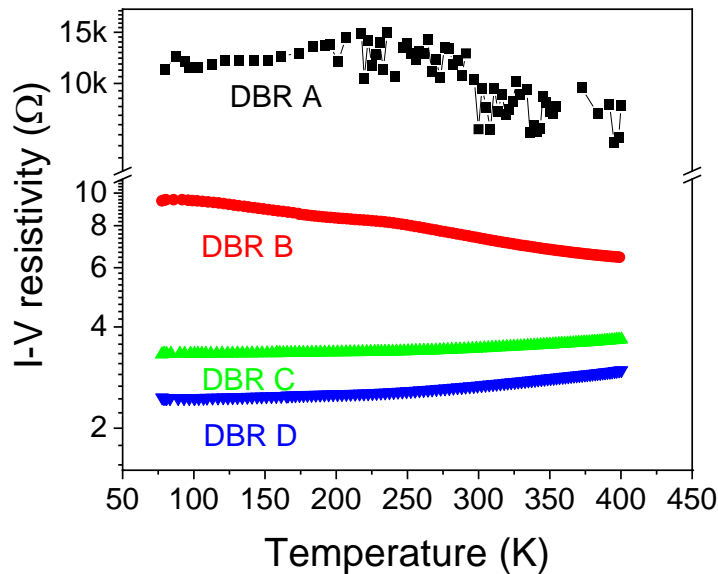


Fig. 6.9 Temperature-dependent I-V resistivity for DBRs A, B, C, and D.

Therefore, this behavior was likely caused by degenerately doped GaN/AlInN/GaN layer and low interface barriers. For the undoped reference DBR (DBR A), the resistance was about 3 orders of magnitude higher than for DBRs C and D and slowly increased in a temperature range between 77 K and approximately 230 K, while it decreased when the temperature is further increased to values up to 400 K. This is typical for undoped semiconductors. For DBR B, with undoped AlInN layers, the resistivity was about 3 times higher as for DBRs C and D and decreased within the whole temperature range. This can be explained by a better electron

transport across the barriers of the heterointerfaces and also by an increasing carrier concentration in the nominally undoped AlInN layer.

A typical I-V characteristic as a function of temperature of DBR C is shown in Fig. 6.10. Only a weak temperature dependence with a less than 6 % decrease in resistance towards lower temperatures was found. This is very similar to metallic behavior and indicates the presence of degenerated semiconductor layers.

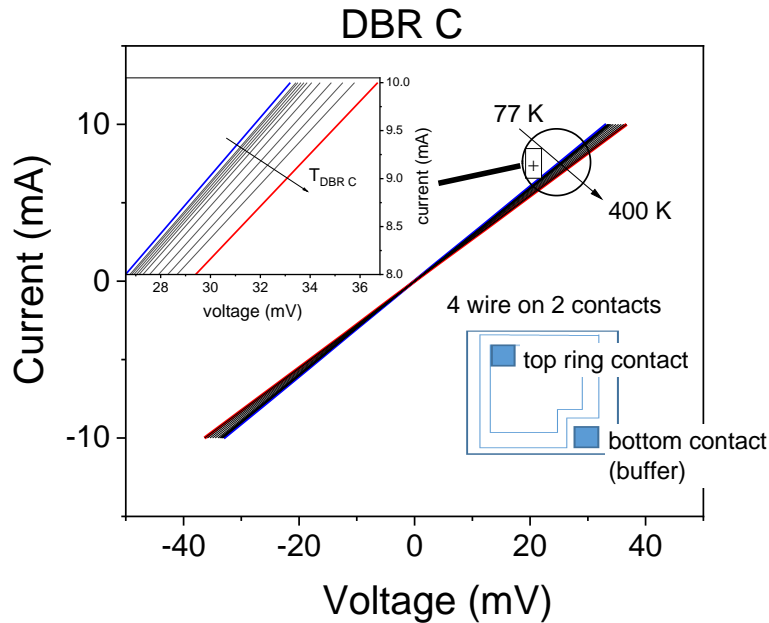


Fig. 6.10 Temperature dependence of the vertical I-V characteristics of low doped DBR C. The inset shows the sample scheme with a 1mm^2 mesa of the DBR C in four-point-probe geometry.

6.5 Summary

In this chapter, highly conductive and reflective Ge-doped AlInN/GaN DBRs were demonstrated. Simulations of the Bragg mirror's reflectivities together with structural analysis by X-ray diffraction reveal an increased optical loss mechanism within the doped AlInN layers and interface roughening as major causes for the observed reduction of the optical reflectivity. By adjustment of the Ge doping level of the AlInN layers, this structural degradation was minimized and a highly conductive 45-fold DBR with a maximum reflectivity of 99 % and ohmic current-voltage characteristics with a vertical specific resistance of $5 \times 10^{-4} \Omega\text{cm}^2$ was realized. Therefore, Ge has the potential to be used as n-type donor to realize highly reflective and low-resistive AlInN/GaN DBRs that are suited for GaN-based VCSELs using extra-cavity metal contacts.

Chapter 7 Summary and outlook

Goal of this thesis was to study novel concepts for the realization of GaN-based VCSELs in the blue spectral range. For better current spreading across the p-GaN region with reduced light absorption, GaN-based homoepitaxial tunnel-junctions were studied as alternative to highly absorbing ITO layers. In order to facilitate current injection through an extra-cavity n-contact which can enable shorter cavities, highly conductive and highly reflective AlInN/GaN Bragg mirrors were realized.

For GaN tunnel junction implementation, their growth and processing were first studied and optimized using LED type devices. By an optimization of the growth parameters in the p-type doping profile, low-resistive tunnel junctions were realized that are characterized by low voltage offset, high transparency and superior current-spreading. Low turn-on voltages of 2.8 V and 3.4 V for standard LEDs and tunnel-junction LEDs, respectively, and similar series resistance of about $1 \times 10^{-4} \Omega \text{cm}^{-2}$ were demonstrated.

Subsequently, three different approaches for the formation of current-apertures in GaN-VCSELs were developed and tested on μm -sized ITO-LEDs and TJ-GaN-based LEDs using tunneling contacts. The realization of devices with aperture sizes between 2 and 10 μm with good I-V characteristics under room temperature continuous wave operation opened the door for the fabrication of GaN-based VCSELs. Improved electro-optical properties of intra-cavity ITO-VCSEL structures and TJ-GaN VCSEL structures under room temperature continuous wave operation were demonstrated. In a direct comparison of TJ-GaN VCSEL-structures and ITO-VCSEL-structures, similar I-V characteristics but higher light output of TJ-GaN VCSEL-structures were obtained. However, both types of VCSEL-structures still exhibited strong spectral broadening due to significant interface roughness in the upper $\text{SiO}_2/\text{HfO}_2$ DBR. The quality factors (Q-factor) were calculated to be around 84 for specific VCSEL devices with either ITO or TJ configuration on the p-region at an operating wavelength of about 420 nm. The resulting increase of light intensity above threshold current in a typical 6 μm aperture VCSEL showed at a threshold current density of 0.5 kAcm^{-2} (7.2 V) the possible onset of superluminescence for TJ-VCSEL devices and 2.5 kAcm^{-2} (6.6 V) for ITO-VCSEL devices.

In this work, highly conductive and reflective 45-fold AlInN/GaN DBRs with of ohmic current-voltage characteristics, a vertical specific resistance of $5 \times 10^{-4} \Omega \text{cm}^2$ and a maximum reflectivity of 99 % were successfully developed by adjusting the Ge doping level in the AlInN layers.

From the direct comparison of Si and Ge doping, Ge is undoubtedly better as n-type donor to realize simultaneously highly reflective and low-resistive AlInN/GaN DBRs.

With major improvements of the upper dielectric mirror fabrication, VCSEL operation of TJ-VCSELs is anticipated. Further progress can be expected from the use of Bulk GaN substrates which improves the reliability of the devices but also reduces the photonic disorder of the optical cavity. Other processing and growth-related issues such as for the fabrication of the current aperture or the properties of the electrons blocking layer must be considered as well. With the now feasible conductive epitaxial DBR structures, one might be able to realize shorter cavity lengths and, therefore, to reduce the threshold current density and increase light output of such VCSELs.

References

1. S. Lee, C. A. Forman, C. Lee, J. Kearns, E. C. Young, J. T. Leonard, D. A. Cohen, J. S. Speck, S. Nakamura, S. P. DenBaars. *Appl. Phys. Express* **11**, 062703 (2018).
2. Y. Higuchi, K. Omae, H. Matsumura, T. Mukai. *Appl. Phys. Express* **1**, 121102 (2008).
3. T. Hamaguchi, M. Tanaka, H. Nakajima. *Jpn. J. Appl. Phys.* **58**, SC0806 (2019).
4. J. T. Leonard, E. C. Young, B. P. Yonkee, D. A. Cohen, T. Margalith, S. P. DenBaars, J. S. Speck, S. Nakamura. *Appl. Phys. Lett.* **107**, 091105 (2015).
5. R. Michalzik, VCSELs: Fundamentals, Technology and Applications of vertical-cavity surface emitting lasers. *Springer Series in Optical Sciences*, Vol. **166** (2013).
6. C. Berger, A. Dadgar, J. Bläsing, A. Lesnik, P. Veit, G. Schmidt, T. Hempel, J. Christen, A. Krost, A. Strittmatter, *J. Cryst. Growth* **414**, 105-109 (2015).
7. T. Aschenbrenner, H. Dartsch, C. Kruse, M. Stoica, M. Gartner, A. Pretorius, A. Rosenauer, T. Wagner, D. Hommel, *J. Appl. Phys.* **108**, 063533 (2010).
8. A. Eljarrat, S. Estrade, Z. Gacevic, S. Fernandez-Garrido, E. Calleja, C. Magen, F. Peiro, *Microsc. Microanal.* **18**, 1143-1154 (2012).
9. J. F. Carlin, C. Zellweger, J. Dorsaz, S. Nicolay, G. Christmann, E. Feltin, R. Butte, N. Grandjean, *Phys. Status Solidi B* **242**, 11, 2326-2344 (2005).
10. AR & VR displays: a target for GaN-based VCSELs - An interview with Sony Corporation - i-Micronews (Oct. 2020).
11. B. Corbett, R. Charash, B. Damilano, H. K. Chauveau, N. Cordero, H. Shams, J. M. Lamy, M. Akhter, P. P. Maaskant, E. Frayssinet, P. de Mierry, J. Y. Duboz, *Phys. Status Solidi C9*, No. 3-4, 931-933 (2012).
12. W. Muranaga, T. Akagi, R. Fuwa, S. Yoshida, J. Ogimoto, Y. Akatsuka, S. Iwayama, T. Takeuchi, S. Kamiyama, M. Iwaya, I. Akasaki, *Jpn. J. Appl. Phys.* **58** (2019).
13. K. Ikeyama, Y. Kozuka, K. Matsui, S. Yoshida, T. Akagi, Y. Akasuka, N. Koide, T. Takeuchi, S. Kamiyama, M. Iwaya, I. Akasaki, *Appl. Phys. Express* **9**, 102101 (2016).
14. T. Takeuchi, S. Kamiyama, M. Iwaya, I. Akasaki, *Rep. Prog. Phys.* **82**, 0125002 (2019).
15. E. Hashemi, F. Hjort, M. Satattin, T. Ive, O. Bäcke, A. Lotsari, M. Halvarsson, D. Adolph, V. Desmaris, D. Meledin, A. Haglund, *Appl. Phys. Express* **10**, 055501 (2017).
16. M. Arita, M. Nishioka, Y. Arakawa, *Phys. Status Solidi A* **194**, (2002).
17. P. Sana, C. Seneza, C. Berger, H. Witte, M. P. Schmidt, J. Bläsing, S. Neugebauer, F. Hoerich, A. Dadgar, A. Strittmatter, *Jpn. J. Appl. Phys.* **60**, 010905 (2021).

18. C. Seneza, C. Berger, P. Sana, H. Witte, J. Bläsing, A. Dempewolf, A. Dadgar, J. Christen, A. Strittmatter, *Jpn. J. Appl. Phys.* **61**, 015501 (2022).
19. S. Neugebauer, M. P. Hoffmann, H. Witte, J. Bläsing, A. Dadgar, A. Strittmatter, T. Niermann, M. Narodovitch, M. Lehmann, *Appl. Phys. Lett.* **110**, 102104 (2017).
20. T. Remmele, M. Albrecht, K. Irscher, R. Fornari, M. Straßburg, *Appl. Phys. Lett.* **99**, 141913 (2011).
21. G. Cosendey, A. Castiglia, G. Rossbach, J.-F. Carlin, N. Grandjean, *Appl. Phys. Lett.* **101**, 151113 (2012).
22. S. M. Sze, K. K. Ng, *Physics of semiconductor devices*, 3rd edn. (Wiley&Sons, Inc. 2007).
23. <https://www.findlight.net/blog/2018/12/28/surface-emitting-lasers/>
24. Philip Moser, *Energy-Efficient VCSELs for Optical Interconnects*. Dissertation, Technische Universität Berlin, 2016.
25. S. Pereira, M. R. Correia, T. Monteiro, E. Pereira, E. Alves, A. D. Sequeira, N. Franco, *Appl. Phys. Lett.* **78**, 9 (2001).
26. Joachim Piprek, *Nitride Semiconductor Devices: Principles and simulation*. WILEY-VCH Verlag GmbH & Co. KGaA, 2007.
27. C. Berger, *Metallorganische Gasphasenepitaxie von nitridischen Mikrokavitäten für vertikal emittierende Laser und Einzelphotonenemitter*. Dissertation, Otto-von-Guericke-Universität Magdeburg, 2017.
28. Mark Fox, Radu Ispasoiu, *Quantum wells, superlattices and band-gap engineering [in Springer handbook of electronic and photonic materials]*, edited by S. Kasap, P. Capper, 2017.
29. M. J. Adams, *Fundamental theory in semiconductor lasers and SOAS*, in *Semiconductor Modeling Techniques Vol. 159*. Edited by X. Marie and N. Balkan, Springer-Verlag Berlin Heidelberg 2012.
30. D. Alexandropoulos, J. Scheuer, M. J. Adams. *Vertical cavities and micro-ring resonators in Semiconductor modeling techniques* **159**, 230-232 (2012).
31. A. D. Rakic, M.L. Majewski, *Cavity and mirror design for vertical-cavity surface-emitting lasers*, Chap. 8 in *Vertical-Cavity Surface-Emitting Laser Devices*, ed. by H. Li, K. Iga, 259–301pp. (Springer, Berlin, 2003).
32. P. Debernardi, R. Orta, *IEEE J. Quantum Electron* **43**, 269–274 (2007).
33. J. Mistrik, S. Kasap, H. E. Ruda, C. Koughia, J. Singh. *Optical properties of electronic materials: Fundamentals and characterization*, in *the Springer Handbook of Electronic*

- and Photonic Materials*, 2nd Ed. 47p (Springer International Publishing AG, Cham 2017).
34. H. A. MacLeod, *Thin film optical filters*. Third edition, Institute of physics publishing, Bristol BS1 6BE, UK (1986 and 2001).
 35. T. E. Sale, Vertical cavity surface emitting lasers. Dissertation, University of Sheffield (1993).
 36. Wie Sun, Chee-Keong Tan, Nelson Tansu, Scientific reports. **7**: 6671 (2017), DOI:10.1038/s41598-017-06889-3.
 37. Y.-Y. Zhang, G.-H. Fan, Y.-A. Yin, G.-R. Yao. Optics Express **20**, (2012).
 38. S. Zhang, E. Xie, T. Yan, W. Yang, J. Herrnsdorf, Z. Gong, I. M. Watson, E. Gu, M. D. Dawson, X. Hu, J. Appl. Phys. **118**, 125709 (2015).
 39. F. Reveret, L. Bignet, W. Zhigang, X. Lafosse, G. Patriarche, P. Disseix, F. Medard, M. Mihailovic, J. Leymarie, J. Zuniga.Perez, S. Bouchoule, J. Appl. Phys. **120**, 093107 (2016).
 40. Y.-K. Song, H. Zhou, M. Diagne, I. Ozden, A. Vertkov, A. V. Nurmikko, Appl. Phys. Lett. **74**, (1999).
 41. H.-C. Wang, M.-C. Chen, Y.-S. Lin, M.-Y. Lu, K.-I. Lin, Y.-C. Cheng, Nanoscale Research Letters **12**: 591 (2017).
 42. L.W. Wu, S. J. Chang, T. C. Wen, Y. K. Su, Senior Member, IEEE, J. F. Chen. Member, IEEE, W. C. Lai, C. H. Kuo, C. H. Chen, J. K. Sheu, IEEE JOURNAL OF QUANTUM ELECTRONICS **38** (2002).
 43. Z. Lin, R. Hao, G. Li, S. Zhang, Jpn. J. Appl. Phys. **54**, 022102 (2015).
 44. S.M. SZE, *Semiconductor devices, Physics and Technology*. AT&T Bell Laboratories, Inc. (1985).
 45. P.R. Hagemana, W.J. Schaff, J. Janinski, Z. Liliental-Weber, J. Cryst. Growth **267**, 123–128 (2004).
 46. A. Dadgar, J. Bläsing, A. Diez, A. Krost, Appl. Phys. Express **4**, 011001 (2011).
 47. S. Fritze, A. Dadgar, H. Witte, M. Buegler, A. Rohrbeck, J. Bläsing, A. Hoffmann, A. Krost, Appl. Phys. Lett. **100**, 122104 (2012).
 48. A. Ajay, J Schörmann, M. Jiménez-Rodríguez, C. B. Lim, F. Walther, M. Rohnke, I. Mouton, L. Amichi, C. Bougerol, M. I. Den Hertog, M. Eickhoff, E. Menroy, J. Phys. D: Appl. Phys. **49**, 44 (2016).

49. W. Götz, N. M. Johnson, J. Walker, D. P. Bour, R. A. Street, *Appl. Phys. Lett.* **68**, 667 (1996).
50. H. Obloh, K.H Bachem, U. Kaufmann, M. Kunzer, M. Maier, A. Ramakrishnan, P. Schlotter, *J. Cryst. Growth* **195**, 270 (1998).
51. U. Kaufmann, P. Schlotter, H. Obloh, K. Köhler, and M. Maier, *Phys. Rev. B* **62**, 10867 (2000).
52. J.-K. Ho, C.-S. Jong, C. C. Chiu, C.-N. Huang, K.-K. Shih, *J. Appl. Phys.* **86**, 4491 (1999)
53. T. Margalith, O. Buchinsky, D. A. Cohen, A. C. Abare, M. Hansen, S. P. DenBaars, L. A. Coldren, *Appl. Phys. Lett.* **74**, 3930 (1999)
54. T. Takeuchi, S. Kamiyama, M. Iwaya, I. Akasaki, *Semicond. Sci. Technol.* **36**, 063001 (2021).
55. K. Kiyohara, M. Odawara, T. Takeuchi, S. Kamiyama, M. Iwaya, I. Akasaki, T. Saito, *Appl. Phys. Express* **13**, 111003 (2020).
56. M. J. Grundmann, U. K. Mishra, *Phys. Stat. Solidi. C* **4**, 2830-2833 (2007).
57. M. F. Schubert, *Appl. Phys. Lett.* **96**, 031102 (2010).
58. M. Malinvern, D. Martin, N. Grandjean, *Appl. Phys. Lett.* **107**, 051107 (2015).
59. F. Akyol, S. Krishnamoorthy, Y. Zhang, J. Hwang, S. Rajan, *Appl. Phys. Lett.* **108**, 131103 (2016).
60. E. C. Young, B. P. Yonkee, W. Feng, S. H. Oh, S. P. DenBaars, S. Nakamura, J. S. Speck, *Appl. Phys. Express* **1**, 9022102 (2016).
61. E. R. Glaser, W. E. Carlos, G. C. B. Braga, J. A. Freitas, Jr., W. J. Moore, B. V. Shanabrook, R. L. Henry, A. E. Wicknenden, D. D. Koleske, H. Obloh, P. Kozodoy, S. P. DenBas, U. K. Mishra, *Phys. Rev. B* **65**, 1. 085312 (2002).
62. M. Kuramoto, S. Kobayashi, T. Akagi, K. Tazawa, K. Tanaka, T. Saito, T. Takeuchi, *Appl. Phys. Express* **11**, 112101 (2018).
63. S.-U.-Masabih, J. Leonard, D. Cohen, S. Nakamura, D. Feezell, *Phys. Status Solidi A* **214**, (2017).
64. A. Demir, G. Zhao, S. Freisem, X. Liua, D. G. Deppe, *Proc. of SPIE Vol.* **7952** (2011).
65. J. He, M. Feng, Y. Zhong, J. Wang, R. Zhou, H. Gao, Yu Zhou, Q. Sun, J. Liu, Y. Huang, S. Zhang, H. Wang, M. Ikeda, H. Yang, *Scientific reports* **8**, 7922 (2018).
66. P. Kozodoy, S. Keller, S.P. DenBaars, U.K. Mishra, *J. Cryst. Growth* **195**, 265-269 (1998).

67. U. Kaufmann, M. Kunzer, M. Maier, H. Obloh, A. Ramakrishnan, B. Santic, P. Schlotter, *Appl. Phys. Lett.* **72**, 1326 (1998).
68. S. Nayak, M. Gupta, U. V. Waghmare, and S. M. Shivaprasad, *Phys. Rev. Appl.* **11**, 014027 (2019).
69. M. A. Reshchikov, G.-C. Yi, and B. W. Wessels, *Phys. Rev. B* **59**, 13176 (1999).
70. Q. Dai, Q. Shan, J. Wang, S. Chhajed, J. Cho, E. F. Schubert, M. H. Crawford, D. D. Koleske, M.-Ho Kim, Y. Park. *Appl. Phys. Lett.* **97**, 133507 (2010).
71. F. Nippert, S. Karpov, I. Pietzonka, B. Galler, A. Wilm, T. Kure, C. Nenstiel, G. Callsen, M. Strassburg, H.-J. Lugauer, A. Hoffmann, *Jpn. J. Appl. Phys.* **55**, 05FJ01 (2016).
72. F. Nippert, S. Y. Karpov, G. Callsen, B. Galler, T. Kure, C. Nenstiel, M. R. Wagner, M. Strassburg, H.-J. Lugauer, A. Hoffmann, *Appl. Phys. Lett.* **109**, 161103 (2016).
73. K. Prabakaran, M. Jayasakthi, S. Surender, S. Pradeep, S. Sanjay, R. Ramesh, M. Balaji, N. Gautier, K. Baskar, *Applied surface Science, Elsevier* **476**, 993-999 (2019).
74. H. Morkoc, *Materials Science and Engineering R* **33**, 135-207 (2001).
75. A. Szyszka, M. Wośko, T. Szymański, R. Paszkiewicz, *Ultramicroscopy* **170**, (2016).
76. T. Hagiwara, K. Saito, H. Chakihara, S. Matsuo, M. Inoue, S. Muranaka, Y. Ota, M. Matsuura. *J. Photopolym. Sci. Technol.* **28**, 1 (2015).
77. C. Shen, T. K. Ng, J. T. Leonard, A. Pourhashemi, S. Nakamura, S. P. DenBaars, J. Speck, A. Y. Alyamani, M. M. El-desouki, B. S. Ooi. *Optics Letters* **41**, (2016).
78. A. A. Alatawi, J. A. Holguin-Lerma, C. H. Kang, C. Shen, R. C. Subeedi, A. M. Albadri, A. Y. Alyamani, T. K. Ng, B. S. Ooi. *Optics Express* **26**, 26356 (2018).
79. A. Kafar, S. Stanczyk, M. Sarzynski, S. Grzanka, J. Goss, G. Tagowski, A. Nawakowska-Siwinska, T. Suski, P. Perlin. *Optics Express* **24**, 9675 (2016).
80. M. Akazawa, B. Gao, T. Hashizume, M. Hiroki, S. Yamahata, and N. Shigekawa, *J. Appl. Physics* **109**, 013703 (2011).
81. S. Yoshida, K. Ikeyama, T. Yasuda, T. Furuta, T. Tekeuchi, M. Iwaya, S. Kamiyama, I. Akasaki, *Jpn. J. Appl. Phys.* **55**, 05FD10 (2016).
82. C. Berger, A. Lesnik, Th. Zettler, G. Schmidt, P. Veit, A. Dadgar, J. Bläsing, J. Christen, A. Strittmatter, *J. Cryst. Growth* **440**, 6 (2016).
83. G. Perillat-Merceroz, G. Cosendey, J.-F. Carlin, R. Butté, and N. Grandjean, *J. of Appl. Phys.* **113**, 063506 (2013).

Appendixes

Appendix A

Lithographic processing parameters

Mg activation in a rapid thermal annealer (RTA)

- Activation of p-GaN for standard pn-junction diodes (std-LEDs and std-VCSELs):
800 °C for 5 minutes in N₂ ambient
- Activation of p-GaN for tunnel junction diodes (TJ-LEDs and TJ-VCSELs):
800 °C for 60 minutes in N₂ ambient
- Oxygen precondition or p-contact annealing
550 °C for 5 minutes in O₂ ambient

Lithography

After cleaning of quarter wafers by rinsing them with ultrasonic in acetone, isopropanol and DI water they were processed as:

Positive photoresist (MA-P1240), T = RT	Negative photoresist (nLoF2020), T = RT
<ul style="list-style-type: none"> ▪ Spin coating: 1000/3/5s 3000/5/40s ▪ Soft bake: 3' @100 °C ▪ UV-exposure: 70'' @22 mWcm⁻² (using MA14 mask aligner system) ▪ Post bake: none ▪ Development: MA-D331, 40s 	<ul style="list-style-type: none"> ▪ Spin coating: 1000/3/5s 3000/5/40s ▪ Soft bake: 1' @110 °C ▪ UV-exposure: 1.5'' @22 mWcm⁻² (MA14 mask aligner system) ▪ Post bake: 1' @110 °C ▪ Development: AZ826, 30s

ICP-RIE (etching)

GaN-etching	Si ₃ N ₄ or SiO ₂ -etching
<ul style="list-style-type: none"> ▪ RF-power 15 W, ICP-power 50 W (etching rate: ~50 nm/min) ▪ Process: GaNs75 st JH 3mT ▪ Cl₂, 42 sccm and Ar, 14 sccm plasma 	<ul style="list-style-type: none"> ▪ RF-power 15 W, ICP-power 50 W (etching rate: ~24 nm/min) ▪ Process: GaNs75 st JH 3mT ▪ SF₆, 70 sccm and O₂ 5 sccm plasma

Metallization (in e-beam)

- Ti/Al/Ni/Au (14 nm/33 nm/10 nm/60 nm) for n-contacts deposition
- Ni/Au (10 nm/10 nm) for p-contacts deposition

Stripping

- Stripper chemicals for negative photoresist: NI555 or SH5 and acetone
- Stripper chemicals for positive photoresist: P1316 or SH5 and acetone

p-GaN surface treatments

- SAG-approach for TJ-overgrow: O₂ plasma asher flow (200 W, 5 min, 3.5 mbar)
BOE 3 min before TJ-overgrown
- O₂ plasma asher cleaning prior to n-contact deposition: (50 W, 30s, 2.5 mbar)

GaN:Ge sidewall-etch facets treatment

- TMAH: 70 °C, from 10 to 15 min for 100 to 350 nm sidewall-etch depth, respectively
- Aqua regia to remove Ni-mask: 20 seconds

Publication list

- P. Sana, **C. Seneza**, C. Berger, H. Witte, M. -P. Schmidt, J. Bläsing, S. Neugebauer, F. Hoerich, A. Dadgar, and A. Strittmatter. *Low-resistivity vertical current transport across AlInN/GaN interfaces*. Jpn. J. Appl. Phys. **60**, 010905 (2021).
- **C. Seneza**, C. Berger, P. Sana, H. Witte, J. Bläsing, A. Dempewolf, A. Dadgar, J. Christen, A. Strittmatter, Jpn. J. Appl. Phys. **61**, 015501 (2022).

Conferences and workshops

- **Seneza Cleophace**, Berger Christoph, Witte Hartmut, Bläsing Jürgen, Dempewolf Anja, Dadgar Armin, Christen Jürgen, Strittmatter André.
Highly reflective and conductive AlInN/GaN distributed Bragg reflectors realized by Ge-doping. In: DPG-Frühjahrstagung: Dresden, 15. - 20. März 2020 - Bad Honnef: DPG, 2020, Vortrag: HL 30.27
- **C. Seneza**, C. Berger, H. Witte, J. Bläsing, A. Dempewolf, A. Dadgar, J. Christen, A. Strittmatter. *Highly reflective and conductive AlInN/GaN distributed Bragg reflectors realized by Ge-doping*. DGKK workshop on epitaxy of III-V compounds, Dresden (2019)
- Berger Christoph, Neugebauer Silvio, **Seneza Cleophace**, Witte Hartmut, Bläsing Jürgen, Dadgar Armin, Strittmatter André. *GaN:Ge as transparent conductive nitride contact layer for blue tunnel-junction LEDs*. In: DPG-Frühjahrstagung: Dresden, 15. - 20. März 2020 - Bad Honnef: DPG, 2020, Vortrag: HL 8.3
- Witte Hartmut, **Seneza Cleophace**, Sana Prabha, Berger Christoph, Dadgar Armin, Strittmatter André. *Thermally activated spreading resistance of Si- and Ge-doped lattice matched GaN/InAlN periodic stacks*. In: DPG-Frühjahrstagung: Dresden, 15. - 20. März 2020 - Bad Honnef: DPG, 2020, 2020, Vortrag: HL 68.5
- C. Berger, S. Neugebauer, **C. Seneza**, H. Witte, F. Hörich, A. Dadgar, A. Strittmatter. *Heavily Ge-doped GaN as transparent current spreading layer for blue tunnel junction light emitting diodes*. DGKK workshop on epitaxy of III-V compounds, Dresden (2019)

- Berger, Christoph; Neugebauer, Silvio; **Seneza, Cleophace**; Bläsing, Jürgen; Dadgar, Armin; Strittmatter, André. *GaN:Mg/GaN:Ge tunnel junctions for better light emitters*. In: ICNS13, 13'th International Conference on Nitride Semiconductors, Bellevue, Washington, USA, 7-12 July 2019, 2019, S. -, Online
- Berger, Christoph; Neugebauer, Silvio; **Seneza, Cleophace**; Bläsing, Jürgen; Dadgar, Armin; Christen, Jürgen; Strittmatter, Andrée-Woo. *Small-area current injection in GaN-based light emitters with tunnel junctions*. In: Verhandlungen der Deutschen Physikalischen Gesellschaft e. V. Berlin 2018 - Bad Honnef: DPG, 2019, Art. HL2.5; [Tagung: DPG-Frühjahrstagung, Regensburg, 31. März - 05. April 2019]

Other publications

- M.L. Chithambo, **C. Seneza**, J.M. Kalita, Radiat. Meas. **105**, 7-16 (2017)
<https://doi.org/10.1016/j.radmeas.2017.08.009>
- M.L. Chithambo, **C. Seneza**, F.O. Ogundare, Radiat. Meas. **66**, 21-30 (2014)
<http://dx.doi.org/10.1016/j.radmeas.2014.04.025>
- M.L. Chithambo, **C. Seneza**, Physica B **439**, 165-168 (2014)
<http://dx.doi.org/10.1016/j.physb.2013.11.045>
- **C. Seneza**, M.L. Chithambo, *Study of F-center defects in carbon-doped aluminium oxide using luminescence techniques*. International Symposium on Luminescence, Port Elizabeth, South Africa, 1 – 6 July (2012).

Appendix C

Declaration of Honor

I hereby declare that, I prepared and submitted this thesis on the subject

“Fabrication of electrically pumped vertical cavity surface emitters employing GaN:Mg/GaN:Ge tunnel junction contacts”

without the impermissible help of third parties and that none other than the aids indicated have been used; all sources of information are clearly marked, including my own publications.

I further declare that this work has not yet been submitted as a doctoral thesis in the same or a similar form in Germany, nor in any other country. It has not yet been published as a whole.

Magdeburg, 30.06.2022

M. Sc. Cleophace Seneza